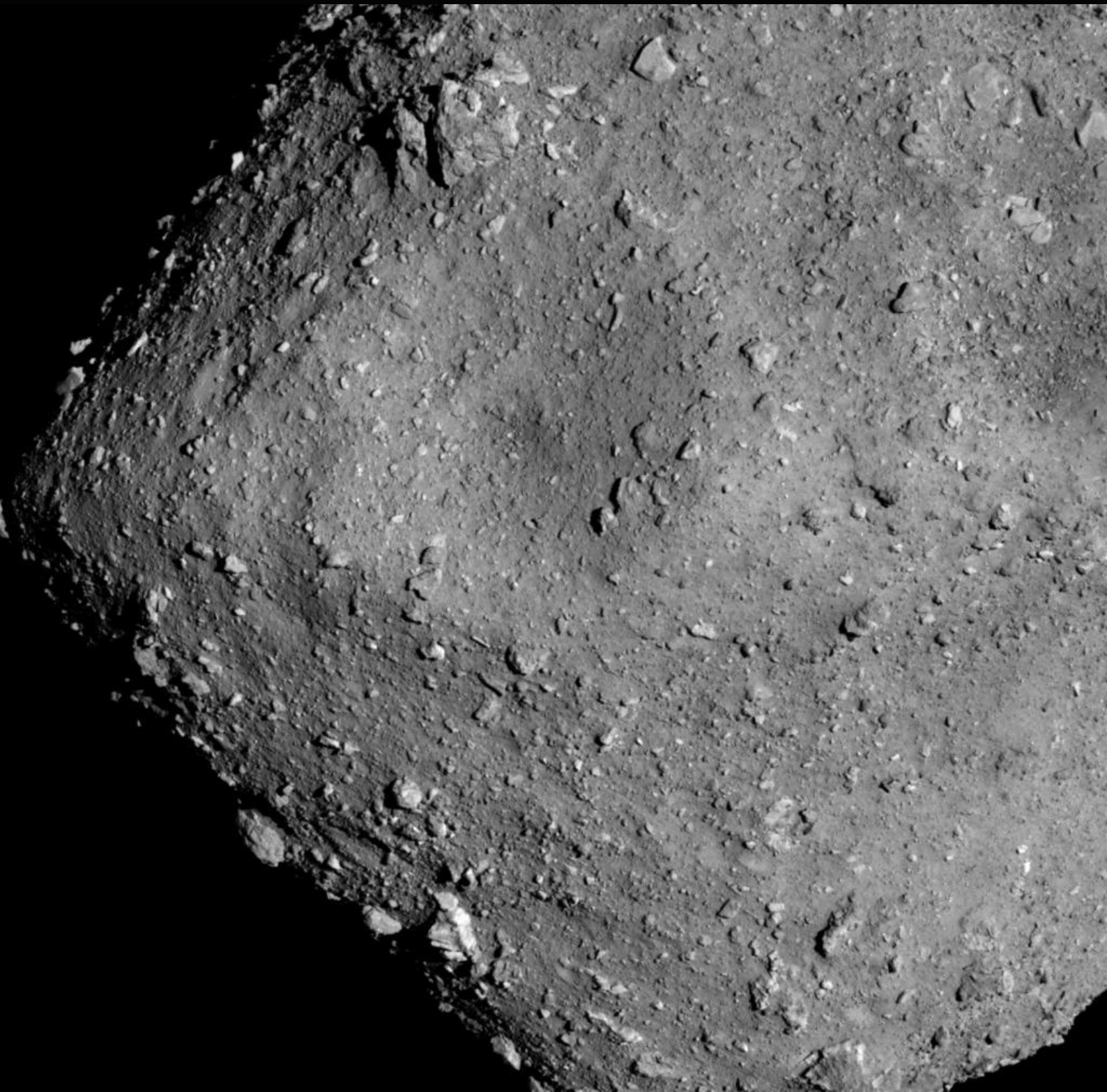


# Temporary Capture of Asteroid Ejecta into Periodic Orbits: Application to JAXA's Hayabusa2 Impact Event

Daniel Villegas Pinto





# Temporary Capture of Asteroid Ejecta into Periodic Orbits: Application to JAXA's Hayabusa2 Impact Event

by

Daniel Villegas Pinto

A thesis submitted to the  
Faculty of Aerospace Engineering of the  
Delft University of Technology  
in partial fulfillment  
of the requirements for the degree of  
Master of Science  
in Aerospace Engineering,  
to be defended publicly on Tuesday April 16, 2019 at 9:00 AM.

Student number:	4634802	
Thesis Committee:	Dr. Jeannette Heiligers	TU Delft, Supervisor
	Dr. Stefania Soldini	JAXA, Supervisor
	Prof. Dr. Pieter Visser	TU Delft, Chair
	Dr. Alessandra Menicucci	TU Delft, External

An electronic version of this thesis is available at <http://repository.tudelft.nl/>.

Frontispiece: Asteroid (1999 JU3) Ryugu as seen from the Hayabusa2 spacecraft. Courtesy of JAXA, University of Tokyo, Kochi University, Rikkyo University, Nagoya University, Chiba Institute of Technology, Meiji University, University of Aizu and AIST.



*"Every book, every volume you see here, has a soul. The soul of the person who wrote it and of those who read it and lived and dreamed with it. Every time a book changes hands, every time someone runs his eyes down its pages, its spirit grows and strengthens."*

– Carlos Ruiz Zafón, *The Shadow of the Wind*

# Acknowledgments

The path my life has followed continues to amaze me to this day. I've been extremely fortunate in these past two and a half years – some might say lucky even – in the experiences I've lived, the people I've met, and the opportunities I've encountered. Although I am one to follow my dreams, I'm sure none of this would've been possible without the people that helped me throughout this time, and on whom I could always rely.

I would firstly like to thank my two supervisors, Dr. Jeannette Heiligers and Dr. Stefania Soldini, for their continuous support, availability, and kindness during this thesis project. You were more than simple monitors of my work; your candor, openness, ability to always ask the “right questions”, and your general help – even from over 9000 km away - never failed to motivate and inspire me. Jeannette, I was truly fortunate to have you as a supervisor. Our many interactions were always a source of ideas and encouragement. Stefania, I must thank you profusely, for my time in Japan would never have been possible – nor nearly as fulfilling – without you. You went above and beyond to help in all you could, and I could not be more thankful. I hope the three of us can continue the work we've developed so far, and I will surely miss our weekly (skype) meetings.

I would also like to extend my deepest appreciation to Prof. Yuichi Tsuda, for kindly receiving me in his lab at JAXA's Institute of Space and Astronautical Science in Kanagawa, Japan. Your insight and recommendations were always much appreciated and extremely valuable. Moreover, the chance to be next to the control room during the first ever successful deployment and landing of a rover to an asteroid was the experience of a lifetime.

My time in Japan would not have been the same without the people I shared it with. I discovered lifelong friends and experienced some of the most unique adventures ever. As someone once wrote, “Happiness is only real when shared”. Thank you to all my friends and colleagues at JAXA, I will always treasure our memories. I already miss our weekly beers, our random trips, and even our daily lunch at ISAS's cafeteria.

This journey would not have been possible without the continuous support and love from my friends and family. To my parents and my brother, you have always been a rock I can lean on, and your words and encouragement have never failed me. To my aunt, thank you for helping me through these two years and half. None of this would've been possible without you and I will always cherish your kindness and compassion. Last but not least, Catarina. Thank you for your support, your help, and your patience. You have never failed to bring me joy and calm my mind. I could not have asked for more.

*Daniel Villegas Pinto*  
*Delft, April 2019*



# Summary

Near-Earth Objects (NEOs) such as asteroids and comets, offer us the possibility of looking back into the early days of the solar system. Given the wealth of their scientific information, their study could allow us to learn about the origins of water on Earth, and possibly even the origin of life. Moreover, the fact that NEOs, by definition, orbit the Sun at close distances, means current space technology can be used to make round-trip missions to these objects not only feasible but in fact potentially more cost-effective than the standard planetary mission. Nonetheless, with new goals come new challenges, and the chaotic dynamical environment inherent to these small bodies is certainly one of them. Given their generally small gravity, the solar radiation pressure is a major perturbation to the system, which alters the dynamics significantly. This is specially true when considering objects with large area-to-mass ratios, as is the case for asteroid ejecta, the topic of this thesis.

This report presents the work developed on the topic of temporary capture of asteroid ejecta into periodic orbits about the asteroid, applied to the case of the Hayabusa2 mission from the Japan Aerospace Exploration Agency (JAXA). Hayabusa2 is a sample-return mission to the C-type asteroid Ryugu, which arrived at the asteroid at the end of June 2018. After an observation period and two touchdown sample collection maneuvers, the spacecraft will fire its Small Carry-on Impactor (SCI) at the asteroid, creating a crater that will allow the observation and collection of subsurface material. However, the ejecta from this cratering event may pose dangers to the mission if it remains about the asteroid for long periods of time.

In this thesis we approach the problem of temporary orbital capture of ejecta particles in periodic orbits using invariant manifold theory. As opposed to using extensive brute-force simulations of wide ranges of initial conditions, this approach allows us to efficiently find physical constraints (e.g., ejection velocities, impact location, and particle radius) for ejecta particles to remain temporarily trapped in periodic orbits and assess the dangers posed by the SCI operation to the Hayabusa2 spacecraft. The results found with this methodology could also be used to constrain numerical brute-force simulations in high-fidelity models to find other initial conditions that lead to similar orbital captures.

We model the dynamical framework of the problem using a perturbed Augmented Hill Problem (AHP), which includes solar radiation pressure, the effect of eclipses, and the  $J_2$  and  $J_4$  terms of the asteroid's gravity potential spherical harmonics expansion.

This study has allowed us to identify the impact locations that lead to the largest number of ejecta particles being captured into three families of periodic orbits, namely, the AHP equivalents of the planar  $a$  and  $g'$  families and the southern halo orbits, where the latter are commonly known as terminator orbits. Most importantly, we were able to find impact locations for which no ejecta particles get captured into these periodic orbits, identifying the Sun-side of the asteroid at medium latitudes as the best impact location.

Furthermore, important conclusions to the effects of including solar radiation pressure and the effect of eclipses in the dynamics of the system are also established, particularly regarding the structure of the stable manifolds of the equilibrium points and the stability of periodic orbits. We point to the importance of including the solar radiation pressure in the study of the dynamical environment about small bodies. Last but not least, the conclusions and methodology applied in this study are found to have applications beyond the study of ejecta dynamics: a similar approach can be followed to design landing trajectories from periodic orbits to the surface of small bodies.



# Contents

<b>Acknowledgments</b>	<b>iii</b>
<b>Summary</b>	<b>v</b>
<b>Nomenclature</b>	<b>ix</b>
List of Symbols . . . . .	ix
List of Acronyms . . . . .	x
List of Sub/Superscripts . . . . .	x
<b>List of Figures</b>	<b>xi</b>
<b>List of Tables</b>	<b>xiii</b>
<b>I Introduction</b>	<b>1</b>
I.1 Missions to NEOs . . . . .	1
I.1.1 NEAR Shoemaker . . . . .	2
I.1.2 Hayabusa . . . . .	2
I.1.3 Deep Impact . . . . .	2
I.1.4 Hayabusa2 . . . . .	3
I.1.5 OSIRIS-REx . . . . .	4
I.1.6 AIDA . . . . .	5
I.2 Literature Review/State-of-the-art . . . . .	5
I.3 Research Questions . . . . .	6
I.4 Thesis Structure. . . . .	6
<b>II Journal Article</b>	<b>7</b>
<b>III Conclusions and Recommendations</b>	<b>57</b>
III.1 Review of Research Questions. . . . .	57
III.2 Recommendations . . . . .	60
III.2.1 Future Work . . . . .	60
III.2.2 Other Applications. . . . .	61
<b>Bibliography</b>	<b>67</b>
<b>Appendices</b>	<b>71</b>
<b>A Verification and Validation</b>	<b>73</b>
A.1 State vector integration . . . . .	74
A.2 STM integration. . . . .	77
A.3 Differential correction algorithm . . . . .	80



# Nomenclature

## List of Symbols

$\mathbf{a}_{SRP}$	Solar radiation pressure acceleration vector in dimensional coordinates
$A$	Exposed surface area
$C$	Jacobi constant
$C_{lk}$	Stokes coefficients of degree $l$ and order $k$ for spherical harmonics
$C_R$	Albedo or total reflectance
$J$	Jacobian
$J_2, J_4$	Gravitational effects due to $C_{20}$ and $C_{40}$ , respectively
$k$	Stability index
$l$	Degree
$m$	Mass
$n$	Order
$r$	Distance
$\mathbf{r}$	Position vector
$R$	Radius
$\mathbf{R}$	Reference frame
$t$	Time
$T$	Period
$T_a$	Period of asteroid about the Sun
$\mathbf{X}$	State vector
$\beta$	Dimensionless solar radiation pressure acceleration
$\delta$	Declination
$\Delta$	Variation or error
$\Delta C_{max}$	Maximum variation of the Jacobi constant
$\Delta C_{max}^*$	Maximum variation of modified the Jacobi constant
$\epsilon$	Small perturbation
$\zeta$	Right ascension
$\lambda_i$	Eigenvalues of the state transition matrix, $i = 1, 2$
$\mu$	Gravitational parameter of asteroid
$\mu_S$	Gravitational parameter of the Sun
$\Phi$	State transition matrix
$\Phi_M$	Monodromy matrix
$\omega$	Angular velocity of asteroid around Sun

## List of Acronyms

AHP	Augmented Hill Problem
AIDA	Asteroid Impact and Deflection Assessment
AU	Astronomical Unit
CR3BP	Circular Restricted Three-Body Problem
JAXA	Japan Aerospace Exploration Agency
NASA	National Aeronautics and Space Administration
NEAR	Near-Earth Asteroid Rendezvous
NEO	Near-Earth Object
ODE	Ordinary Differential Equation
SCI	Small Carry-on Impactor
SOI	Sphere of Influence
SRP	Solar Radiation Pressure
STM	State Transition Matrix
RPA	Radiation Pressure Approximation
ZVC	Zero-Velocity Curve

## List of Subscripts/Superscripts

$\square_0$	Initial conditions
$\square_a$	From the asteroid's orbit
$\square_{Hill}$	In Hill frame
$\square_{imp}$	Impact condition
$\hat{\square}$	Unit vector
$\dot{\square}$	First-order derivative with respect to time
$\ddot{\square}$	Second-order derivative with respect to time

# List of Figures

I.1 Asteroid Eros as seen from NEAR. Courtesy of NASA. . . . .	2
I.2 Asteroid Itokawa as seen from Hayabusa. . . . .	3
I.3 Hayabusa2's mission timeline and trajectory design. The reference frame is centered on the Sun with the Earth situated in the positive $x$ -axis. . . . .	3
I.4 Asteroid Ryugu as seen from Hayabusa2. Courtesy of JAXA, University of Tokyo, Kochi University, Rikkyo University, Nagoya University, Chiba Institute of Technology, Meiji University, University of Aizu, AIST. . . . .	4
I.5 Asteroid Bennu as seen from OSIRIS-REx. Courtesy of NASA, Goddard, and University of Arizona. . . . .	4
III.1 Times of flight for the landing trajectories following the unstable manifolds of the $a$ and terminator families. . . . .	62
III.2 Example of a landing trajectory for a terminator orbit that is very close to the $L_2$ point. . . . .	62
III.3 Example of a landing trajectory from a terminator orbit that orbits the asteroid several times before landing. . . . .	63
III.4 Impact velocities and angles for the $a$ and terminator families. . . . .	63
III.5 Impact locations for terminator family with $\beta = 1000$ as a function of the impact angle. . . . .	64
III.6 Landing trajectory from family $a$ orbit, with the following conditions: $t_{flight} = 5.00$ days, $\sigma_{imp} = 91.617^\circ$ , $v_{imp} = 0.3353$ m/s. . . . .	64
III.7 Landing trajectory from terminator orbit, with the following conditions: $t_{flight} = 4.75$ days, $\sigma_{imp} = 90.63^\circ$ , $v_{imp} = 0.3358$ m/s. . . . .	65
A.1 A stable manifold trajectory from family $a$ integrated forwards in time from the asteroid surface up to its period orbit. . . . .	74
A.2 Comparison between between orbit obtained in literature and the model developed in this work. The SRP acceleration is $\beta = 354.7336$ [- . . . . .	76
A.3 Variation of the Jacobi constant and $\beta$ in the AHP model eclipses for the orbit of family $a$ , seen in (a). (b) two periods; (c) one period. The initial conditions are $x_0 = 0.04195325$ , $\dot{y}_0 = 6.24192578$ [-] and $y_0, z_0, \dot{x}_0, \dot{z}_0 = 0$ . . . . .	77
A.4 Variation of the Jacobi constant and $\beta$ in the AHP model with eclipses for an orbit of family $g'$ , seen in (a). (b) two periods; (c) one period. The initial conditions are $x_0 = 0.04458068$ , $\dot{y}_0 = 5.88143855$ [-] and $y_0, z_0, \dot{x}_0, \dot{z}_0 = 0$ . . . . .	78
A.5 Comparison between the geometry of families of periodic orbits $a$ and $g'$ in the AHP model with eclipses and from literature. . . . .	79
A.6 Comparison of the stability index of families of periodic orbits $a$ and $f$ from the AHP model and from literature. . . . .	81
A.7 Comparison of the stability index from family of periodic orbits $g'$ from the AHP model and from literature. . . . .	82
A.8 Iterative process of the single-shooting differential corrector for an orbit of family $a$ with $\beta = 30$ . Figures (a)-(e) show the iteratively corrected orbit; figure (f) shows the magnitude of the correction at each iteration. Note that the orbit is corrected for half a period only. . . . .	82



# List of Tables

A.1	The two testing iterations for the validation and verification of the model. . . . .	74
A.2	Error associated with the maximum variation of the Jacobi constant for different trajectories in the AHP model. Initial conditions and period (or in the case of the random trajectories, integration time) are presented in non-dimensional units. . . . .	75
A.3	Error associated with the maximum variation of the Jacobi constant for different trajectories in the AHP model with the $J_2$ and $J_4$ gravity perturbations. Initial conditions are presented in non-dimensional coordinates. . . . .	75
A.4	Error associated with the maximum variation of the Jacobi constant for different trajectories in the AHP model with eclipses. Initial conditions are presented in non-dimensional coordinates. . . . .	77
A.5	Error associated with the integration and propagation of the state transition matrix for different trajectories in the AHP model. Initial conditions are presented in non-dimensional coordinates, and $z_0$ is zero for all orbits except for the terminator family, where $z_0 = 0.19962821$ for $\beta = 0$ and $z_0 = 0.03303122$ for $\beta = 100$ . . . . .	80
A.6	Error associated with the integration and propagation of the state transition matrix for different trajectories in the AHP model with the $J_2$ and $J_4$ gravity perturbations. Initial conditions are presented in non-dimensional coordinates, and $z_0$ is zero for all orbits except for the terminator family, where $z_0 = 0.32021070$ for $\beta = 0$ and $z_0 = 0.04221324$ for $\beta = 100$ . . . . .	80
A.7	Error associated with the integration and propagation of the state transition matrix for different periodic orbits in the AHP model with eclipses. Initial conditions are presented in non-dimensional coordinates, and $z_0$ is zero for all orbits except for the terminator family, where $z_0 = 0.19962821$ for $\beta = 0$ and $z_0 = 0.03303122$ for $\beta = 100$ . . . . .	80
A.8	Position error after one period in the AHP model for families of periodic orbits $a$ and $g'$ . Initial conditions are presented in non-dimensional coordinates, and $y_0, z_0, \dot{x}_0, \dot{z}_0 = 0$ . . . . .	83
A.9	Position error after one period in the AHP model with the $J_2$ and $J_4$ gravity perturbations for the families of periodic orbits $a$ and $g'$ . Initial conditions are presented in non-dimensional coordinates, and $y_0, z_0, \dot{x}_0, \dot{z}_0 = 0$ . . . . .	83
A.10	Position error after one period in the AHP model with eclipses for families of periodic orbits $a$ and $g'$ . Initial conditions are presented in non-dimensional coordinates, and $y_0, z_0, \dot{x}_0, \dot{z}_0 = 0$ . . . . .	83
A.11	Position error after one period in the full model (with eclipses and gravity perturbations), for families of periodic orbits $a$ and $g'$ . Initial conditions are presented in non-dimensional coordinates, and $y_0, z_0, \dot{x}_0, \dot{z}_0 = 0$ . . . . .	83
A.12	Comparison between results found by the differential corrector and those in literature, for $\beta = 0$ , for families of periodic orbits $a$ , $g'$ , and $f$ . . . . .	84
A.13	Comparison between results found by the differential corrector and those in literature, for $\beta = 33$ . . . . .	84





# Introduction

Ever since the dawn of humankind, we have been looking at the skies. The famous comet Halley, the first ever identified comet, was first described in a historical document by Chinese astronomers in 240 BC [1], far before the scientific revolution and enlightenment period. The exploration and pursuit of the secrets kept by the vast space above our heads have not only contributed to the technological development of the human species, but also brought us closer to the mysteries surrounding the origin of life. When the first near-Earth asteroid was discovered in 1898 by G. Witt [2], no-one imagined we would one day be stepping on the Moon, landing on Mars, on asteroids, or exploring the interstellar space beyond the solar system; and yet, here we are. The question then stands: what else can we still not imagine?

In the pursuit of knowledge and in the path leading to an interplanetary species, many stones are still left unturned. The asteroids and comets pertaining to the group of Near-Earth Objects (NEOs) certainly represent some of these "stones". Other than their wide scientific value, they hold an ever more significant position in the support of other areas, as planetary protection and asteroid mining. Their value and significance is a product of many factors, among them: their accessibility from Earth, their scientific content as remnants of the early days of the solar system, and their position in the solar system as possible "space stations" for interplanetary travel [3].

Due to their small size, asteroids typically exert small gravitational forces. As a consequence, even small perturbations can have a large effect on the objects orbiting an asteroid. This makes the dynamical space around asteroids particularly challenging to study and to design and operate space missions. Nonetheless, due to the reasons stated above, the design and study of these missions is a flourishing area, and expected to become increasingly prominent in the coming years.

A topic of particular interest to current and future space missions relates to the behavior and fate of asteroid ejecta in the dynamical environment surrounding these asteroids. While it was initially thought that asteroids smaller than a few tens of kilometers would be stripped of the fine and loose layer of rock that covers the surface of many bodies (known as regolith) [4], the wealth of information provided by previous missions and other numerical studies have helped prove otherwise. Nonetheless, and although studies on ejecta dynamics have taken place before, much is still unknown about the topic [5]. With this in mind, this thesis presents an in-depth investigation on the orbital motion of asteroid ejecta, as a product of an impact event by JAXA's Hayabusa2 mission.

In this chapter, we discuss some of the previous, current, and future missions to NEOs and establish the wide scope of interest and applicability of this thesis to future missions. Furthermore, we present a concise review on existing literature about the study of asteroid ejecta and the asteroid's dynamical environment, and present the research objectives and questions of this thesis.

## I.1. Missions to NEOs

The number of NEO missions has been increasing throughout the last decades. The consecutive accomplishments and the scientific data collected by some of these missions have greatly contributed to our understanding of asteroids and comets and enabled an abundance of technology demonstrations. These accomplishments have been, and continue to be, incorporated into other missions, thus advancing science, technology,

and the frontiers of space exploration. This section presents past, present, and future missions to NEOs, together with some of their achievements.

### **I.1.1. NEAR Shoemaker**

The first mission in NASA's Discovery Program was launched on February 1996 from Cape Canaveral and was the Near-Earth Asteroid Rendezvous (NEAR) Shoemaker mission [6]. The mission's goal was to study the second largest known near-Earth asteroid: 433 Eros. Eros is an S-type asteroid with approximately 17 km in diameter and a spin period of approximately 5.3 h<sup>1</sup>. The NEAR Shoemaker mission reached Eros in February 2000 and managed to successfully orbit the asteroid for a year, becoming the first ever mission to orbit an asteroid. The spacecraft gradually lowered its orbit until eventually soft-landing on the asteroid on February 2001, which marked the end of the mission. Besides obtained detailed information on the asteroid's gravity, shape, and spectroscopy, the mission showed significant quantities of regolith on the surface [7]. With all its accomplishments, the NEAR Shoemaker set an important milestone in the field of NEO missions, opening a pathway for future missions.



Figure I.1: Asteroid Eros as seen from NEAR. Courtesy of NASA<sup>2</sup>.

### **I.1.2. Hayabusa**

Hayabusa (initially known as MUSES-C) was JAXA's first asteroid mission and the first mission ever to successfully return an asteroid sample to Earth. After its launch in 2003, the spacecraft arrived at the subject of its mission, asteroid 25143 Itokawa, in 2005 [8]. Once at the asteroid, Hayabusa obtained an abundance of data relating to the asteroid's shape, density, topography, spin axis, and spectroscopy. It employed a hovering strategy over the asteroid, as opposed to orbiting, thus maintaining continuous control over the spacecraft. The sample collected from the S-type asteroid arrived back on Earth in 2010 [9]. Moreover, the mission also attempted to land a rover, MINERVA, on the surface, which was unsuccessful. The sample return marked a huge milestone in space science and mission design, allowing scientist to directly measure and study the components of an asteroid, and possibly compare them with observational data from other missions (such as NEAR) or other meteorite samples.

### **I.1.3. Deep Impact**

The Deep Impact mission from NASA is of particular significance to the study undertaken in this thesis. It studied comet 9P/Tempel and consisted of two companion spacecraft/modules. The spacecraft reached the comet on July 2005, and separated shortly after. One of the modules consisted of a 364 kg impactor spacecraft,

<sup>1</sup><https://ssd.jpl.nasa.gov/sbdb.cgi#top>; accessed 04-03-2019.

<sup>2</sup><https://photojournal.jpl.nasa.gov/catalog/PIA02923>; accessed on 28-02-2019.

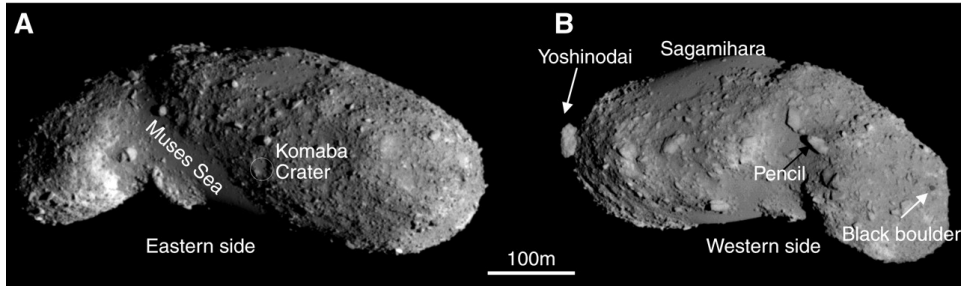


Figure I.2: Asteroid Itokawa as seen from Hayabusa. Courtesy of [10].

designed to excavate material from the comet that would be studied by the scientific instruments aboard the main spacecraft, at a safe distance of 500 km [11, 12]. The impactor spacecraft collided against the comet with a velocity of 10 km/s, as the mother-spacecraft probe flew-by the comet.

### I.1.4. Hayabusa2

Hayabusa2 is JAXA's second sample-return mission and the subject of the work presented in this thesis. The mission's goal is to investigate the C-type asteroid 1999 JU3, commonly known as asteroid Ryugu, with the purpose of returning a sample to potentially answer questions relating to the origins of water on Earth [13]. The spacecraft arrived at the asteroid at the end of June 2018, and at the time of writing, it has thus far successfully deployed two landers on the surface - becoming the first ever mission to successfully place a lander on an asteroid - and most recently completed the first of its three scheduled touchdowns to collect samples. Most notably, the mission plans to perform a ballistic impact on the surface of the asteroid, the topic investigated in this report, so as to create an artificial crater for observation and sample collection [14]. This will allow for a sample collection of the asteroid's subsurface layers that has not been subjected to space weathering [15]. The

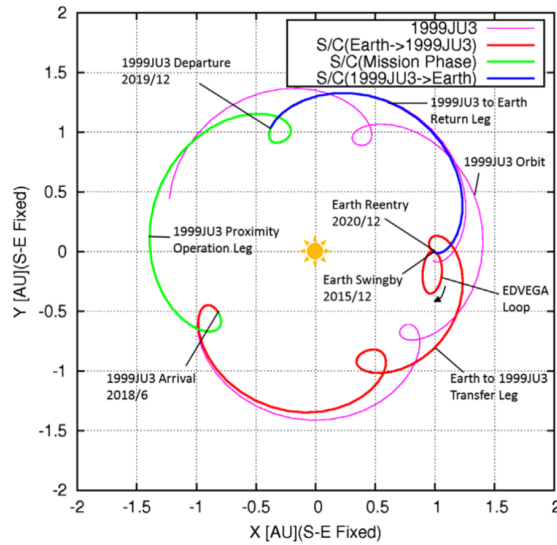


Figure I.3: Hayabusa2's mission timeline and trajectory design. The reference frame is centered on the Sun with the Earth situated in the positive  $x$ -axis. Courtesy of [13].

asteroid's small gravity and size make spacecraft operations challenging, which is why JAXA decided to continuously hover the spacecraft over the asteroid, at an approximate distance of 20 km along the asteroid-Earth line [13]. This same strategy was also used for Hayabusa, although Hayabusa2 will have a longer exploration phase (three months for Hayabusa and 18 months for Hayabusa2). This operational method also allows for continuous communication with the spacecraft. Asteroid Ryugu has an effective radius of 440 m and is in a heliocentric orbit with a period of 1.3 years. Data from the spacecraft's instruments has shown its surface to be extremely rocky and covered with boulders and regolith. After performing the planned operations, the collected samples will return to Earth via a re-entry capsule in 2020 [13]. Figure I.3 presents the timeline and

general trajectory design of the Hayabusa2 mission and Figure I.4 shows the surface of Ryugu as seen from the Hayabusa2 spacecraft.

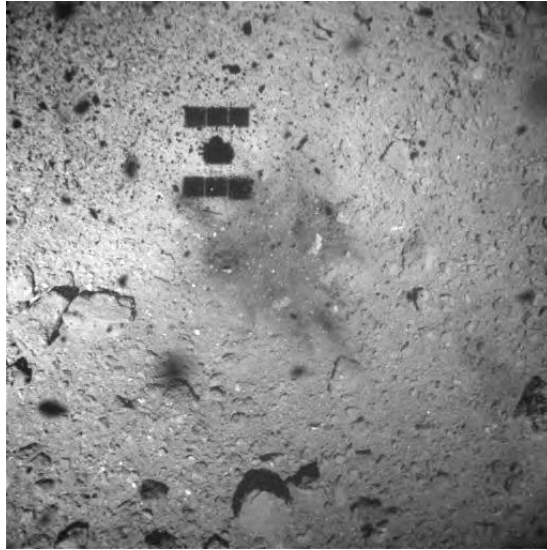


Figure I.4: Asteroid Ryugu as seen from Hayabusa2. Courtesy of JAXA, University of Tokyo, Kochi University, Rikkyo University, Nagoya University, Chiba Institute of Technology, Meiji University, University of Aizu, AIST<sup>3</sup>.

### I.1.5. OSIRIS-REx

The OSIRIS-REx mission from NASA is, at the time of writing, orbiting the subject of its mission: the C-type asteroid 101955 Bennu. The mission launched in 2016 and plans to touchdown on the asteroid surface to collect a sample through a touch-and-go sample-collection mechanism and return it to Earth for further analysis [16]. The sample is expected to arrive back on Earth in 2023. The mission was launched in September 2016 and arrived in close proximity of the asteroid at the end of 2018. Asteroid Bennu recently became the smallest object ever to be orbited by a spacecraft<sup>4</sup>. Figure I.5 shows the South pole of asteroid Bennu as seen from the OSIRIS-REx spacecraft.

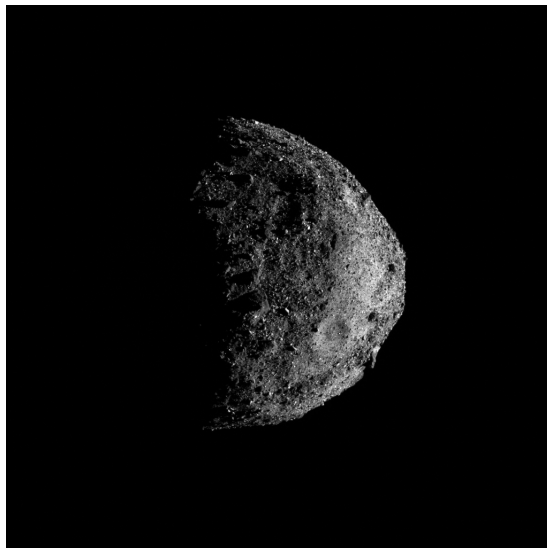


Figure I.5: Asteroid Bennu as seen from OSIRIS-REx. Courtesy of NASA, Goddard, and University of Arizona<sup>5</sup>.

<sup>3</sup>[http://www.hayabusa2.jaxa.jp/en/topics/20190225e\\_TD1\\_W1image/](http://www.hayabusa2.jaxa.jp/en/topics/20190225e_TD1_W1image/); accessed on 01-03-2019.

<sup>4</sup><https://www.asteroidmission.org/?latest-news=nasas-osiris-rex-spacecraft-enters-close-orbit-around-benu-breaking-record>; accessed on 04-03-2019.

### I.1.6. AIDA

The Asteroid Impact and Deflection Assessment (AIDA) mission is a planned joint mission between NASA and ESA to the binary asteroid 65803 Didymos. The mission consists of two separate missions: the Double Asteroid Redirection Test (DART) from NASA, led by the John Hopkins' Applied Physics Laboratory, and the Hera mission from ESA<sup>6</sup>. The DART mission will consist of a high velocity impact on the smaller body of the binary in 2022, in an effort to demonstrate asteroid deflection technology via kinetic impact [17]. The Hera counterpart spacecraft will arrive at the binary asteroid three years later to observe the impact site and aftermath of the event. Besides the asteroid deflection technology demonstration, the data collected by both spacecraft could provide important scientific return regarding both the internal composition of binary asteroids and the existence of long term bounded motion.

## I.2. Literature Review/State-of-the-art

Previous authors have considered the dynamics of asteroid/comet ejecta orbiting about small bodies. As mentioned, due to their generally small mass, the dynamical environment about small bodies is susceptible to perturbations that are commonly neglected when analyzing the orbital dynamics about larger bodies. One of the largest perturbations is usually posed by the solar radiation pressure (SRP) [18]. This creates a complex and highly-perturbed environment, especially for particles or spacecraft with large area-to-mass ratios, for which the intensity of the SRP accelerations is significantly larger [19]. For example, for ejecta particles, the smaller the radius, the larger the SRP acceleration.

The work by Scheeres et al. in [5] presents a comprehensive review regarding not only the perturbations experienced by asteroid ejecta, but also different approaches for modeling and studying the fate of these particles. In said paper, the different types of conditions that lead ejecta to either re-impact, be captured, or escape, are qualitatively divided into different groups. Scheeres et al. also study the different gravity modeling options one can take to describe the gravity of the asteroid. A remark is made with respect to the existence of bounded motion about an asteroid, referencing the fact that an orbit needs not to be mathematically stable to remain about an asteroid for long periods of time, which is referred to as temporary capture. Although the existence of these trajectories is acknowledged, the unanswered questions refer to the conditions that actually lead to temporary capture. This exact point is one of the main drives behind this thesis project.

The work in [20] studies the motion of ejecta particles about spherical comets that are in eccentric orbits about the Sun using an analytical method to compute the motion of the ejecta particles under SRP-perturbed environments over long periods of time. The method, called Radiation Pressure Approximation (RPA), uses averaged solutions for the computation of the particle's angular momentum and eccentricity, as an explicit function of the true anomaly. This method is recovered in [21] by Scheeres and Marzari to study the possibility of temporary orbital capture following the impact of the Deep Impact mission on comet 9P/Tempel. Scheeres and Marzari find initial conditions, which, under the RPA method, lead to long periods of orbital capture. Although these works are applied to comets, they could be transformed to analyze temporary capture about asteroids. Nonetheless, in these works the effects the body's irregular gravity field or eclipses are not taken into account.

In [22], Scheeres et al. study the orbital environment about asteroid 4769 Castalia in the dynamical framework of the two-body problem with a detailed gravity model in its spherical harmonics expansion, which is computed from a radar-derived physical shape model. Several types of orbital motion are studied, and applied to both ejecta particles and spacecraft. Although this paper does not include perturbations other than the irregular gravity field of the uniformly rotating asteroid, it presents trajectories leading to the equilibrium points of the system by following their stable manifolds, a similar approach to that employed in this thesis.

Although this thesis approaches the topic of ejecta dynamics from an astrodynamics point of view, previous authors have studied the ejection dynamics from an impact cratering stand-point by analyzing the geological properties of the body's surface [23]. A common approach in this field is to employ empirically obtained scaling laws that make use of small-scale laboratory experiments to describe the ejection conditions of the material and the crater-forming processes. These laws have also been employed to study the cratering event of the Deep Impact mission in [24] and [25].

<sup>5</sup><https://www.asteroidmission.org/galleries/spacecraft-imagery/>; accessed on 01-03-2019.

<sup>6</sup>[https://www.esa.int/Our\\_Activities/Space\\_Engineering\\_Technology/Hera/Asteroid\\_Impact\\_Deflection\\_Assessment\\_AIDA\\_mission](https://www.esa.int/Our_Activities/Space_Engineering_Technology/Hera/Asteroid_Impact_Deflection_Assessment_AIDA_mission); accessed on 28-02-2019.

A further exposition of previous research regarding the dynamics in the vicinity of small bodies and the framework of the traditional Hill Problem [26, 27], the Augmented Hill Problem (AHP) [18, 28], and the AHP with eclipses [29], is exposed in Chapter II of this thesis. So as not to repeat information, this section only exposes previous research in the field of asteroid or comet ejecta about small bodies.

Nonetheless, from the presented research, we find that the study of asteroid ejecta and their temporary capture has yet to be studied in a dynamical environment that considers the SRP, eclipses, and the oblateness of the small body. Previous research considers either high-fidelity gravity models in a two-body problem, ignoring the SRP, or takes into account the SRP but ignores the effects of eclipses and models the asteroid's gravity as a point mass. The study presented in this thesis thus aims at contributing to this topic by studying the conditions necessary for ejecta particles to be temporarily captured in periodic orbits, using a model that considers the SRP, the effect of eclipses, and the oblateness of the asteroid.

### I.3. Research Questions

The goal of this thesis is to study the conditions for which asteroid ejecta could be temporarily captured into periodic orbits following an impact event on the surface of the asteroid. It is directly applied to the Hayabusa2 mission from JAXA, which is the motivation behind this research. It aims at assessing whether the trajectories followed by the ejecta particles from the asteroid surface could pose a hazard to the mission or the spacecraft, taking into account that a collision with the ejecta particles could limit the performance of the spacecraft. Taking this information into account, we formulate the following main research question:

**Can ejecta that is temporarily captured into periodic orbits following Hayabusa2's SCI operation pose a danger to the spacecraft?**

With the purpose of elaborating a solid structure for the research process, the main research question can be further divided into the following sub-questions:

1. What type of dynamical environment exists about asteroid Ryugu and what is the effect of the perturbations posed by the SRP, eclipses, and the  $J_2$ ,  $J_4$  terms of the asteroid's gravity potential expansion?
2. What are the initial conditions that lead ejecta particles to periodic orbits and thus temporary capture?
3. For what duration do the ejecta particles remain captured about the asteroid?
4. What is the effect of particle radius in the dynamics experienced by the ejecta particles, in terms of temporary capture?
5. What trajectories do the captured ejecta particles follow and do they pose a danger to the Hayabusa2 spacecraft?
6. What are the best and worst impact locations for the SCI in terms of possibility of temporary capture and safety of the spacecraft?

### I.4. Thesis Structure

Following this introductory chapter where the motivation and research objectives of this thesis were presented, Chapter II presents the main body of research in the form of a self-contained draft journal article. It includes an introduction where a more detailed overview of previous work on the dynamical framework on which this thesis is based is presented, together with a comprehensive review of research relevant to this work. We present the dynamical model used and its equations of motion, relevant background knowledge and methodology, considerations on impact dynamics and their relation with the studied SCI operation from an astrodynamics perspective, the results of the research, and the conclusions of said research.

Chapter III recovers the research objectives and questions, in order to review to what degree they were fulfilled. In the same chapter we also make recommendations for future work on the topic of this thesis and present another promising application for the implemented methodology, presenting some preliminary results. In Appendix A we present the verification and validation of the model and of the tools developed for this thesis.



## Journal Article

This chapter presents the main results of this thesis research project in the form and style of a draft journal article. It is thus a self-contained document, albeit included in the body of this report.

# Temporary Capture of Asteroid Ejecta into Periodic Orbits: Application to JAXA's Hayabusa2 Impact Event

Daniel Villegas Pinto \*  
*Delft University of Technology, 2629 HS Delft, The Netherlands*

In the framework of JAXA's Hayabusa2 mission, we study the dynamical environment around asteroid Ryugu to investigate whether ejecta particles can be temporarily trapped in periodic orbits following the Small Carry-on Impactor (SCI) operation. If these particles remain about the asteroid, they could potentially jeopardize the mission as, in the event of a collision with the Hayabusa2 spacecraft, the spacecraft's functionality could be reduced. In this paper, we make use of invariant manifold theory to assess the conditions - impact location, particle radius, ejection velocity - that cause ejecta particles to get captured in periodic orbits. The analysis is carried out within the dynamical framework of the perturbed Augmented Hill Problem, which takes into account the solar radiation pressure, the effect of eclipses, and the  $J_2$  and  $J_4$  terms of the asteroid's gravity potential in its spherical harmonics expansion. We analyze millimeter to centimeter sized particles and captures into three families of periodic orbits that are robust to large values of the solar radiation pressure acceleration – the traditional  $a$  and  $g'$  families of the Hill Problem and the southern halo orbits. We go on to find the impact locations for the SCI from where ejecta particles are most likely to be captured into periodic orbits via their stable manifolds. As such, we recover the sets of initial states that lead ejecta to temporary orbital capture and show that solar radiation pressure cannot be neglected in these analyses, identifying locations on the Sun side of the asteroid at medium latitudes as the best impact locations.

## Nomenclature

$a, b, c$	= Asteroid axes, m
$a_p$	= Perturbing acceleration, $m/s^2$
$a_{SRP}$	= Dimensional solar radiation pressure acceleration, $m/s^2$
$A$	= Exposed surface area, $m^2$
$C_{lk}$	= Stokes coefficients of order $l$ and degree $k$
$C_R$	= Reflectivity coefficient or albedo

---

\*d.e.villegaspinto@student.tudelft.nl

$d_a$	=	Mean distance between Sun and asteroid
$g$	=	Sigmoid function
$J$	=	Jacobian
$J_2, J_4$	=	Gravitational oblateness terms due to the $C_{20}$ and $C_{40}$ Stokes coefficients, respectively
$m$	=	Mass, kg
$P_0$	=	Solar constant, $\text{kg m/s}^2$
$\mathbf{r}$	=	Position vector of particle, m (or km or dimensionless)
$r_x$	=	Distance to $x$ -axis, m (or dimensionless)
$\mathbf{R}$	=	Reference frame
$R$	=	Ejecta particle radius, cm
$R_a$	=	Average asteroid radius, m
$s$	=	Contrast factor for sigmoid function
$t$	=	time, s (or dimensionless)
$T$	=	Period, s (or dimensionless)
$T_a$	=	Asteroid period about Sun
$U$	=	Gravity potential in spherical harmonics, $\text{m}^2/\text{s}^2$ (or dimensionless)
$U_x, U_y, U_z$	=	Gravity accelerations in cartesian coordinates for spherical harmonics, $\text{m/s}^2$ (or dimensionless)
$\tilde{U}$	=	Effective potential, dimensionless
$\mathbf{v}$	=	Eigenvector
$v_{ej}$	=	Ejection velocity, m/s (or dimensionless)
$V$	=	Kinetic energy, dimensionless
$\mathbf{X}$	=	State vector, m and m/s (or dimensionless)
$\beta$	=	Solar radiation pressure acceleration, dimensionless
$\epsilon$	=	Small perturbation
$\zeta$	=	Right ascension in the Hill frame, deg (or rad)
$\delta$	=	Declination, deg (or rad)
$\Delta$	=	Variation or error
$\lambda_i$	=	Eigenvalues of Monodromy matrix
$\mu$	=	Asteroid gravitational parameter, $\text{m}^3/\text{s}^2$
$\mu_S$	=	Sun gravitational parameter, $\text{m}^3/\text{s}^2$
$\rho$	=	Density, $\text{kg/m}^3$
$\sigma$	=	Ejection angle with respect to surface normal, deg (or rad)

$\tau$	=	Half-period, s (or dimensionless)
$\Phi$	=	State transition matrix
$\Phi_M$	=	Monodromy matrix
$\omega$	=	Mean motion of asteroid about Sun, rad/s
$\hat{\square}$	=	Unit vector
$\dot{\square}$	=	First-order derivative with respect to time
$\ddot{\square}$	=	Second-order derivative with respect to time

*Subscripts/Superscripts*

$\square_0$	=	Initial condition
$\square_{ej}$	=	Ejection condition
$\square_{Hill}$	=	In the Hill frame
$\square^U$	=	Unstable
$\square^S$	=	Stable

## I. Introduction

With the increased attention that the topic of small bodies has received in the past few decades, we have seen the space community motivated more than ever by the scientific value that missions to Near-Earth Objects (NEOs) offer. The answers to the origins of the solar system and water on Earth may very well lie within the knowledge kept by these small bodies of our solar system [1] and this quest has pushed forward a number of missions. From NASA's NEAR Shoemaker mission orbiting an asteroid for the first time [2], JAXA's Hayabusa mission returning an asteroid sample for the first time in history [3, 4], ESA's ROSETTA mission [5, 6], NASA's Deep Impact mission [7, 8], up to the mission on which the work here presented is applied to, JAXA's Hayabusa2, a sample-return mission to the C-type near-Earth asteroid 1993 JU3, also known as asteroid Ryugu.

After having arrived at asteroid Ryugu at the end of June 2018, Hayabusa2 is now in the process of planning to fire its Small-Carry-on-Impactor (SCI) at the asteroid with the purpose of collecting subsurface material from the created crater via a third and final touchdown [9]. While preliminary studies assumed that the asteroid ejecta generated from this event would be cleared within less than 30 days [10], other studies (such as [11]) and observations (such as [12], where an asteroid was observed to have a debris trail, likely resultant of a collision) show the possibility of dust particles remaining about the asteroid for long periods of time. Due to the small mass of the asteroid, the dynamical environment of the ejecta is highly perturbed by solar radiation pressure (SRP). Although these conditions are often disruptive to

the possibility of bounded motion, they may give rise to scenarios that result in temporary capture (as proven by the observations detailed in [12]), posing a danger to the mission in case of a collision with the spacecraft. Moreover, temporary capture of ejecta particles about the asteroid could prevent the spacecraft from approaching the asteroid to complete its final sample collection of the subsurface material excavated by the ballistic impact. This is thus the motivation for the undertaking of this work; its purpose is to assess the conditions that can cause asteroid ejecta to remain trapped in periodic orbits about asteroid Ryugu following the impact event on its surface.

The dynamical environment presented here is, at its core, based on a particular case of the Circular Restricted Three-Body Problem (CR3BP) [13, 14] commonly known as the Hill Problem. The Hill Problem describes the scenario where the dynamics are situated in the vicinity of the secondary body and the mass of the secondary body is much smaller than that of the primary; it was first introduced in 1878 by George Hill [15] and used to describe dynamics about the Moon. It is a common approach when analyzing the orbital dynamics about NEOs and has been employed in previous works [11, 14, 16–18]. However, the classical Hill Problem does not include the effect of the SRP, which is a major perturbation of the system under consideration [14, 19]. Also known as the Photogravitational Hill Problem [20], the extension of the Hill Problem to the case of a radiating primary is here referred to as the Augmented Hill Problem (AHP). The model used in this paper is a further extension of the AHP, here referred to as the perturbed AHP, which also includes the effect of eclipses and the asteroid's  $J_2$  and  $J_4$  terms of its spherical harmonics gravity potential expansion.

Several orbital dynamics studies have been carried out under the AHP model. In [20], an extensive search and analysis of families of planar periodic orbits is undertaken for very small values of SRP acceleration. The AHP has also been used to study the dynamics of solar-sails about asteroids, as seen in [21–24]. Specifically, the work in [21] shows how a spacecraft can take advantage of the SRP to remain bounded to the asteroid's vicinity for long periods of time. In [25], Broschart and Villac explore an orbit family previously presented in [26–28], known as the terminator family (the equivalent of the southern halo orbits in the CR3BP [29]), which is shown to exhibit long-term stability in heavily SRP-perturbed environments and robustness against gravitational uncertainties. This type of orbit and its quasi-periodic family branches are further analyzed in [30]. Also of interest are the works presented in [31] and [32], where families of periodic orbits for large values of SRP acceleration are analyzed. Specifically, in [31], various families of three-dimensional symmetric periodic orbits are analyzed as orbiting possibilities for Hayabusa2 about asteroid Ryugu. In [32], planar orbit families of the Hill Problem are continued into and analyzed in the AHP up to very high values of SRP. The work in [32] also presents the effect of eclipses on the family-parameter curve and the shape of these orbit families, which proves especially relevant when considering large values of SRP acceleration and is further explored in this paper.

In [19], Scheeres et al. present an extensive review on the types of trajectories ejecta particles can take after being lofted from an asteroid's surface, which perturbations should be taken into account, and possibilities regarding the modeling of these trajectories and particles. They present basic dynamical equations and models, and a classification

scheme for the possible fate of the ejecta particles. In [33], the dynamics of ejecta particles in close-proximity of asteroid 4769 Castalia are studied extensively using a radar-derived shape model. Although the model considers only the asteroid’s gravity, ranges of velocities that guarantee either re-impact or escape are obtained and remarks relating to capture conditions are addressed. Scheeres and Marzari [11] simulate extensive sets of initial conditions via an analytical method to find those that cause dust particles to be temporarily trapped about comet 9P/Tempel after ejection from its surface. Soldini and Tsuda [34] study the fate of asteroid ejecta about asteroid Ryugu by simulating different initial conditions and integrating them forwards in time, both in the two-body problem and the AHP, leading to conclusions on the fact that smaller particles (large values of SRP acceleration) are likely to escape or re-impact faster.

All these works form a basis for the general understanding that (quasi)-periodic orbits can exist in the heavily-perturbed orbital environment about NEOs. The problem investigated in this paper builds on these works by investigating the sets of initial conditions that enable millimeter- to centimeter-sized asteroid ejecta to get captured into periodic orbits and consequently pose a danger to the Hayabusa2 spacecraft. In this paper, these initial conditions are found by making use of the stable invariant manifolds of periodic orbits, to find trajectories that lead from the asteroid surface to said orbits. The proposed method departs from the more common approach of simulating wide ranges of initial conditions to find the ones that lead to temporary captured motion – as done in [11, 34] –, thus closing the knowledge gap on specific conditions that lead to temporary capture into periodic orbits.

This paper is structured as follows. We first introduce the dynamical models and equations of motion used, presenting the AHP model, eclipse model, and gravity model that includes the asteroid’s  $J_{20}$  and  $J_{40}$  terms of the body’s gravity potential spherical harmonics expansion – here referred to as  $J_2$ ,  $J_4$  for conciseness. We also specify how the dust particles that compose the asteroid ejecta are modeled. Following this, the methodology is presented, regarding periodic orbits, their computation and their study in the different models. We then detail the used approach, with its assumptions and considerations, thus linking the theoretical background with its practical applications. This is followed by the presentation of the results for the planar and three-dimensional cases, the implications of said results for the Hayabusa2 mission and, finally, the conclusions of the work.

## II. Dynamical Model

This section presents the models and theoretical background used throughout this work. The asteroid is assumed to be on a circular orbit about the Sun with constant mean motion  $\omega$ , and is initially modeled as a point mass for the AHP and the eclipse models. Later, the  $J_2$  and  $J_4$  (i.e.,  $C_{20}$  and  $C_{40}$  Stokes coefficients) gravitational terms are implemented. Other forces such as electromagnetic forces, the Poynting-Robertson effect, or the Yarkovsky effect are neglected due to their very small intensity and the fact they only act on very long time scales [35]. Moreover, we neglect collisions between particles.

A rotating reference frame is adopted,  $\mathcal{R}_1(\hat{x}_{Hill}, \hat{y}_{Hill}, \hat{z}_{Hill})$ , hereon referenced as the Hill frame. The Hill frame is

centered in the center of mass of the asteroid, its  $x$ -axis points in the anti-solar direction at all times, its  $z$ -axis points in the direction of the asteroid's orbit angular momentum vector, and the  $y$ -axis completes the orthogonal frame.

### A. The Augmented Hill Problem

As previously mentioned, the AHP and Hill Problem are derived from the CR3BP, by approximating the dynamics to the vicinity of the secondary body, in this case the asteroid [17, 36]. Following [11, 14], the equations of motion are normalized using as unit of length  $[l] = (\mu/\omega^2)^{1/3}$  and as unit of time  $[t] = 1/\omega$ , where  $\mu$  is the asteroid's gravitational parameter. They take the form

$$\ddot{x} - 2\dot{y} = -\frac{x}{r^3} + 3x + \beta \quad (1)$$

$$\ddot{y} + 2\dot{x} = -\frac{y}{r^3} \quad (2)$$

$$\ddot{z} = -\frac{z}{r^3} - z \quad (3)$$

where  $r = \sqrt{x^2 + y^2 + z^2}$  and  $\beta$  is the non-dimensional SRP acceleration. The approximation to the vicinity of the asteroid, or secondary body, means we include the Sun's third-body effect in the dynamics instead of the absolute gravitational attraction felt by the particle from the Sun [14].

The SRP is assumed to be constant and acting along the Sun-asteroid direction. The non-dimensional SRP acceleration,  $\beta$ , is then obtained by normalizing the traditional SRP acceleration,  $a_{SRP}$ , for a cannonball model [14, 30, 37], i.e., with a constant exposed area and attitude, which yields

$$\beta = \frac{a_{SRP}}{[l]/[t]^2} = \frac{(1 + C_R)P_0}{m/A \mu^{1/3} \mu_S^{2/3}} \quad (4)$$

where  $C_R$  is the reflectivity coefficient or albedo,  $P_0 \approx 1.02 \times 10^{17}$  kg m s<sup>-2</sup> is the solar constant,  $m/A$  is the mass-to-area ratio, and  $\mu_S$  is the gravitational parameter of the Sun.

The system presented in Eqs.(1)-(3) admits an energy integral,  $C$ , known as the Jacobi Constant [14]

$$C = 2\tilde{U} - V^2 = 3x^2 + 2\beta x + \frac{2}{r} - z^2 - (\dot{x}^2 + \dot{y}^2 + \dot{z}^2) \quad (5)$$

where  $\tilde{U} = \frac{3}{2}x^2 + \beta x + \frac{1}{r} - \frac{z^2}{2}$  and  $V = \sqrt{(\dot{x}^2 + \dot{y}^2 + \dot{z}^2)}$  represent, respectively, the effective potential and kinetic energies of the system [14]. Since  $V$  cannot be negative, we can write  $V^2 = 2\tilde{U} - C \geq 0$ , which translates into the

regions of accessible and forbidden motion of a particle, i.e.,  $2\tilde{U} \geq C$ . The boundaries of these regions are called Zero-Velocity Curves (ZVC) and can give us important insights into the motion of particles in three-body systems [36].

By setting the left-hand side of Eqs.(1)-(3) to zero, we find the Lagrangian equilibrium points of the system. Contrary to the traditional CR3BP, the system admits only two equilibrium points,  $L_1$  and  $L_2$ , both of them on the  $x$ -axis. For  $\beta = 0$  these are easily found for  $x = \pm(\frac{1}{3})^{\frac{1}{3}}$ , while for  $\beta \neq 0$  they are found by choosing the real roots of the polynomials  $3x^3 + \beta x \pm 1 = 0$ . The equilibrium point  $L_1$  lies along the negative  $x$ -axis, i.e., on the asteroid's Sun side, and  $L_2$  along the positive side of the  $x$ -axis. It is important to note that an increase in SRP acceleration causes the  $L_1$  point to move towards the Sun and the  $L_2$  point to asymptotically move towards the asteroid. This can be seen in Figure 1a, which shows the positions of the  $L_1$  and  $L_2$  points of the system for different values of  $\beta$ . In this paper, we consider ejecta particles from millimeter to centimeter sizes, which in turn translate into a large range of  $\beta$  values (see Table 2). For this reason, the  $L_1$  point loses its significance to our analysis, as it is too far from the asteroid. Figures 1b and 1c present the ZVCs of the system for  $\beta$ -values of 0 and 30; here too we can see how the geometry of the regions of allowed and forbidden motion is affected by the SRP. The effect of the SRP on the dynamics of the system is a critical component of the analysis undertaken in this work, and a recurring theme.

**Table 1 Asteroid Ryugu Properties [34, 38]**

$\mu$ [ $\text{m}^3 \text{s}^{-2}$ ]	Asteroid axes [m]			Avg. radius, $R_a$ [m]	Orb. period, $T_a$ [days]	Density, $\rho$ [ $\text{kg}/\text{m}^3$ ]	$C_R$
	a	b	c				
32	446.5	439.7	433.9	440	473.889287	1270	0.07

From Eq. (4), we see that the intensity of the SRP acceleration will vary only with the particle's mass-to-area ratio. In this work, the ejecta particles are modeled as spheres of constant density and have material characteristics equal to those of asteroid Ryugu, i.e., with the same density,  $\rho$ , and reflectivity,  $C_R$ . The properties of asteroid Ryugu are shown in Table 1, where the orbital period of the asteroid about the Sun,  $T_a$ , is used to compute the mean motion of the asteroid,  $\omega = 2\pi/T_a$ . For the mass-to-area ratio of the ejecta particles, we use

$$m/A = \frac{4/3\rho\pi R^3}{2\pi R^2} = \frac{2}{3}\rho\pi R \quad (6)$$

where  $R$  is the particle's radius, and only the area exposed to the SRP is considered. Eq. (6) hence translates into a linear variation of  $\beta$  with the particle radius  $R$ , where the smaller the radius, the larger the SRP acceleration. Table 2 shows the relation between different values of  $\beta$ , the radius and area-to-mass ratio, the dimensional value of the SRP acceleration,  $a_{SRP}$ , and the  $x$  coordinate of the second Lagrangian equilibrium point,  $x_{L_2}$ , together with its corresponding Jacobi constant,  $C_{L_2}$ . Note that even for a spacecraft, the SRP acceleration values about Ryugu are significant. For instance, for the Hayabusa2 spacecraft its non-dimensional SRP acceleration is situated between  $\beta = 40$  and  $\beta = 50$ , for an

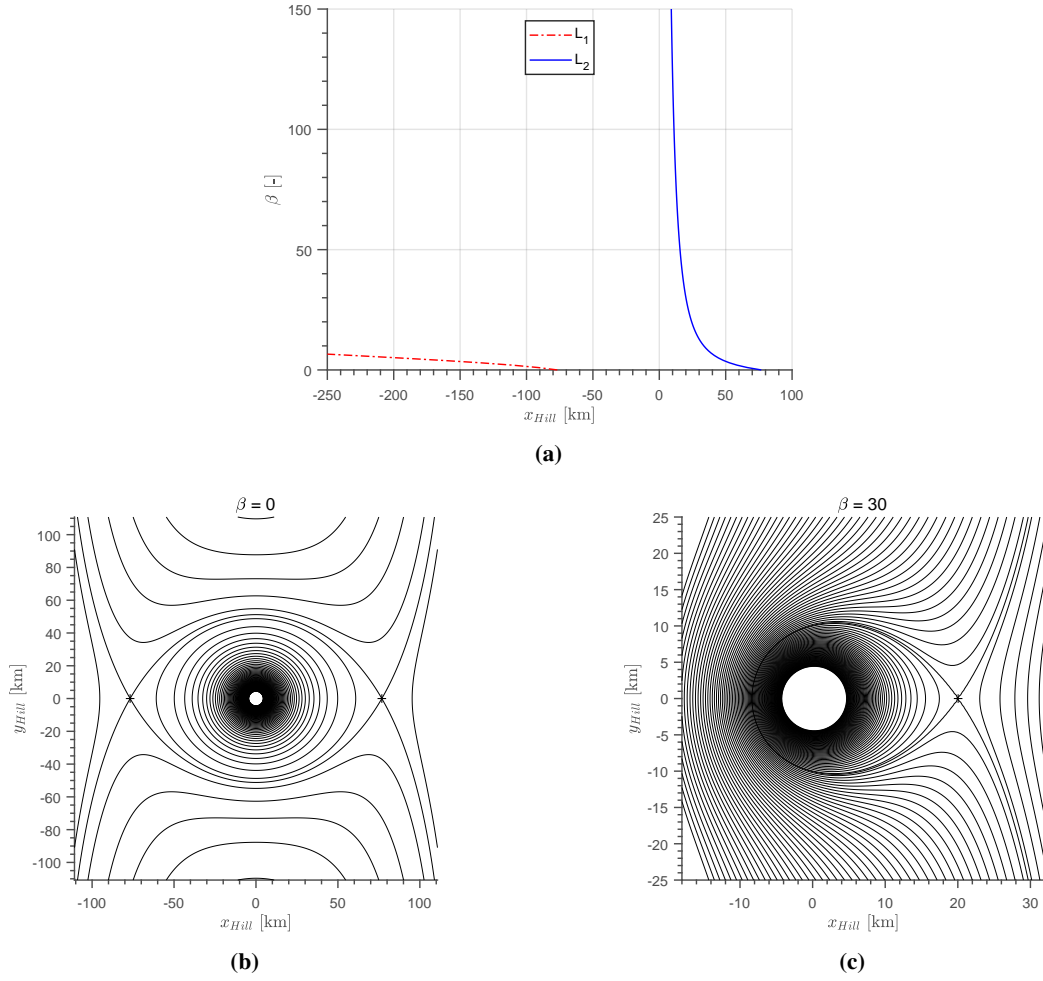


**Fig. 1** The effect of solar radiation pressure ON the dynamics of the AHP: (a) variation of the equilibrium points with  $\beta$ ; (b) ZVCs for  $\beta = 0$ ; (c) ZVCs for  $\beta = 30$ . The equilibrium points are marked with a cross.

mass-to-area ratio of  $35 \text{ kg/m}^2$  [31] and an albedo of 0.3. Finally, in order to analyze millimeter to centimeter sized particles, we focus on  $\beta$  values ranging between  $\beta = 30$  and  $\beta = 200$  for the remainder of this paper, highlighted in Table 2.

## B. Eclipse Model

Given the magnitudes of SRP accelerations considered, eclipses are likely to pose a significant perturbation to the particles whose trajectories or orbits cross the eclipse region. To model this perturbation, a simple cylindrical eclipse model is adopted. This model is used instead of a conical model due to the negligible impact that the conical model would have on the system, given the small size of the asteroid and the large distance from the Sun [39]. We simulate the transition between the eclipse and sunlit regions by means of a modified sigmoid function [40, 41] of the form

**Table 2** Relationship between non-dimensional SRP acceleration ( $\beta$ ), mass-to-area ratio ( $m/A$ ), particle radius ( $R$ ), dimensional SRP acceleration ( $a_{SRP}$ ), Jacobi constant of the  $L_2$  point ( $C$ ), and position of the  $L_2$  point ( $x_{L_2}$ ).

$\beta$	$\frac{m}{A}$	$R$ [cm]	$a_{SRP}$ [mm/s <sup>2</sup> ]	$C_{L_2}$ [-]	$x_{L_2}$ [km]
0	-	-	0	4.327	76.8
1.0	1322.0	156.1	$2.608 \times 10^{-6}$	5.613	66.26
5.0	264.4	31.23	$1.304 \times 10^{-5}$	9.48	44.47
10.0	132.2	15.61	$2.608 \times 10^{-5}$	12.94	33.54
30.0	44.06	5.204	$7.825 \times 10^{-5}$	22.01	20.04
50.0	26.44	3.123	$1.304 \times 10^{-4}$	28.34	15.6
100.0	13.22	1.561	$2.608 \times 10^{-4}$	40.03	11.06
200.0	6.61	0.7807	$5.217 \times 10^{-4}$	56.58	7.828
300.0	4.406	0.5204	$7.825 \times 10^{-4}$	69.29	6.393
500.0	2.644	0.3123	$1.304 \times 10^{-3}$	89.45	4.953

$$g(\chi) = \frac{1}{1 + e^{-s\chi}} \quad (7)$$

where  $\chi$  is the input and  $s > 0$  is often referred to as the contrast factor term, which defines the steepness and "length" of the transition. The function will take an "S" shaped curve, behaving as a smooth Heaviside function, passing from 0 to 1 after  $\chi$  becomes positive. Using this function, we can redefine the value for the SRP acceleration,  $\beta^*$ , as

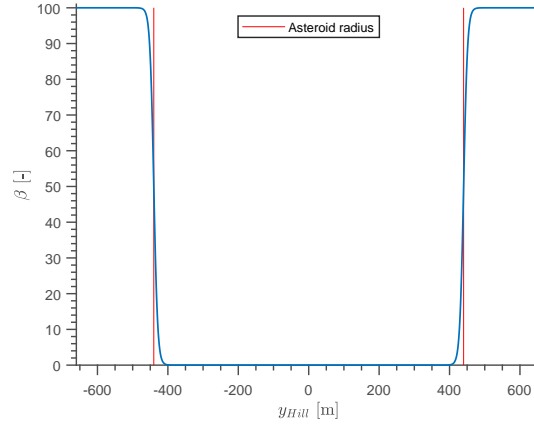


**Fig. 2** Variation of non-dimensional SRP acceleration as a particle transitions through the eclipse region in the  $xy$ -plane.

$$\beta^* = \begin{cases} \beta & \text{if } x \leq 0 \\ \beta g(r_{sig}) & \text{otherwise} \end{cases} \quad (8)$$

where  $r_{sig} = (r_x - R_a)$ , and  $r_x$  is the distance to the  $x$ -axis,  $r_x = \sqrt{y^2 + z^2}$ . Figure 2 shows the value of  $\beta^*$  for  $x > 0$ ,  $z = 0$ , and  $\beta = 100$ , when passing through an eclipse region.

### C. Gravity Perturbations

To better represent the physical environment experienced by ejecta particles around asteroid Ryugu, a higher-fidelity representation of the asteroid's gravity is presented by considering the  $J_2$  and  $J_4$  terms of its spherical harmonics gravity potential expansion. The common notation  $J_2 = -C_{20}$  and  $J_4 = -C_{40}$  is used, where  $C_{lk}$  refers to the term of the Stokes coefficients with degree  $l$  and order  $k$  [42]. Previous work has analyzed the effect of the oblateness of the secondary in both the AHP [43] and the CR3BP [44]. Asteroid Ryugu's  $J_2$  and  $J_4$  terms are therefore included in the dynamics to obtain a more realistic model.

Data from the Hayabusa2 team have shown that asteroid Ryugu's spin-axis is oriented approximately normal to its orbital plane. Since it spins about its shortest axis,  $c$ , i.e., the axis with largest moment of inertia [14], we can include the gravity perturbations of the  $C_{20}$  and  $C_{40}$  terms without affecting the existing dynamical symmetry of the system with respect to the  $xz$ -plane: because we only consider the terms with order  $k = 0$ , the gravity acceleration will only vary with latitude, and not with longitude, removing the need to track the spin-state of the asteroid and retaining a time-invariant system.

We can then write for the Stokes coefficients [26]

$$C_{20} = \frac{1}{10r_0^2} (2c^2 - a^2 - b^2) \quad (9)$$

$$C_{40} = \frac{3}{280r_0^4} \left[ 3(a^4 + b^4) + 8c^4 + 2a^2b^2 - 8(a^2 + b^2)c^2 \right] \quad (10)$$

where  $r_0$  is the effective radius, taken to be the average radius of the asteroid. Note that since we consider only the Stokes coefficients with order zero (and degrees two and four), we can use the Hill frame to define the gravity potential of the asteroid, and do not need to perform the usual reference frame transformation from the body-fixed frame to the rotating Hill frame. The non-dimensional gravity potential in its spherical harmonics expansion then becomes [45]

$$U(r, \delta) = \frac{1}{r} \left[ 1 + \left( \frac{r_0}{r} \right)^2 \left( \frac{1}{2} C_{20} (3 \sin^2 \delta - 1) \right) + \left( \frac{r_0}{r} \right)^4 \left( \frac{1}{8} C_{40} (35 \sin^4 \delta - 30 \sin^2 \delta + 3) \right) \right] \quad (11)$$

where  $\delta$  is the particle's declination in the Hill frame. Expressing  $r$  and  $\delta$  in Cartesian coordinates and differentiating with respect to  $x$ ,  $y$ , and  $z$ , we can derive the accelerations in the respective directions, i.e.,  $U_x, U_y, U_z$ . The equations of motion presented in Eqs. (1)-(3) then become

$$\ddot{x} - 2\dot{y} = U_x + 3x + \beta \quad (12)$$

$$\ddot{y} + 2\dot{x} = U_y \quad (13)$$

$$\ddot{z} = U_z - z \quad (14)$$

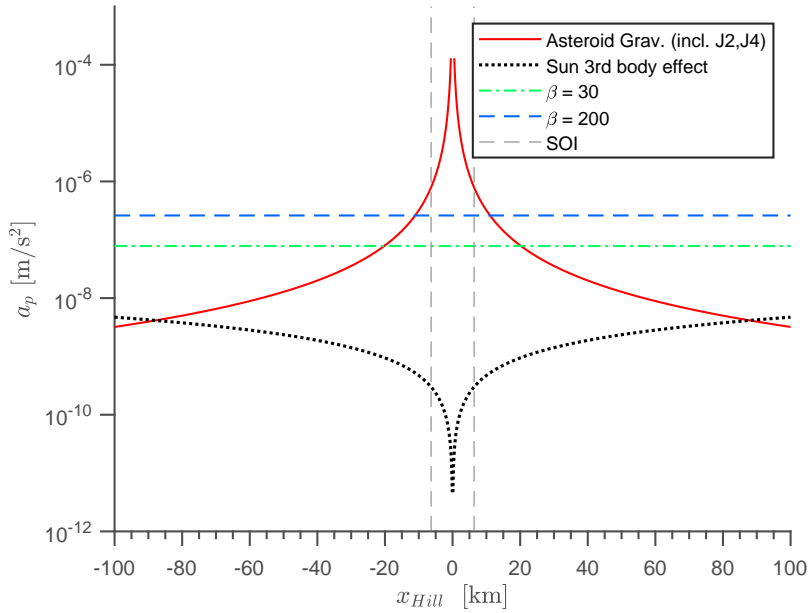


**Fig. 3 Magnitude of the perturbing accelerations about Asteroid Ryugu as a function of the  $x$ -coordinate.**

Finally, as a concluding remark regarding the incorporation of the different perturbations considered for the model in this paper, we analyze the magnitudes of the various perturbing accelerations,  $a_p$ , to a particle about asteroid Ryugu. Figure 3 shows the dimensional accelerations of the different perturbing sources along the  $x$ -axis, where we also include the Sphere of Influence (SOI) of the asteroid,  $R_{SOI} = d_a(\mu/\mu_S)^{2/5}$  [13], where  $d_a$  is the mean distance from the Sun to the asteroid. As expected, the gravitational acceleration is the main perturbation when in close-proximity to the asteroid.

However, just outside the SOI, the magnitudes of the SRP accelerations are close to the same orders of magnitude of the asteroid's gravity acceleration, and actually become larger for distances larger than 12 km for  $\beta = 200$  ( $R = 7.8$  mm) and larger than 20 km for  $\beta = 30$  ( $R = 5.2$  cm). The Sun's third-body effect remains the smallest perturbation for distances smaller than approximately 88 km from the asteroid. For larger distances it becomes more significant than the asteroid's gravity. We note the relevance of the SRP to the dynamics of the problem and, therefore, the importance of including said eclipses in the system (for trajectories or orbit that cross the eclipse regions).

### III. Periodic Orbits

This section presents the methodology used in this work, related to the computation and analysis of periodic orbits. The orbit families studied in this paper are also presented and analyzed in terms of stability, geometry, and the effects of the different perturbations to the system.

#### A. Symmetries

The system presented in the previous section displays the following symmetries [46, 47]

$$(y, t) \rightarrow (-y, -t) \quad (15)$$

$$(y, z, t) \rightarrow (-y, -z, -t) \quad (16)$$

$$(z) \rightarrow (-z) \quad (17)$$

Note that while the symmetry expressed in Eq. (17) mirrors only the  $z$  component, Eqs. (15, 16) also include a time reversal. From Eqs. (15)-(17), we can conclude that if a trajectory satisfies one of the following conditions at two different times  $t_1 \neq t_2$

$$(y, \dot{x}, \dot{z}) = 0 \quad (18)$$

$$(y, z, \dot{x}) = 0 \quad (19)$$

the resulting orbit will be periodic [31], with period  $T = 2(t_2 - t_1)$ , assuming  $t_2 > t_1$ . The condition in Eq.(18) is used to find periodic orbits via differential correction.

## B. State transition matrix and stability

Let us take a general state vector  $\mathbf{X} = [x, y, z, \dot{x}, \dot{y}, \dot{z}]^T$  and define the system of ordinary differential equations in Eqs. (1)-(3) by  $F(\mathbf{X})$ , such that  $\dot{\mathbf{X}} = F(\mathbf{X})$ . If we consider the previously mentioned equilibrium points, which are defined by  $F(\mathbf{X}_{eq}) = 0$  [36], we can take  $\mathbf{w}$  such that  $\mathbf{X}^* = \mathbf{X}_{eq} + \mathbf{w}$  is in the neighborhood of  $\mathbf{X}_{eq}$ . We can then linearize

$$\dot{\mathbf{X}}^* = \dot{\mathbf{X}}_{eq} + \dot{\mathbf{w}} = F(\mathbf{X}_{eq} + \mathbf{w}) \approx F(\mathbf{X}_{eq}) + \left. \frac{\partial F(\mathbf{X})}{\partial \mathbf{X}} \right|_{eq} \mathbf{w} + O(\mathbf{X}_{eq}^2) \quad (20)$$

where, if we neglect the higher order terms  $O(\mathbf{X}_{eq}^2)$ , we obtain

$$\dot{\mathbf{w}} = \left. \frac{\partial F(\mathbf{X})}{\partial \mathbf{X}} \right|_{eq} \mathbf{w} = J\mathbf{w} \quad (21)$$

The solution to the variational equation in Eq. (21) can be obtained by the State Transition Matrix (STM) [48],  $\Phi(t, t_0)$ , where  $J$  is the Jacobian of the system at time  $t$  and the initial condition  $\Phi(t_0, t_0) = I$  is the identity matrix

$$\dot{\Phi}(t, t_0) = J \Phi(t, t_0) \quad (22)$$

The STM is thus defined as [49]

$$\Phi(t, t_0) = \frac{\partial \mathbf{X}(t)}{\partial \mathbf{X}(t_0)} \quad (23)$$

and can be integrated alongside the equations of motion.

The study of the STM has many applications. For a periodic orbit, we can compute its eigenvalues after one period,  $T$ , to analyze its stability. The STM after one period is commonly known as the Monodromy matrix,  $\Phi_M = \Phi(T, t_0)$  [50]. The eigenvalues of the Monodromy matrix occur in three reciprocal pairs [51], as  $\{\lambda_1, \frac{1}{\lambda_1}, \lambda_2, \frac{1}{\lambda_2}, 1, 1\}$ . The two unit pairs are a characteristic of the energy integral of the system and are always situated on the unit circle [29, 52]. A periodic orbit will be stable if all its eigenvalues are situated on the unit circle. Focusing on  $\lambda_1, \lambda_2$ , we introduce the following stability indices  $k_1, k_2$  [29, 52]

$$k_i = \lambda_i + \frac{1}{\lambda_i} \quad (24)$$

where an orbit will be stable if  $|k_i| < 2$  and  $k_i$  is real for  $i = 1, 2$ .

### C. Differential correction

In order to find periodic orbits, a single-shooting differential corrector method is implemented [50]. Differential correction is a targeting method that uses the STM to iteratively improve a set of initial conditions. From an initial condition  $\mathbf{X}_0 = [x_0, 0, z_0, 0, \dot{y}_0, 0]^T$ , which satisfies the first part of the periodic orbit condition in Eq. (18) (the condition must be met at two different times), we integrate the state vector and STM forward in time until the first  $xz$ -plane crossing, i.e.,  $y = 0$ . When searching for a simply-periodic orbit, we can assume as a first approximation that this corresponds to the half-period mark  $\tau = T/2$ , and  $\mathbf{X}_\tau = [x_\tau, 0, z_\tau, \dot{x}_\tau, \dot{y}_\tau, \dot{z}_\tau]^T$ . From the periodic orbit condition of Eq. (18), we can write the error with respect to the state vector of the actual periodic orbit at the half-period mark ( $t_2$ ) as  $\Delta\mathbf{X}_\tau = [\Delta x_\tau, 0, \Delta z_\tau, -\dot{x}_\tau, \Delta\dot{y}_\tau, -\dot{z}_\tau]^T$ . Then, linearizing and neglecting the higher order terms, we can write

$$\Delta\mathbf{X}_\tau \approx \Phi(\tau, t_0)\Delta\mathbf{X}_0 + F(\mathbf{X})|_{t=\tau} \Delta\tau \quad (25)$$

where  $\Delta\mathbf{X}_0 = [\delta x_0, 0, \delta z_0, 0, \delta\dot{y}_0, 0]^T$  is the correction to be implemented to the initial condition, and  $\Delta\tau$  is the deviation from  $T/2$ . Note that  $\Delta\tau$  can be obtained from the second row of the vector notation in Eq. (25) and is equal to

$$\Delta\tau = \frac{-\phi_{21}\delta x_0 - \phi_{23}\delta z_0 - \phi_{25}\delta\dot{y}_0}{\dot{y}_\tau} \quad (26)$$

where  $\phi_{ij}$  correspond to the  $i, j$  elements of the STM and  $\delta x_0, \delta y_0, \delta z_0$  represent the correction to the initial conditions.

Combining Eqs. (25) and (26) we can then write

$$-\dot{x}_\tau = \left(\phi_{41} - \frac{\ddot{x}_\tau}{\dot{y}_\tau}\phi_{21}\right)\delta x_0 + \left(\phi_{43} - \frac{\ddot{x}_\tau}{\dot{y}_\tau}\phi_{23}\right)\delta z_0 + \left(\phi_{45} - \frac{\ddot{x}_\tau}{\dot{y}_\tau}\phi_{25}\right)\delta\dot{y}_0 \quad (27)$$

$$-\dot{z}_\tau = \left(\phi_{61} - \frac{\ddot{z}_\tau}{\dot{y}_\tau}\phi_{21}\right)\delta x_0 + \left(\phi_{63} - \frac{\ddot{z}_\tau}{\dot{y}_\tau}\phi_{23}\right)\delta z_0 + \left(\phi_{65} - \frac{\ddot{z}_\tau}{\dot{y}_\tau}\phi_{25}\right)\delta\dot{y}_0 \quad (28)$$

where we have three unknown variables ( $\delta x_0, \delta z_0, \delta\dot{y}_0$ ) and two equations. By setting the value of one of these variables to zero (in this paper we choose to set  $\delta x_0 = 0$ ) we can easily obtain the necessary correction to the other two initial

coordinates. This operation is repeated until the norm of the correction vector  $\Delta X_0$  is below a specified tolerance, chosen to be  $10^{-9}$ . Once a periodic orbit is found, a family continuation algorithm is adopted, which makes use of a modified version of the pseudo-arclength continuation method [53–55].

## D. Periodic orbits of the AHP and perturbed AHP models

### 1. AHP model

In the traditional Hill Problem studied by Hénon in [17], five families of periodic orbits are identified:  $a$ ,  $g$ ,  $g'$ ,  $f$ , and  $c$ . The  $a$  and  $c$  families correspond to planar Lyapunov orbits about the  $L_2$  and  $L_1$  points, respectively; the  $g$  and  $f$  families correspond to Distant Prograde Orbits (DPOs) and Distant Retrograde Orbits (DROs), respectively [56]; and family  $g'$  corresponds to a bifurcation from the  $g$  family. In [32], the effect of SRP on these families is presented, showing that the  $g$  family crosses the origin of the reference frame for increasing values of SRP acceleration, tending towards degenerate near-linear orbits along the  $x$ -axis; family  $c$  loses its significance to our problem as the  $L_1$  point quickly shifts towards the Sun (see Figure 1a); family  $f$  experiences a similar behavior to family  $g$ , albeit extending towards the  $L_1$  point; and families  $a$  and  $g'$  approach the asteroid with the  $L_2$  point (see Figures 4, 5). Family  $a$ , as well as other libration point orbits, are also studied in the AHP model for large values of SRP acceleration in the proximity of asteroids in [23, 24]. For the reasons stated above, we focus on the  $a$  and  $g'$  families.

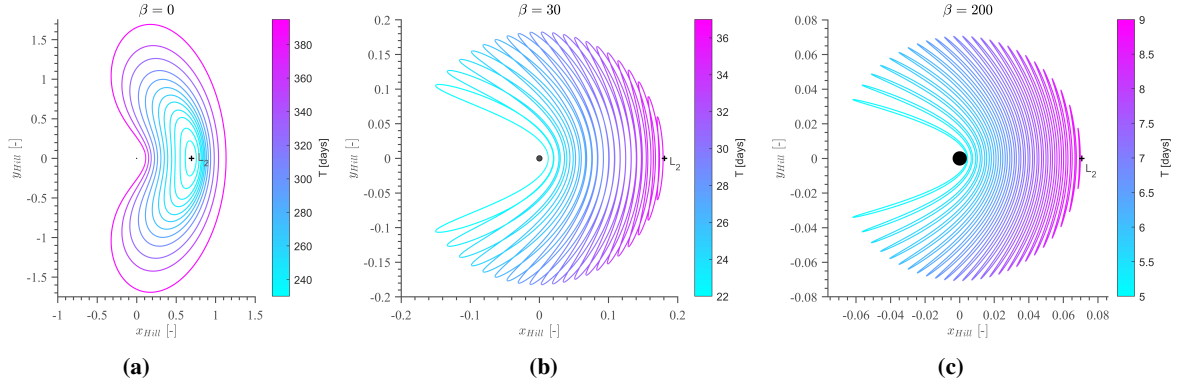


**Fig. 4 Family  $a$  of planar Lyapunov orbits in the AHP model for different values of SRP acceleration.**

While doubly-periodic family  $g'$  is unstable in the Hill Problem [17], the addition of the SRP acceleration stabilizes the family [32]. In fact, for the values of  $\beta$  considered in this work, all orbits in family  $g'$  are stable in the AHP model. Family  $a$ , however, is unstable in both the traditional Hill Problem and the AHP, for all values of SRP accelerations considered.

The third and final family of periodic orbits analyzed in this work is the family of southern halo orbits, which are commonly known as terminator orbits in the AHP [14, 25, 30] due to their existence close to the Sun-terminator plane, i.e., the plane perpendicular to the Sun-asteroid line.

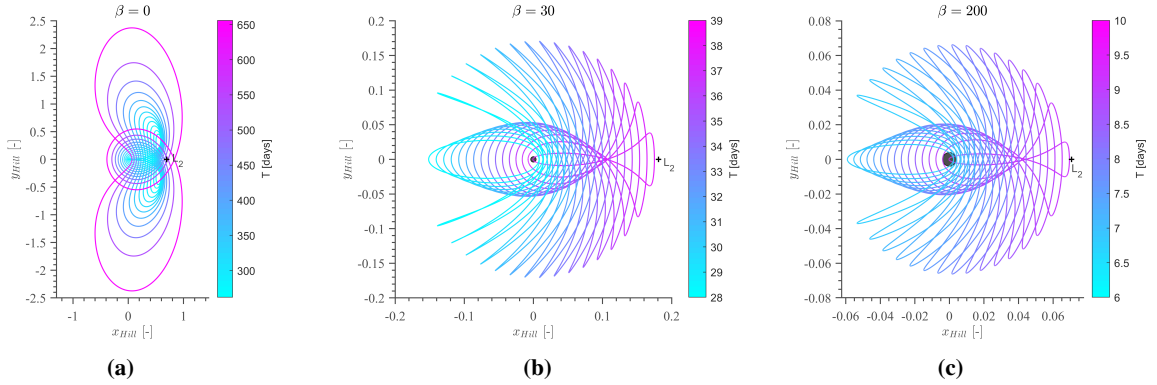


**Fig. 5 Family  $g'$  in the AHP model for different values of SRP acceleration.**

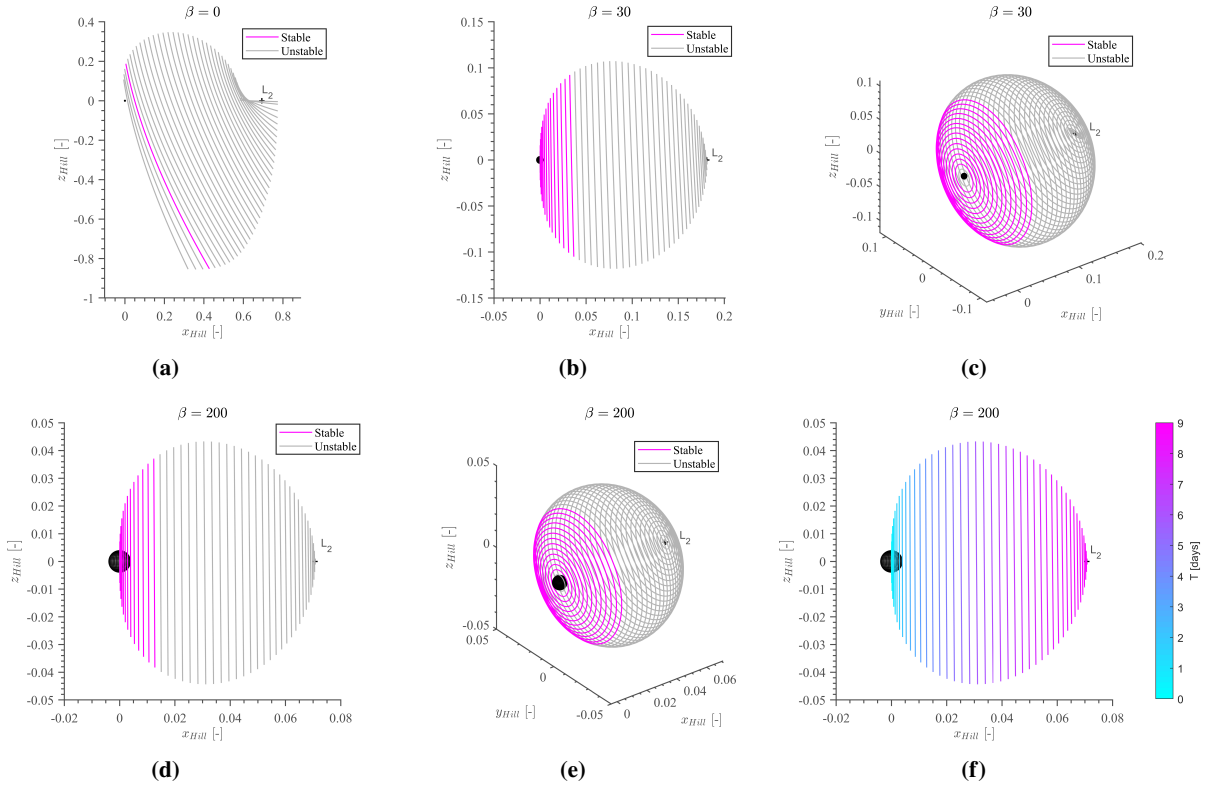


**Fig. 6 Family of terminator orbits for different values of SRP acceleration.**

The choice for studying the planar  $a$  and  $g'$  families of orbits arises from the natural evolution of the planar families with the inclusion of the SRP acceleration, while some of the other families disappear with this inclusion. In addition, both the Hayabusa2 spacecraft and the planned impact location are placed close to the ecliptic plane. Furthermore, the choice for studying terminator/halo orbits for the three-dimensional analysis arises from their previously studied characteristics, which hint at the possibility of presenting a potential hazard to the mission: terminator orbits have been noted to be robust to very large values of SRP acceleration and uncertainties in the gravitational model

[24, 25, 27, 30, 31, 42, 57, 58]. Figure 6 shows the family of terminator orbits, from which is clear that the family approaches the Sun-terminator plane as the SRP acceleration increases and the  $L_2$  approaches the asteroid. Nonetheless, the family doesn't show significant changes to its geometry, merely decreasing in size with the increase in  $\beta$ . A section of the terminator orbit families is always stable; in fact, this region is actually larger when considering SRP, as shown in Figure 6.

A final reason for studying both the terminator orbits and planar Lyapunov orbits (family  $a$ ) is that they originate from the  $L_2$  equilibrium point, which acts as a gateway for re-impacting, orbiting, and escaping trajectories in the AHP. The analysis of the collinear equilibrium point orbits can therefore provide insight into the possibility of escape versus re-impact of the ejecta particles. With this in mind, we choose to focus on these three families of periodic orbits, represented by their family curve parameters (initial  $x$  coordinate and Jacobi constant) in Figure 7.

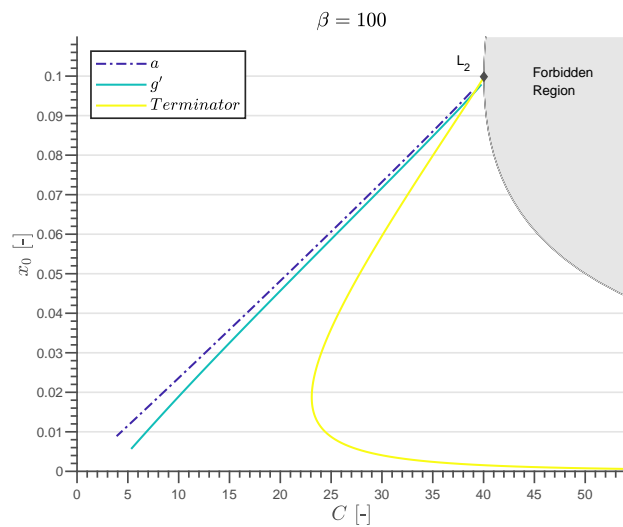


**Fig. 7** Family curves of families  $a$ ,  $g'$ , and terminator orbits in the AHP model for  $\beta = 100$ .

## 2. Eclipse model

Terminator orbits are largely unaffected by the eclipses, except close to the bifurcation with family  $a$  near the  $L_2$  point, where they reside in the eclipse region. For simplicity we neglect these few orbits of the terminator family. On the contrary, families  $a$  and  $g'$  always cross the eclipse region, which implies that their periodic solutions in the eclipse model are required for their analysis.

The inclusion of eclipse disrupts the time-invariant nature of the system, forcing the energy integral portrayed in Eq.(5) to vary as a particle enters or exist the eclipse region. Although the system does not include a time-dependent term, the inclusion of eclipses creates an implicit time dependence, causing the SRP acceleration and in turn the energy integral to vary. However, for an orbit to be periodic, this variation must also be periodic, or else the standard condition

of periodicity  $X(t) = X(t + T)$  [36] would be lost. Moreover, periodic solutions will still exist in the system when including eclipses, as the symmetry conditions in Eqs.(15)-(17) are still maintained.

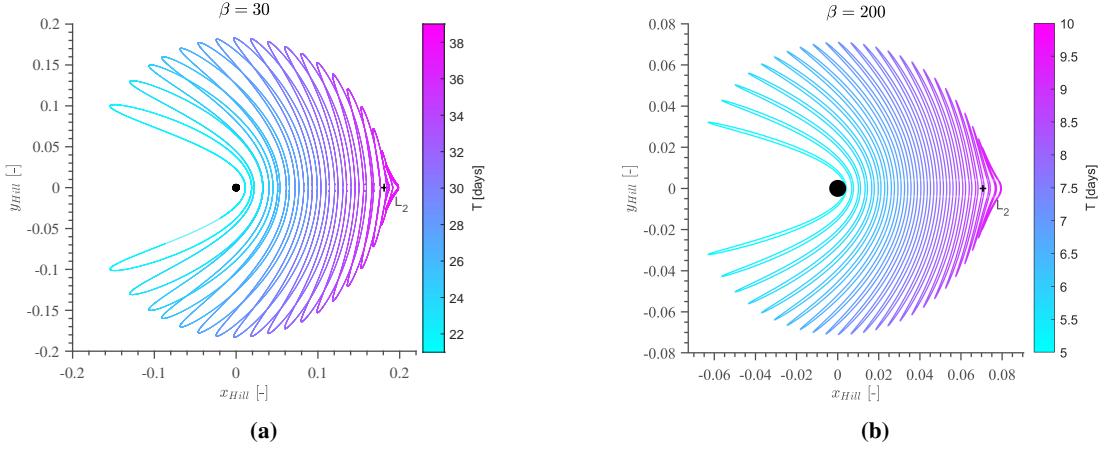


**Fig. 8** Family  $a$  in the AHP + eclipse model for different values of SRP acceleration.

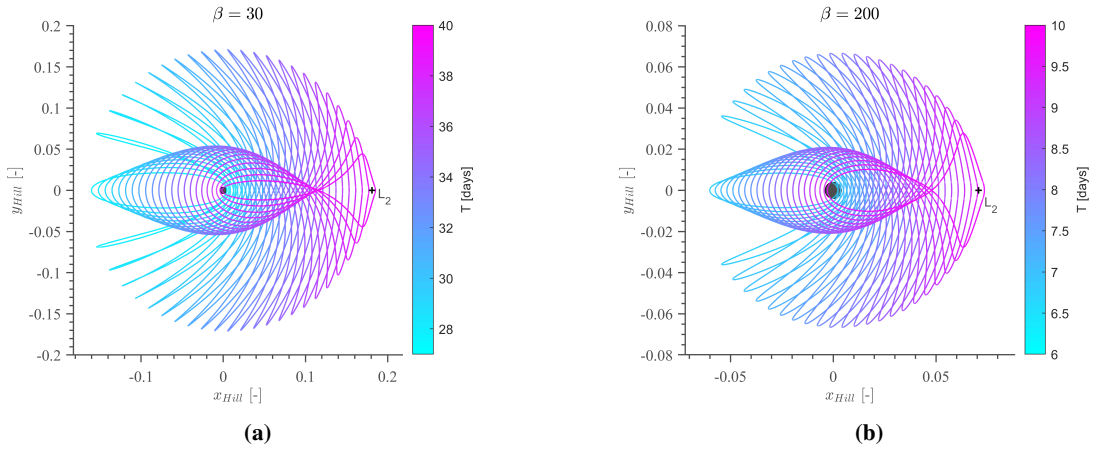


**Fig. 9** Family  $a$  in the AHP + eclipse model for different values of SRP acceleration.

From Figures 8 and 9 we can see how the geometry of families  $a$  and  $g'$  changes in the AHP + eclipse model. Specifically, we can see that the families continue past the  $L_2$  equilibrium point for the different  $\beta$ -values considered. Given there is no SRP acceleration in the eclipse region, the equilibrium point will actually take its position for  $\beta = 0$ . This allows the orbits in the AHP + eclipse model to extend past the  $L_2$  point of the AHP model. The inclusion of eclipses also has implications on the regions of accessible motion defined by the ZVCs (see Figure 1). Due to the periodic variation of the Jacobi constant, these regions will not be constant along an orbit that passes through the eclipse region, but rather vary periodically, depending on the position of the particle along the orbit.

As stated before, the existence of the unit eigenvalue pair of the STM is attributed to the existence of an energy integral in the system. Because the Jacobi constant is no longer constant in the AHP + eclipse model, one might assume

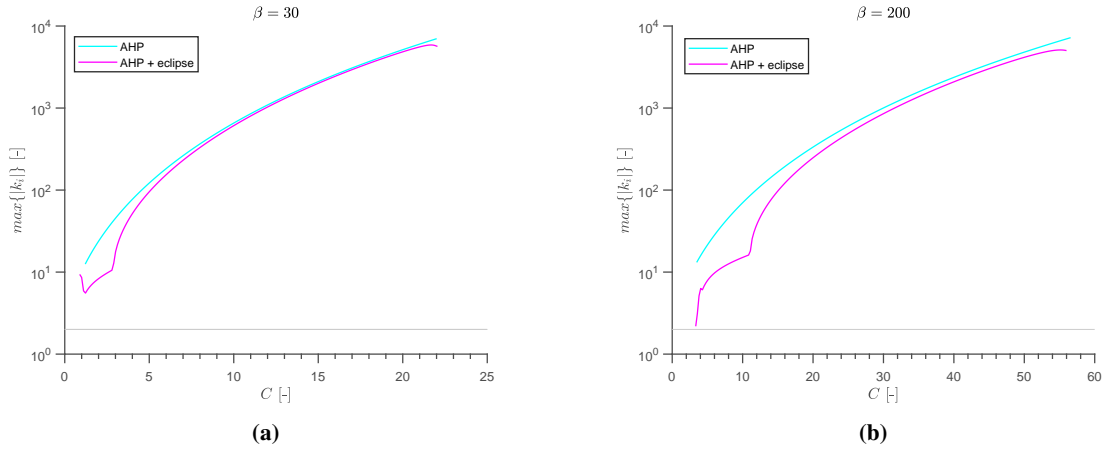


**Fig. 10** Stability of family  $a$  in the AHP and AHP + eclipse models for different values of SRP acceleration.

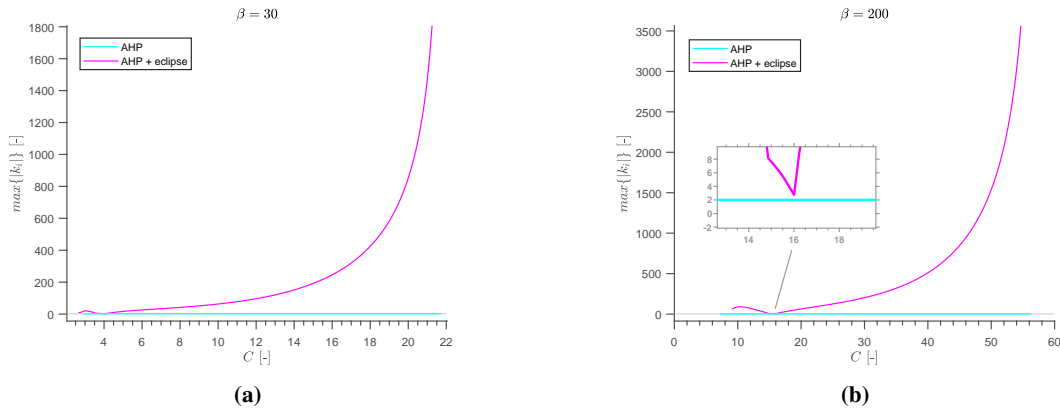


**Fig. 11** Stability of family  $g'$  in the AHP and AHP + eclipse models for different values of SRP acceleration.

that the stability of a periodic orbit can no longer be correctly defined by analyzing its Monodromy matrix. While it is true that the unit eigenvalue pair will vary slightly in the AHP + eclipse model, the symplectic nature of the STM is maintained, a fact that can be verified by analyzing the determinant of  $\Phi$ , which is found to remain within  $10^{-9}$  of unity. The variation to the unit pair simply reflects the disruption to the energy integral of the system. However, because the STM is integrated using the Jacobian of the equations of motion, which does not depend on  $\beta$ , we can still analyze the orbit's stability by studying the eigenvalues of the Monodromy matrix.

Figures 10 and 11 show the effect of eclipses on the stability of the  $a$  and  $g'$  families. We see that the eclipses not only affect the geometry of the orbits and the regions of accessible motion of the particles but also the stability of the periodic orbits. Family  $g'$  becomes unstable for all values of  $\beta$ , while family  $a$  becomes slightly more stable with increasing values of  $\beta$ . For the general case this change in stability will only occur when the SRP plays a significant role in the dynamics, which is the case when studying the dynamics about small bodies (see Figure 3), even for spacecrafts [42]. Note that in Figures 10 and 11, and whenever referring to the Jacobi constant in the AHP + eclipse model, we take

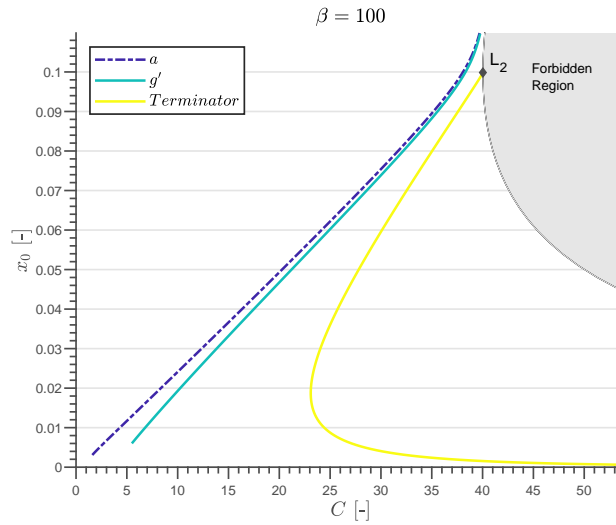


**Fig. 12 Family curves in the AHP + eclipse model for families  $a$ ,  $g'$ , and terminator orbits, for  $\beta = 100$**

the value of the nominal Jacobi constant, i.e., ignoring the eclipse. Although the variation of the Jacobi between the eclipse and non-eclipse regions can be significant (in the orders of magnitude of the nominal Jacobi constant), a particle only spends a very small part of the orbit in eclipse (less than 2% of the period).

Figure 12 shows the family curves of the  $a$ ,  $g'$ , and terminator families in the AHP + eclipse model. Comparing this figure with Figure 7, we see how the  $a$  and  $g'$  families extend past the  $L_2$  point due to the inclusion of eclipses.

### 3. Gravity perturbations model

Because the perturbation posed by the  $J_2$  and  $J_4$  terms is very small when compared to the other perturbations, the shape of the orbits does not change significantly when we include said gravity perturbations in the model. From Eq.(11), we see that the gravity potential will decrease by powers of  $r^2$  and  $r^4$ , which means that the effect of these perturbations will only be significant in close-proximity to the asteroid. This is clear in Figures 13 and 14, that show the family curves of the  $a$ ,  $g'$ , and terminator families in the different dynamical models. The family curve in the AHP +  $J_2$ ,  $J_4$  + eclipse model is slightly offset from the curves in the AHP + eclipse and AHP models when in close-proximity to the asteroid. However, as the distance to the asteroid increases, the family curves of the AHP + eclipse and AHP +  $J_2$ ,  $J_4$  + eclipse models overlap. Despite the small changes to the orbits, note that the inclusion of the  $J_2$ ,  $J_4$  will still affect the trajectories in close-proximity to the asteroid. Note that only one value of SRP acceleration is presented for each of the  $g'$  and terminator family, since they do not exhibit significant changes for different values of SRP acceleration. Finally, the change in stability to the  $a$ ,  $g'$ , and terminator families is almost negligible when adding the gravity perturbations.

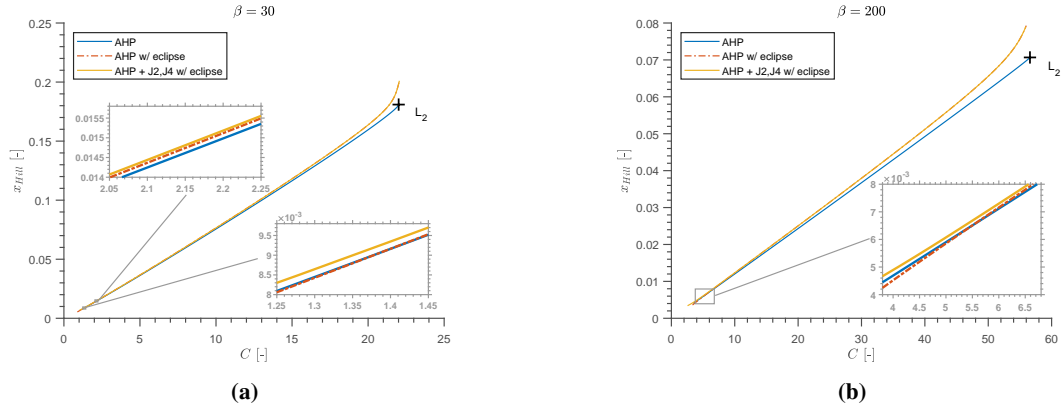


**Fig. 13** Family curve for family *a* in the different dynamical models.

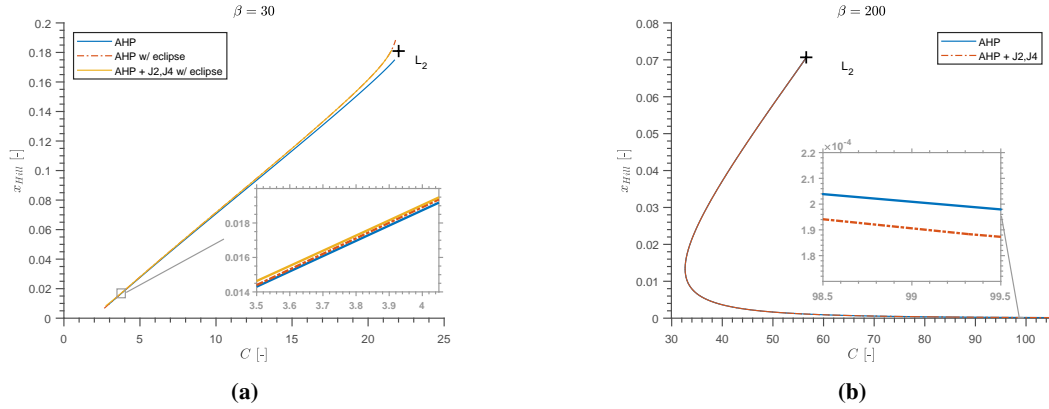


**Fig. 14** Family curves in the different dynamical models for families: (a) *g'*; (b) terminator.

## IV. Particle Ejection Dynamics

In this section we discuss the considerations surrounding the ejection of particles from the asteroid, how we can study the particles that are captured in periodic orbits, and the planned escape trajectory of the Hayabusa2 spacecraft.

### A. Ejection angle

Previous work has considered the problem of asteroid ejecta as a product of a ballistic impact [59, 60]. While more research regarding the ejection angle and velocity distribution for different impact angles, velocities, and surface materials is surely necessary, it is common to assume an ejection angle close to  $45^\circ$  with the surface normal [59, 61–63]. This assumption is based on existing literature and experiments, which show that for impact angles smaller than  $60^\circ$  with respect to the surface normal, the ejection angles tend to exist between  $35^\circ$  and  $50^\circ$  from the surface normal for non-high-velocity particles [64, 65]. Only for very oblique angles have the non-high-velocity particles shown to deviate from this ejection direction and have craters shown more evident asymmetry [66, 67]. However, despite a possible error in impact angle for the SCI, this angle is not expected to depart significantly from its nominal vertical impact [10].

The impact error relative to three-standard deviations (99.7%) corresponds to an error of approximately  $26^\circ$  from the surface normal, far smaller than the aforementioned  $60^\circ$ . Note that when considering the high- or hyper-velocity ejecta particles, this ejection direction may not be observed [68], but given that said particles have far larger velocities than the escape velocity of the asteroid, the aforementioned assumption is still valid for our study. For these reasons, we assume the regolith particles to be ejected only within the range  $\sigma \in [35^\circ, 50^\circ]$ , where  $\sigma$  is the ejection angle with respect to the surface normal. Finally, it should be mentioned that the highest velocity ejecta particles have been shown to be the smallest and also the ones to escape first [68], which backs the choice of  $\beta$  values to not include sub-millimeter sized particles.

## B. Invariant Manifolds and Particle Ejection

We aim to analyze how ejecta might be temporarily captured in periodic orbits about the asteroid. In reality, a particle will not exactly follow the trajectory towards the periodic orbit nor the periodic orbit itself, due to perturbations that we are neglecting in our analysis. Nonetheless, we assume that in reality, it will follow a trajectory close enough to that predicted in our model so we can correctly portray and identify possible hazards to the Hayabusa2 spacecraft. Furthermore, even if an orbit is unstable in the mathematical sense (as detailed in Section III.B), a particle can still remain in the orbit and/or the trajectory leading to it for a long enough time-span to affect the safety of the mission [19].

In order to identify a link between a particle being ejected from the asteroid surface and the periodic orbits, we make use of invariant manifold theory. The invariant manifolds of an unstable orbit define all the trajectories a particle can take, at any point in its orbit, when perturbed in the direction of the orbit's local eigenvectors. All unstable periodic orbits have at least one stable and at least one unstable eigenvalue and respective eigenvectors, which indicate, respectively, all the trajectories that asymptotically lead to or from the orbit [50]. That is, by integrating forward in time a point in an unstable orbit in the direction of its unstable eigenvector, we obtain the local unstable manifold of the orbit at that point. The same occurs when integrating backwards in time in the direction of the local stable eigenvector. Theoretically, these trajectories can occur naturally when the perturbation applied tends to zero. Invariant-manifold-enabled trajectories have therefore been suggested before for virtually fuel-free transfers in trajectory design [69–73].

The initial conditions,  $\mathbf{X}_i^S, \mathbf{X}_i^U$ , of the stable and unstable manifolds at a point  $i$  along an unstable orbit are defined as [74]:

$$\mathbf{X}_i^S = \mathbf{X}_i \pm \epsilon \frac{\mathbf{v}_i^S}{|\mathbf{v}_i^S|} \quad (29)$$

$$\mathbf{X}_i^U = \mathbf{X}_i \pm \epsilon \frac{\mathbf{v}_i^U}{|\mathbf{v}_i^U|} \quad (30)$$

where  $\mathbf{v}_i^S, \mathbf{v}_i^U$  are the local stable and unstable eigenvectors at that point, respectively, and  $\epsilon$  is a small perturbation. The

value of  $\epsilon$  must be small enough so that the assumption on linear dynamics still holds and the motion is considered as asymptotically moving to or from the orbit, but not so small that the integration time is too long because the particle does not depart from the orbit. We chose the dimensionless perturbation value of  $\epsilon = 10^{-6}$ , as suggested in [74, 75], which translates to a position error of 0.1 m. The choice in sign of Eqs. (29), (30) defines the interior and exterior components of the manifolds. Figure 15 shows the stable and unstable manifolds of a planar Lyapunov orbit (family  $a$ ) for  $\beta = 0$ , while Figure 16 shows the stable manifolds for the same family but for different values of the SRP acceleration in the AHP model. Both figures present also the regions of forbidden motion defined by the ZVCs. Note how the shape of manifolds approach the shape of ZVCs for increasing values of  $\beta$ .

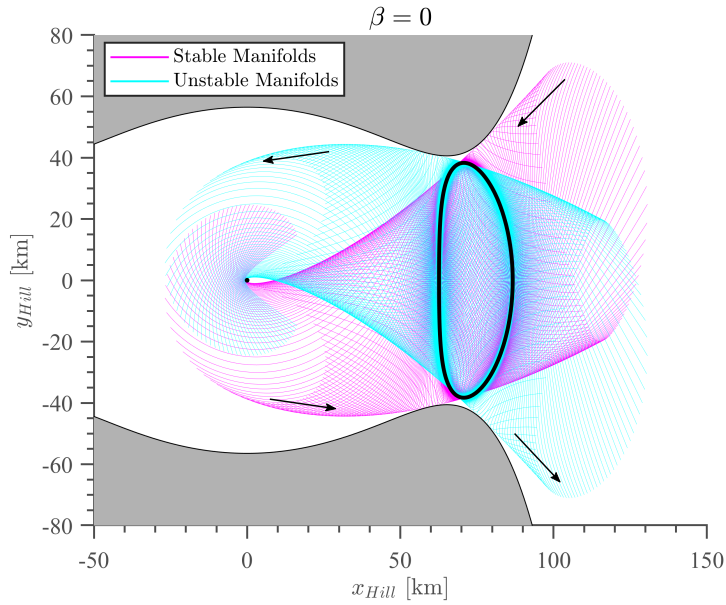


**Fig. 15** Stable and unstable invariant manifolds of an orbit from family  $a$  for  $\beta = 0$ . The region of forbidden motion defined by the ZVC is shown in gray.

The eigenvectors in Eqs.(29)-(30) can be computed from the STM [74]

$$\mathbf{v}_i^{S,U} = \Phi(t_i, t_0) \mathbf{v}^{S,U} \quad (31)$$

where  $\mathbf{v}^{S,U}$  are the stable and unstable eigenvectors of the Monodromy matrix. Considering we want to study the motion of particles arriving at the orbits as opposed to those departing from them, from here on we only focus on calculating the stable manifolds of periodic orbits.

Instead of computing the invariant manifolds of periodic orbits, we can also compute the invariant manifolds of the equilibrium points, as mapping the structure of their manifolds may provide significant insight into the fundamental

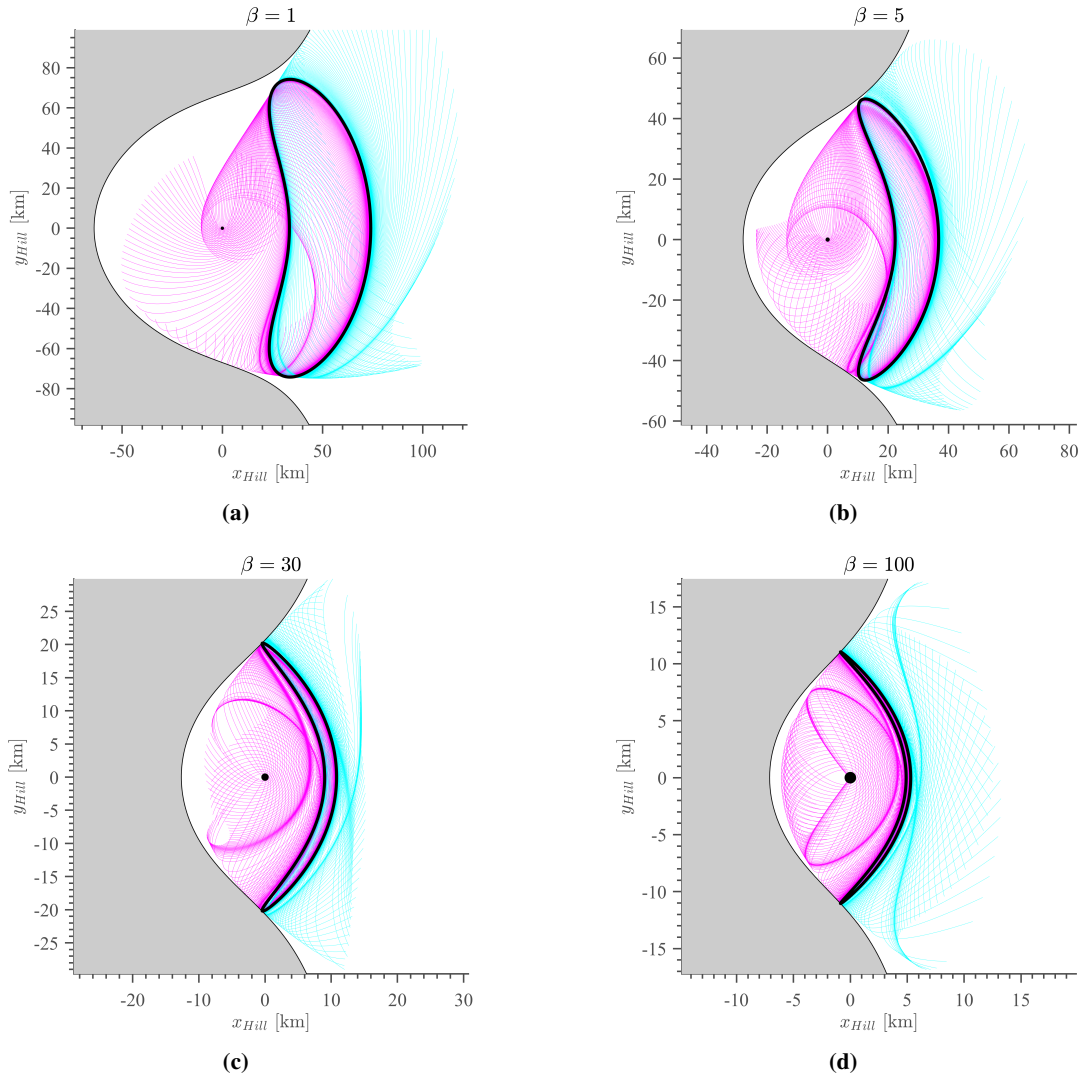


**Fig. 16** Stable manifolds for orbits of family  $a$  in the AHP model for different values of the SRP acceleration. Interior manifolds are shown in pink and exterior manifolds in blue. The regions of forbidden motion defined by the ZVCs are shown in gray.

motion of the particles. For a state  $X_{eq}$  defined by the  $L_2$  equilibrium point, we calculate the Jacobian  $J$  at that point and compute its eigenvectors for the stable and unstable eigenvalues, i.e., the smallest and largest eigenvalues, respectively. The interior stable manifolds of the  $L_2$  point in the AHP model for different values of the SRP acceleration are shown in Figure 17. Note that for larger values of  $\beta$ , the stable manifolds of  $L_2$  intersect with the asteroid surface.

Comparing Figures 16 and 17, we can see how the general direction and shape of the manifolds of family  $a$  follows the structure of the manifolds of  $L_2$ . As  $\beta$  increases, the manifolds tend to travel along the  $x$ -axis, intersect with the asteroid, and become more symmetric with respect to the  $x$ -axis. Moreover, as the nominal orbits approach the  $L_2$  point, their stable manifolds mimic those from the equilibrium point. This is explained by the fact that family  $a$  (as well as the

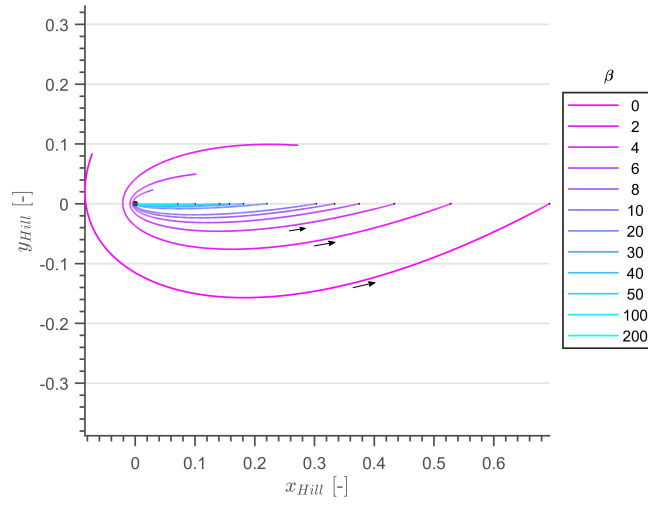


**Fig. 17** Interior stable manifolds of the  $L_2$  equilibrium point for different values of SRP acceleration.

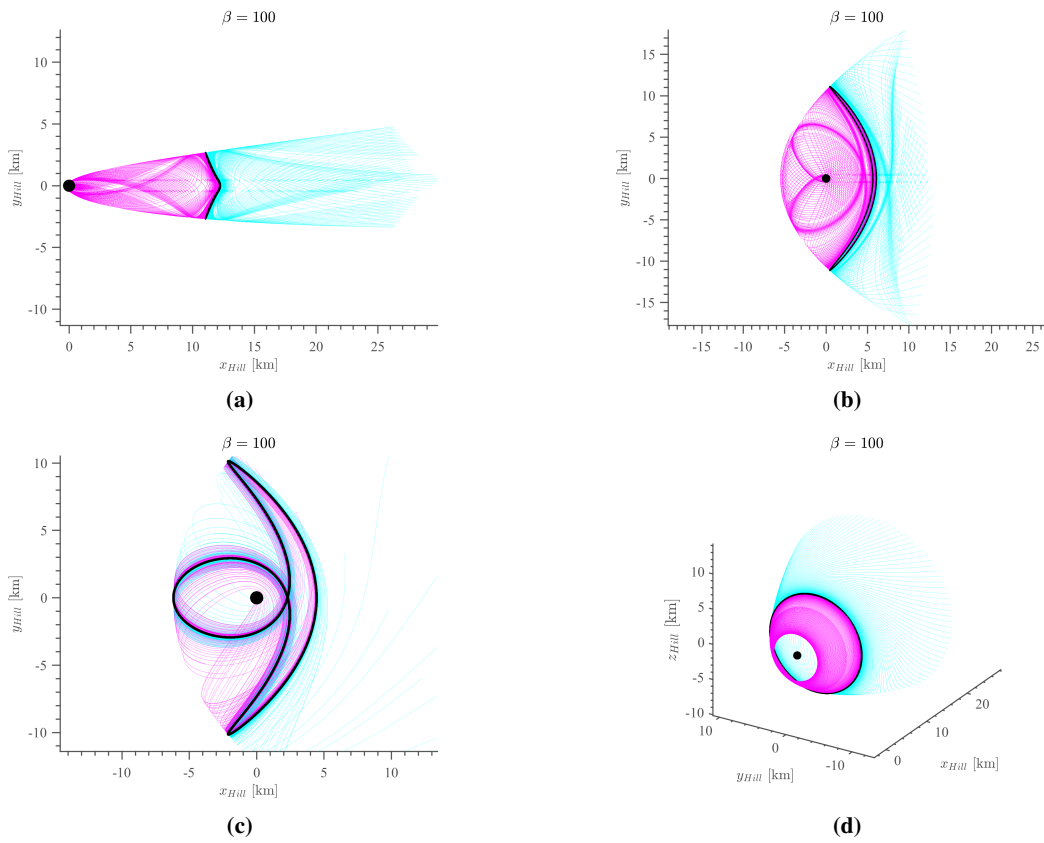


**Fig. 18** (a) and (b): Stable manifolds of orbit from family  $a$ . (c) Stable manifolds for orbit from family  $g'$ . (d) Stable manifolds for orbit from terminator families. All figures are obtained in the AHP +  $J_2, J_4$  + eclipse model with  $\beta = 100$ . Interior manifolds are shown in pink and exterior manifolds in blue.

family of terminator orbits), originate from  $L_2$ . It is also for this reason that we can clearly distinguish the interior and exterior manifolds, the interior extending towards the asteroid and the exterior away from it. For orbits that orbit the asteroid, as those from family  $g'$ , the interior and exterior manifolds do not follow such a distinct dynamic, resulting in trajectories from the exterior manifold that can intersect the asteroid. Figure 18 shows the stable manifolds of the  $a$ ,  $g'$ , and terminator families for different orbits in the full model, i.e., the AHP +  $J_2, J_4$  + eclipse model. Note that the stable manifolds of the terminator family also follow the shape of the stable manifolds of the  $L_2$  point, although for the specific case shown in Figure 18d they do not intersect the asteroid and instead remain in orbit about it.

### C. Trajectory simulation

To find the initial conditions and trajectories that cause the ejecta particles to be temporarily trapped in the considered periodic orbits, we divide each orbit in 250 equidistant nodes, perturb the state of each in the direction of its local stable eigenvector (as detailed in Eq. (29)), and integrate backwards in time. The integration is carried out until one of three stopping conditions is occurs: (1) escape from the system, estimated by the computation of the specific energy of the particle [13]; (2) impact with the asteroid; (3) total integration time reaches 150 days. Note we consider the "impact" radius to be slightly larger than the largest axis of the asteroid,  $a$ , thus avoiding entering the Brillouin sphere of the gravity's spherical harmonics (see [14]). The simulations are carried out in the full model, including the eclipses and gravity gravity perturbations. We consider SRP acceleration values of  $\beta = \{30, 40, 50, 75, 100, 125, 150, 175, 200\}$ ,

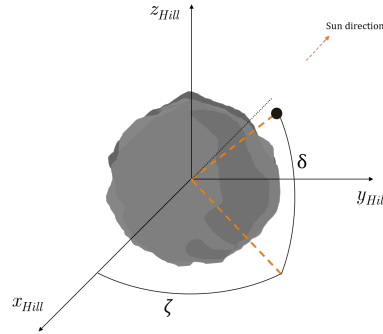


**Fig. 19 Spherical coordinates in the Hill frame.**

which correspond, respectively, to ejecta particle radii of  $R \approx \{5.2, 3.9, 3.1, 2.1, 1.6, 1.2, 1.0, 0.9, 0.8\}$  cm. For each value of  $\beta$ /radius and family of periodic orbits described, we select equidistant orbits along the family, selecting at least 200 orbits per family. By selecting a large number of equidistant orbits along each family we aim to sample the characteristics and structure of said family for each value of  $\beta$ , and thus obtain representative results for the dynamical environment about the asteroid.

When a manifold intersects the asteroid we store the values of its position and velocity, its nominal orbit, and the time it takes for the particle to arrive at the orbit from the asteroid surface. In order to facilitate the presentation of the

results shown in future sections, we establish the following spherical coordinates, defined in the Hill frame: the right ascension,  $\zeta$ , which is the angle measured in the  $xy$ -plane from the  $x$ -axis in a positive direction; and the declination,  $\delta$ , measured from  $xy$ -plane in the direction of the  $z$ -axis, as shown in Figure 19.

#### D. Hayabusa2 escape trajectory

The SCI is a kinetic impactor that will achieve an approximate velocity of 2 km/s upon impact, propelled by an explosive charge [10]. For this reason, after releasing the SCI, the Hayabusa2 spacecraft must move away from the SCI,

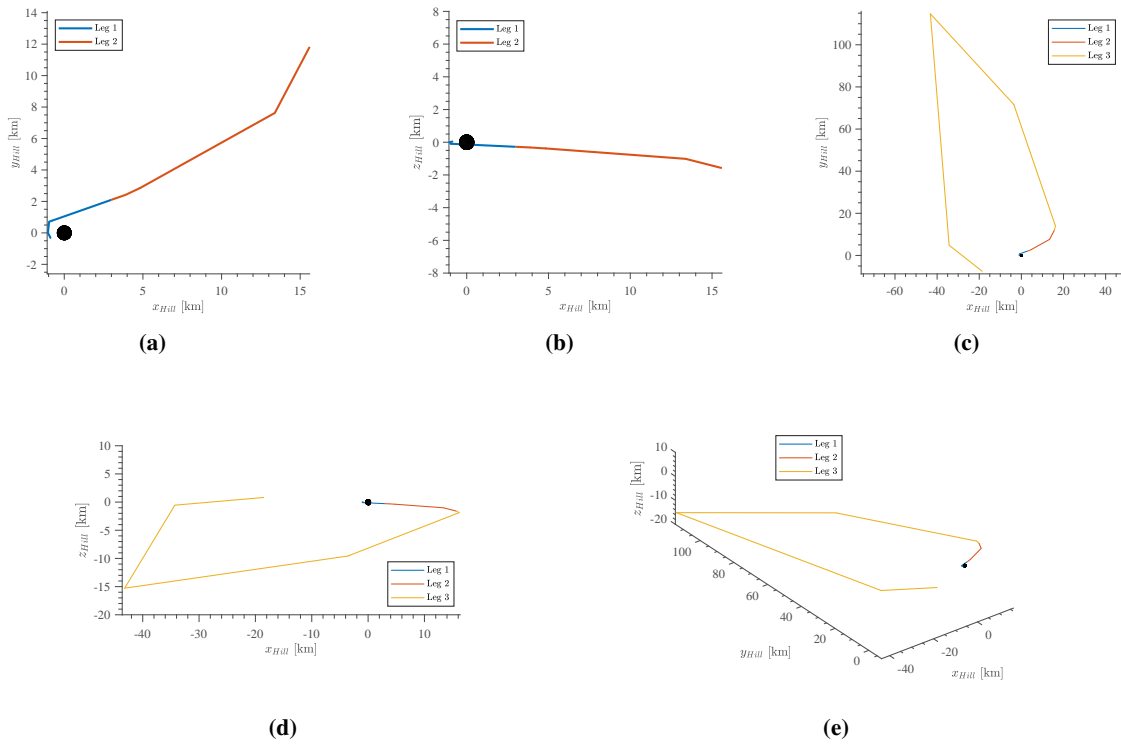


**Fig. 20** The three legs of Hayabusa2's escape trajectory during and following the SCI operation [10].

so that the debris from the charge detonation does not collide with the spacecraft. When released, the SCI's timer, which is set to 40 minutes, will allow for sufficient time for the spacecraft to complete the first leg of its escape trajectory, protecting itself from the explosion by hiding behind the asteroid. Figure 20 shows the three legs of the planned escape trajectory, which is expected to return the spacecraft to the asteroid approximately two weeks after impact [10]. The nominal impact location and respective error radius given by three standard deviations are shown in Figure 21, in the Hill frame. The impact location is slightly offset from the equator towards the northern hemisphere and from the Sun-asteroid line towards the negative  $y$ -axis. The three standard deviation error corresponds to an approximate position error of 200 m.

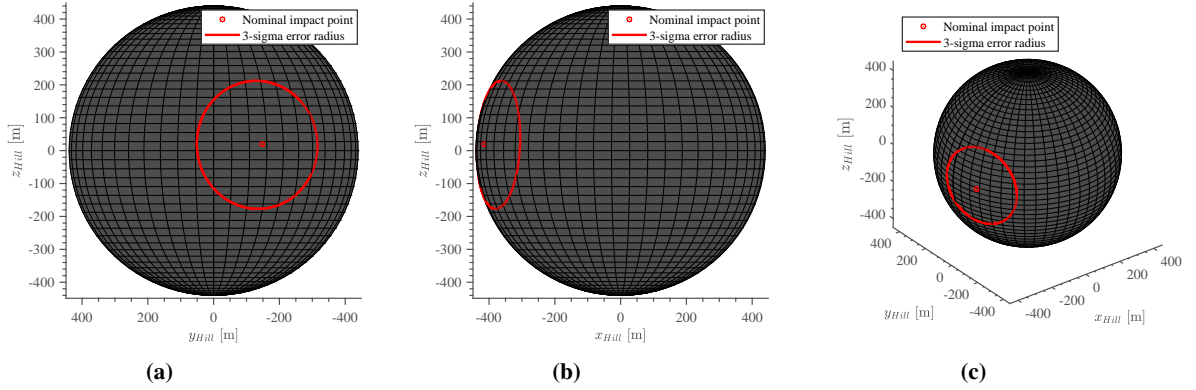


**Fig. 21** Nominal impact location and error radius given by three standard deviations.

## V. Results

This section presents the results obtained from the invariant manifolds analysis described in the previous sections. All results are obtained using the full model, which considers SRP, eclipses, and the gravity perturbations of the  $J_2$  and  $J_4$  terms. Since the stable manifolds are integrated backwards in time, the trajectories that intersect the asteroid surface are in practice ejection trajectories - with a specific ejection location, velocity, and angle - that lead to the periodic orbits. For that reason, we often use the term ejection conditions to refer to the conditions of the stable manifolds at the intersection with the asteroid surface.

### A. Family $a$

A distribution of the ejection velocities for the trajectories that lead to family  $a$  can be seen in Figure 22, where the Figure 22a shows the ejection velocities for any ejection angle and Figure 22b shows the ejection velocities for  $\sigma \in [35^\circ, 50^\circ]$ . Note that, as expected, all velocities are smaller than the local escape velocity of  $v_{esc} = \sqrt{2\mu/r}$  [13], which is marked in the figures with a dashed red line. The ejection velocities for the different particle radii/SRP acceleration approach a common maximum, close to 37.9 m/s, for which the periodic orbits approach the asteroid.

Note also that all trajectories that lead to periodic orbits of family  $a$  must possess an ejection velocity for which the ZVCs are open at the  $L_2$  point, as the orbits of family  $a$  exist about the equilibrium point. An example of this can be seen in Figure 23, where the ZVC is shown for the case of no eclipse.

Figures 24 and 25 show the distribution of the locations, along the asteroid's equator, where the stable manifolds of family  $a$  intersect the surface of the asteroid, i.e., the ejection locations. Figure 24a shows the distribution when all possible ejection angles are considered while Figures 24b and 25 show the distribution for  $\sigma \in [35^\circ, 50^\circ]$ . The length of the bars in Figure 25 are cumulative for all  $\beta$  values, as in Figure 24, where the bars are stacked vertically for the different values of  $\beta$  and the percentage shown on the vertical axis is calculated in the following way for each bin  $i$

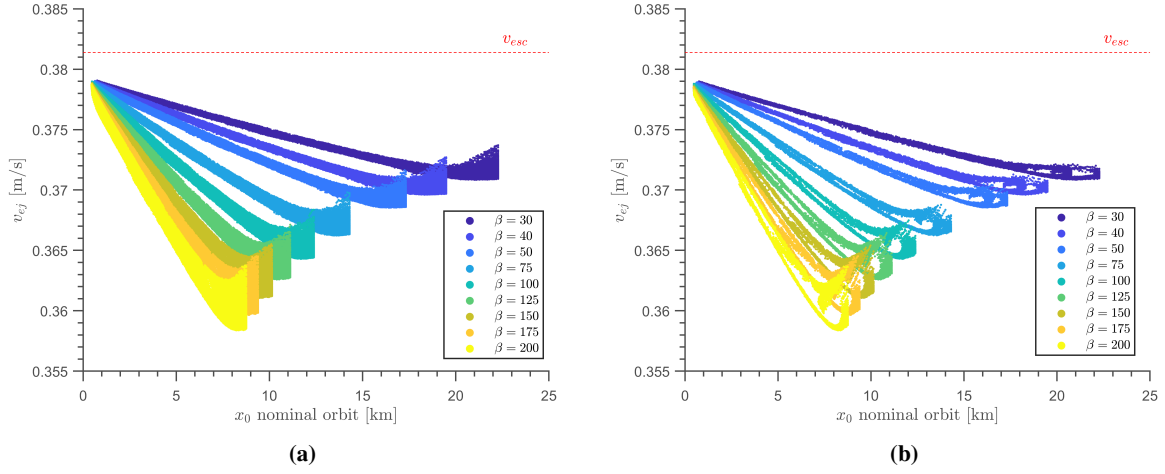


**Fig. 22** Ejection velocities for particles ejected along the stable manifolds of family *a* for different values of the SRP acceleration. (a) For any ejection angle; (b) for the expected ejection angles of  $\sigma \in [35^\circ, 50^\circ]$ .

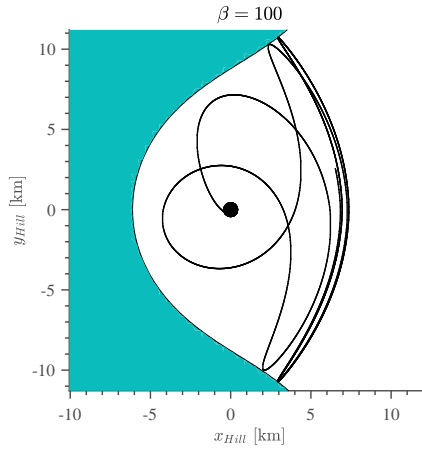


**Fig. 23** Example of stable manifold trajectory from asteroid surface to periodic orbit of family *a* with ZVC. Initial conditions:  $v_{ej} = 0.369$  m/s,  $\sigma = 47.76^\circ$ ,  $\zeta = 194.4^\circ$ .

$$D^i = N_{ej}^i / N_{total} \times 100 \quad (32)$$

where  $N_{total}$  is the total number of stable manifold trajectories that intersect the surface of the asteroid for either all ejection angles or  $\sigma \in [35^\circ, 50^\circ]$  and  $N_{ej}^i$  is the number of manifold trajectories that intersect the asteroid at the right ascension defined by the  $i^{th}$  bin at either any ejection angle (Figure 24a) or at  $\sigma \in [35^\circ, 50^\circ]$  (Figures 24b and 25). The sum of all bars equates to 100%, for all  $\beta$ -values and each of the sub-figures. The right ascension of the planned impact location is also indicated by a vertical gray line, although the nominal impact is not situated along the equator of the asteroid but slightly north from it (see Section IV.D). The error radius corresponding to three standard deviations shown

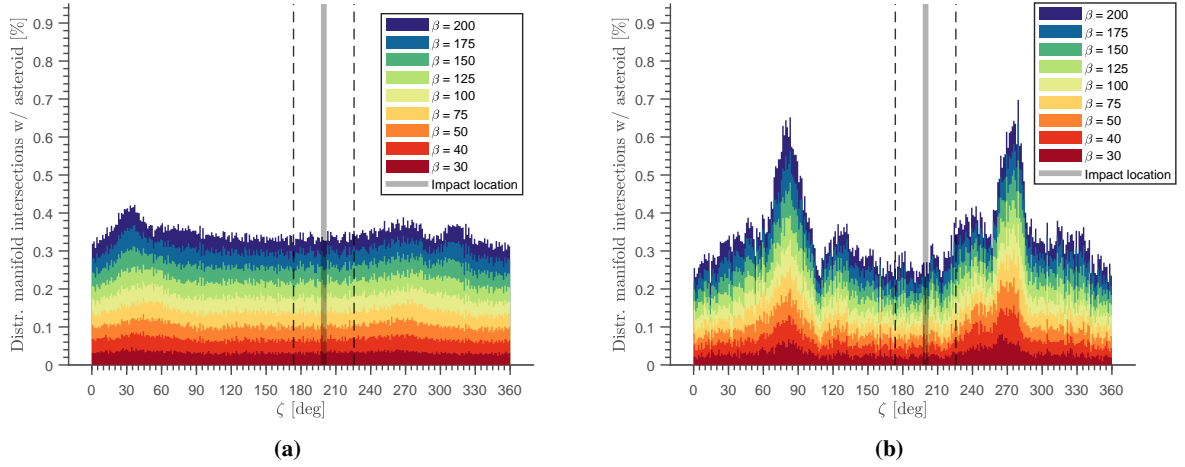


**Fig. 24** Distribution of the ejection locations for particles ejected along the stable manifolds of family  $a$  for different values of SRP acceleration. (a) For any ejection angle; (b) for ejection angles of  $\sigma \in [35^\circ, 50^\circ]$ .

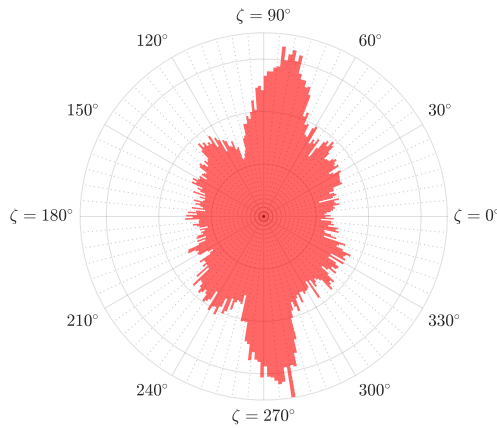


**Fig. 25** Cumulative distribution of the ejection locations in polar coordinates for particles ejected along the stable manifolds of family  $a$  for all values of SRP acceleration and ejection angles of  $\sigma \in [35^\circ, 50^\circ]$ .

in Figure 21 translates into an angle error of approximately  $\Delta\zeta = 26^\circ$  on either side of the nominal impact location and is represented by a black dotted line.

When considering all ejection angles, the distribution of stable manifold intersections around the asteroid's equator is distributed approximately equally along  $\zeta$ , with a small peak around  $\zeta = 35^\circ$  and a small "valley" or minimum around  $\zeta = 0^\circ$ . However, when only considering ejection angles of  $\sigma \in [35^\circ, 50^\circ]$ , Figure 24 shows how local maxima develop around right ascensions of  $\zeta \approx 80^\circ$  and  $\zeta \approx 270^\circ$ . The reason for this is the decrease in manifold trajectories from the other right ascensions, due to the geometry of the manifolds and the considered constraint on the ejection angles. A few examples of the stable manifold trajectories that lead to orbits from the asteroid to family  $a$ , can be seen in Figure 26, where the trajectories with ejection angles between  $\sigma \in [35^\circ, 50^\circ]$  are shown in orange, and the others in gray. The

manifold trajectories do indeed reach all right ascensions, but not always with an ejection angle between  $\sigma \in [35^\circ, 50^\circ]$ . Given that the locations  $\zeta \approx 80^\circ$  and  $\zeta \approx 270^\circ$ , i.e., close to the y-axis, present more trajectories with an ejection angle between these limits, we see a higher relative concentration of ejection locations at these right ascensions.

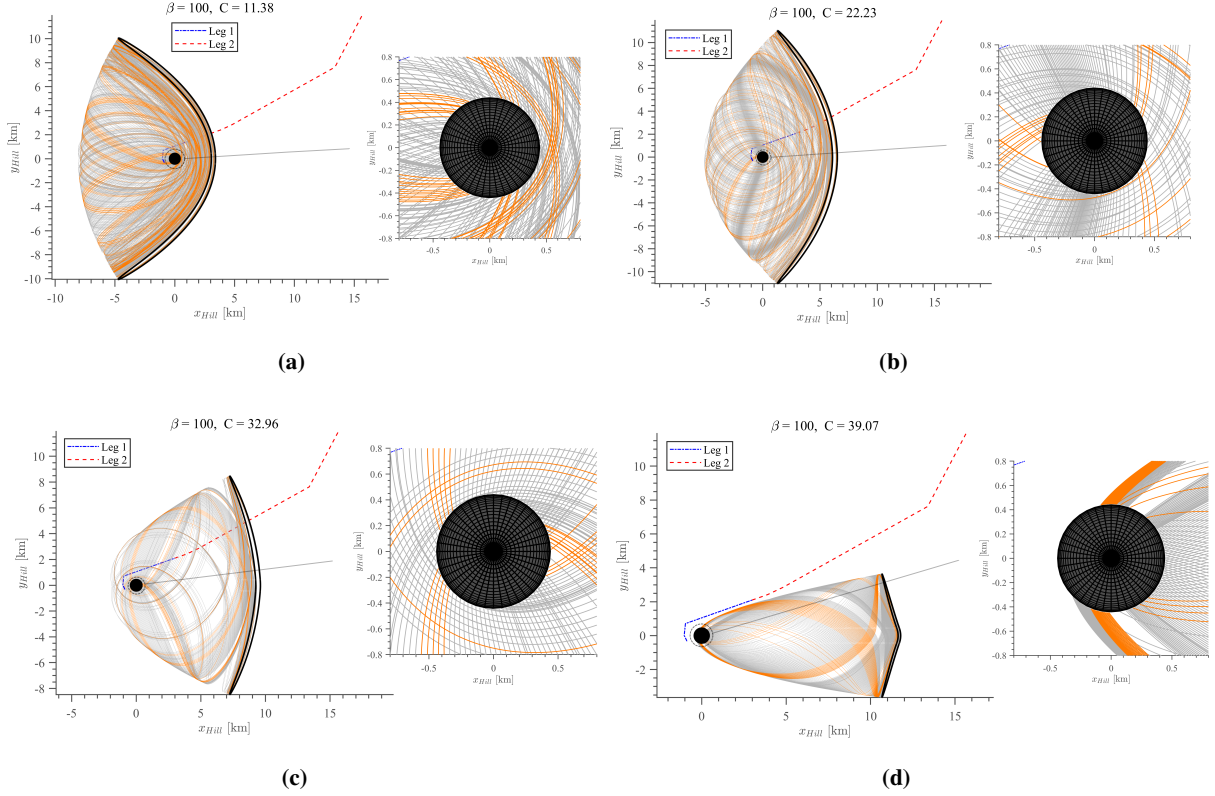


**Fig. 26** Examples of stable manifolds that lead to periodic orbits of family *a* and Hayabusa2’s escape trajectory. The manifold trajectories with ejection angles between  $\sigma \in [35^\circ, 50^\circ]$  are shown in orange.

Table 3 displays the minimum, maximum, and mean times of flight,  $t_{flight}$  from the asteroid surface to the periodic orbits of family *a* of the particles with ejection angles  $\sigma \in [35^\circ, 50^\circ]$ , for different values of  $\beta$ . The minimum and maximum periods of the orbits in the family are also displayed. We note again that even though these orbits are unstable in the mathematical sense, a particle along said orbits would in principle not escape immediately after arriving at the orbits, but rather after a certain number of orbit revolutions. For instance, from Table 3, for  $\beta = 50$ , the minimum time of flight is 42 days; however, in addition to this, the particle will conduct a certain number of revolutions of the periodic orbit. If we consider a minimum of one revolution or period, this would still correspond to an extra 14 days, adding up to a minimum duration of 56 days during which the particle would remain close to the asteroid. Furthermore, note that the periods and times of flight decrease as the value of  $\beta$  increases, i.e., as the radius of the particles decreases. This can be explained by the equation for the Jacobi constant in Eq. (5); for the same position and value of  $C$ , an increase of  $\beta$  will cause the velocity to increase.

**Table 3** Times of flight along the stable manifolds of family  $a$ , between asteroid surface and periodic orbits, with ejection angles between  $\sigma \in [35^\circ, 50^\circ]$  and minimum and maximum periods in family for different values of  $\beta$ .

$\beta$	$\min\{t_{flight}\}$ [days]	$\max\{t_{flight}\}$ [days]	$mean\{t_{flight}\}$ [days]	$\min\{T\}$ [days]	$\max\{T\}$ [days]
30	60.3	149.9	79.3	21.3	38.4
40	49.1	149.2	65.3	17.1	31.2
50	41.9	148.5	55.6	14.4	26.4
75	31.4	148.5	41.4	10.7	19.6
100	25.5	143.1	32.8	8.6	15.9
125	21.8	145.8	27.8	7.3	13.5
150	19.1	135.4	24.2	6.4	11.7
175	17.1	136.9	21.4	5.7	10.5
200	15.5	122.7	19.4	5.2	9.5

### B. Family $g'$

The velocity distribution of the particles ejected along the stable manifolds of family  $g'$  can be seen in Figure 27. The similarity to the velocity distribution of family  $a$  can be explained by the fact that both families exist close to each other in the family curve parameter space, i.e., they have similar values of  $C$  for similar initial positions along the  $x$ -axis, for the entirety of the family curve (see Figure 12). From the energy integral in Eq. (5), their velocities will therefore also be similar for ejection locations.

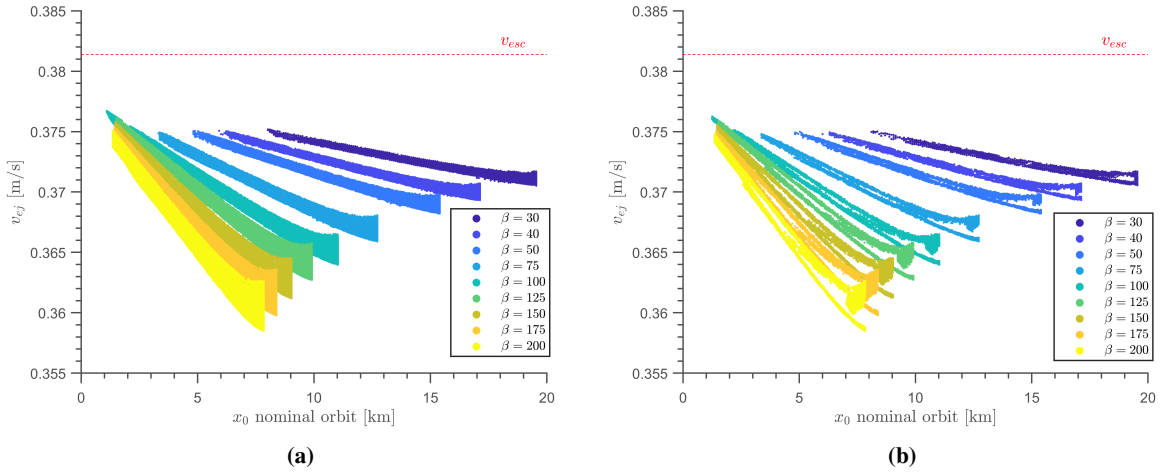


**Fig. 27** Ejection velocities for particles ejected along the stable manifolds of family  $g'$  for different values of SRP acceleration. (a) For any ejection angle; (b) for the expected ejection angles of  $\sigma \in [35^\circ, 50^\circ]$ .

The distribution of locations about the asteroid's equator where the stable manifolds of family  $g'$  intersect the asteroid can be seen in Figures 28 and 29. Both when considering all ejection angles (Figure 28a) and  $\sigma \in [35^\circ, 50^\circ]$  (Figures 28b and 29), the distributions display minima and maxima. When considering all values for  $\sigma$ , we see a clear distribution with a minimum around  $\zeta \approx 90^\circ$  and a maximum between  $\zeta \in [295^\circ, 300^\circ]$ ; for the constrained ejection

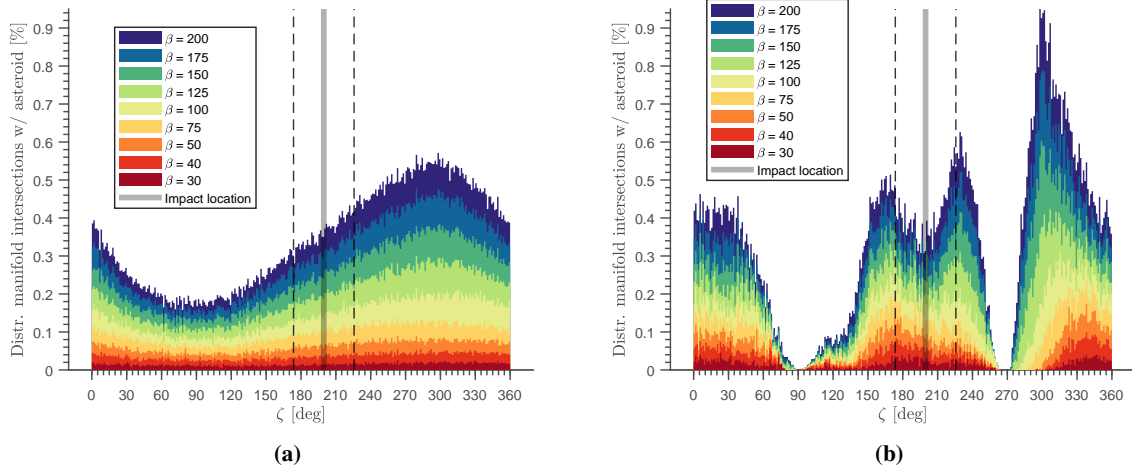


**Fig. 28** Distribution of the ejection locations for particles ejected along the stable manifolds of family  $g'$  for different values of SRP acceleration. (a) For any ejection angle; (b) for ejection angles of  $\sigma \in [35^\circ, 50^\circ]$ .

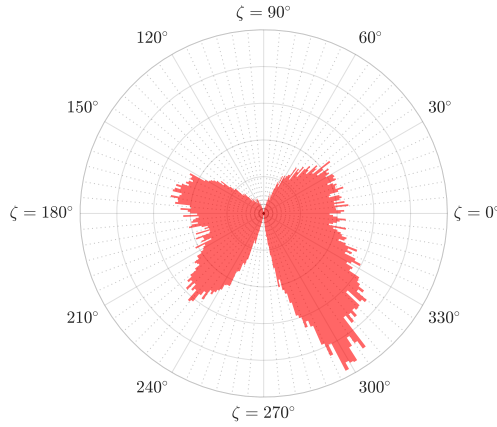


**Fig. 29** Cumulative distribution of the ejection locations in polar coordinates for particles ejected along the stable manifolds of family  $g'$  for all values of SRP acceleration and ejection angles of  $\sigma \in [35^\circ, 50^\circ]$ .

angles, we still see similar extrema, although the minimum becomes more profound and a second minimum appears between  $\zeta \in [260^\circ, 275^\circ]$ . This last minimum is very wide when considering smaller values of  $\beta$ : up to values of  $\beta = 50$ , the minimum extends over a range of  $\Delta\zeta = 30^\circ$ . The same occurs for the minimum around  $\zeta \approx 90^\circ$ . Note also the smaller peaks between  $\zeta \approx 165^\circ, 230^\circ$  and slight valley around  $\zeta \approx 195^\circ$  and when approaching  $\zeta = 360^\circ$ .

The *minima* for this distribution match very closely with the *maxima* found in the distribution of family  $a$  (see Figure 24b). While for family  $g'$  it would make sense to choose an impact location with  $\zeta$  close to the y-axis, i.e.,  $\zeta = 270^\circ$ , family  $a$  shows a high concentration of manifold intersections for those right ascensions. Taking into account the fact that the distribution for family  $a$  does not vary significantly outside the regions where the maxima are located, choosing an impact location that minimizes the chances of ejecta getting captured into orbits of family  $g'$  is recommended, as long

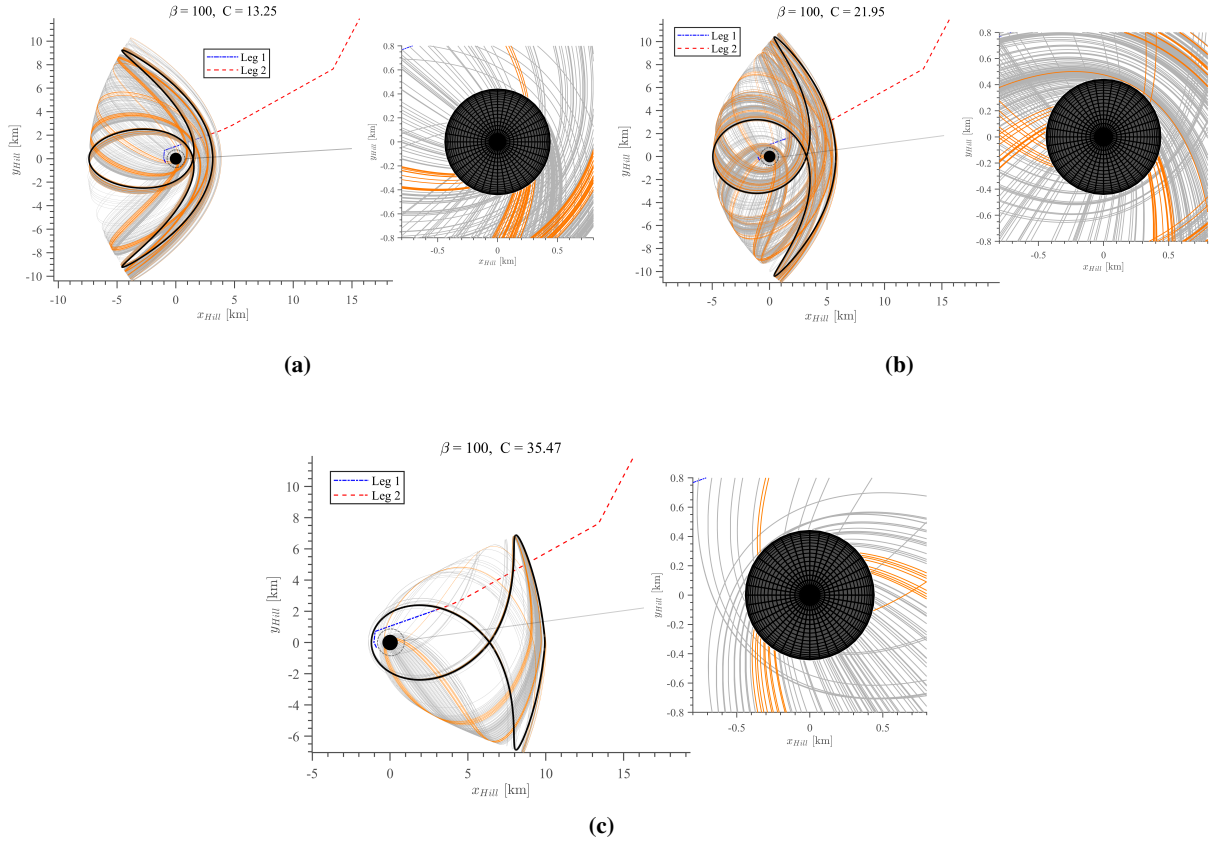


**Fig. 30** Examples of stable manifolds that lead to periodic orbits of family  $g'$  and Hayabusa2's escape trajectory. The manifold trajectories with ejection angles between  $\sigma \in [35^\circ, 50^\circ]$  are shown in orange.

as that location is situated outside the maxima of family  $a$ , i.e., outside locations about  $\zeta \approx 80^\circ$  and  $\zeta \approx 270^\circ$ . For this reason, and taking into account the expected impact angle error of  $\Delta\zeta = 26^\circ$ , if impacting on the equator, we recommend an impact location around  $\zeta = 130^\circ$ , so as to minimize the chances of ejecta getting captured into either orbit family.

The distributions of the ejection locations for family  $g'$  seen in Figure 28 can be explained by the geometry of its stable manifolds and the effect of the angle restriction. Figure 30 shows examples of stable manifold trajectories that depart from the asteroid and get captured into orbits of family  $g'$ , together with the escape trajectory of the Hayabusa2 spacecraft. The stable manifolds seldom intersect the asteroid at right ascensions of  $\zeta = 90^\circ$  and due to the geometry of the trajectories, the ejection angles of said trajectories are rarely within the specified limits. The lack of trajectories within the specified ejection angles is also why we see the minimum between  $\zeta \in [260^\circ, 275^\circ]$ . The maximum for  $\zeta \in [295^\circ, 300^\circ]$  follows the reciprocal reasoning: the geometry of the orbits and their stable manifolds allow for a large number of trajectories to reach those right ascensions, which have, in general,  $\sigma$  within the specified limits.

Finally, Table 4 displays the minimum, maximum, and mean times of flight of the trajectories with ejection angles  $\sigma \in [35^\circ, 50^\circ]$  moving from asteroid surface to the periodic orbits of family  $g'$ , for the different values of  $\beta$ . The

**Table 4** Times of flight along the stable manifolds of family  $g'$ , between asteroid surface and periodic orbits, with ejection angles between  $\sigma \in [35^\circ, 50^\circ]$  and minimum and maximum periods in family for different values of  $\beta$ .

$\beta$	$\min\{t_{flight}\}$ [days]	$\max\{t_{flight}\}$ [days]	$mean\{t_{flight}\}$ [days]	$\min\{T\}$ [days]	$\max\{T\}$ [days]
30	61.0	150.0	110.7	32.0	38.5
40	49.9	150.0	99.4	25.2	31.3
50	44.2	150.0	89.4	21.0	26.6
75	33.0	149.9	73.3	15.2	19.8
100	26.8	150.0	69.0	11.6	16.0
125	22.7	149.5	61.1	9.9	13.6
150	19.9	141.9	49.2	8.7	11.8
175	17.8	148.1	40.6	7.8	10.6
200	16.1	148.1	35.0	7.0	9.6

minimum and maximum times of flight range between 16 days for the smallest sized particles considered (millimeter size), and 61 days for the largest (centimeter size), which excludes the minimum and maximum orbit periods of 5 and 21 days, respectively. Note that even for the smallest particles the maximum time of flight equates to 148 days, a significant value considering the time-span of the mission.

### C. Terminator family

Figure 31 displays the ejection velocities into the stable manifolds of the terminator orbit family as a function of the initial  $x$ -coordinate,  $x_0$ , of the nominal orbit for all ejection angles (Figure 31a) and for  $\sigma \in [35^\circ, 50^\circ]$  (Figure 31b), the ejection velocities as a function of the ejection angle (Figure 31c), and the sections of the family curve whose stable manifolds intersect the asteroid (Figure 31d). Figure 31c shows how the minimal velocities are achieved for  $\sigma \in [40^\circ, 55^\circ]$  and the largest velocities comprise of near vertical ejections. Contrary to families  $a$  and  $g'$ , only part of the orbits of the family generate manifolds that intersect the asteroid: Figure 31d shows how only the stable manifolds from the orbits situated in the regions close to the equilibrium points intersect the asteroid. For the other orbits in the family, the stable manifolds approach the asteroid but never intersect its surface. They simply remain in a quasi-terminator orbit that is situated closer to the asteroid than the original nominal orbit. This situation is shown in Figure 18d in Section IV.A.

Another observation regarding the geometry of the trajectories can be inferred from Figures 31a, 31b, and 31d. Note how the largest ejection velocities in Figure 31a correspond to periodic orbits furthest from the asteroid, i.e., the closest to the equilibrium points. This peak in ejection velocity can also be seen in Figure 31c for  $\sigma \approx 0^\circ$ . This means that the stable manifolds from the terminator orbits closest to the  $L_2$  equilibrium points will depart from the asteroid at the largest velocities and at near vertical trajectories with respect to the local vertical. This also implies that trajectories leading to orbits situated very close to the equilibrium point will likely not be followed by particles ejected from the

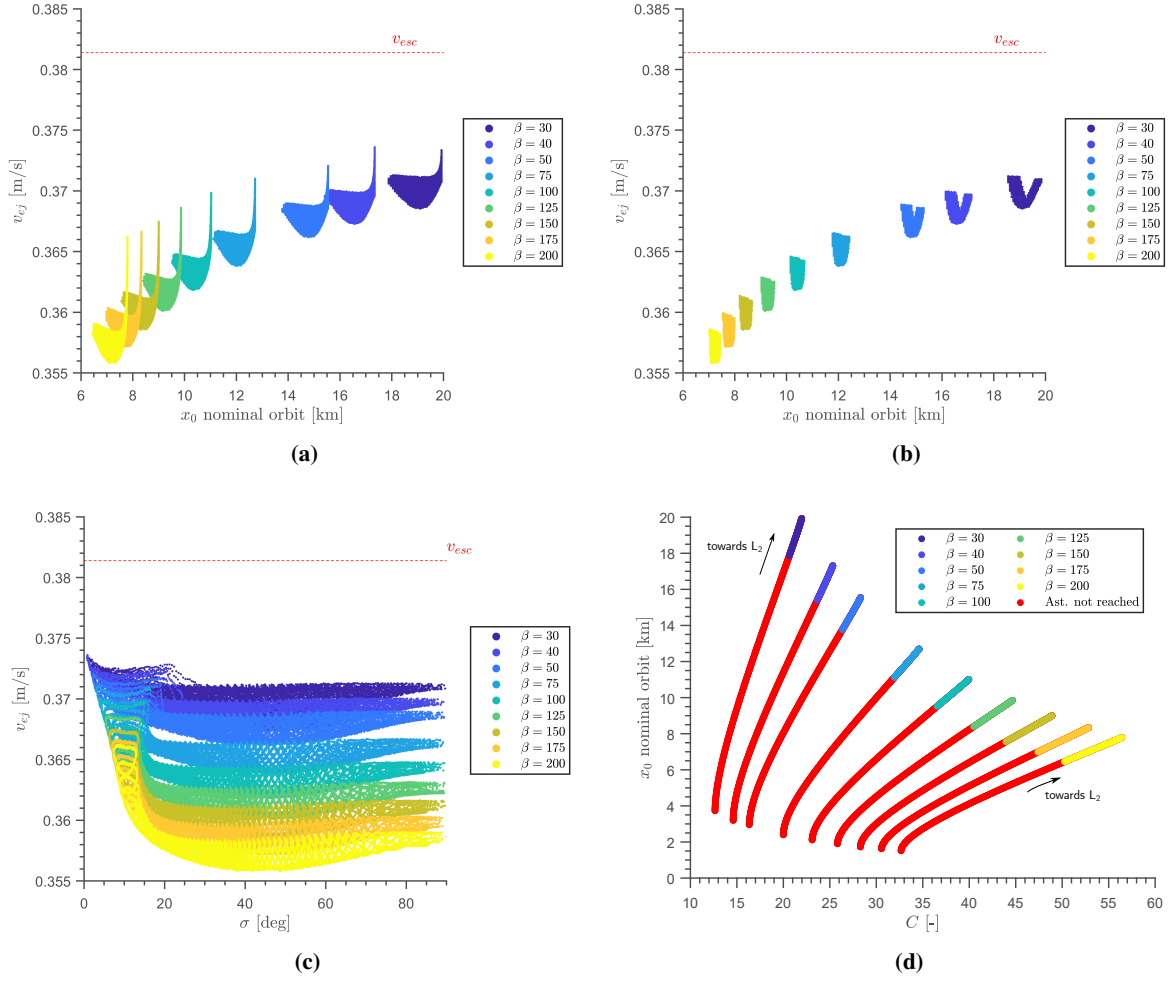


**Fig. 31** (a) Ejection velocities for particles ejected along the stable manifolds of terminator family for different values of the SRP acceleration for any ejection angle; (b) for the expected ejection angles of  $\sigma \in [35^\circ, 50^\circ]$ . (c) Ejection velocity as a function of ejection angle  $\sigma$ . (d) Sections of terminator orbit family for which at least one stable manifold trajectory intersects the asteroid for different values of SRP acceleration.

asteroid surface, due to the ejection angle constraint. This observation can be verified in Figure 32, where several stable manifold trajectories that intersect the asteroid surface are presented. Figures 32a and 32b show examples of orbits that cannot be reached (due to the angle constraint), where specifically Figure 32b displays the aforementioned case. Figures 32c to 32f show examples of trajectories from the asteroid to periodic orbits that can be followed by the ejecta particles.

In Figures 33 and 34, distribution maps of the ejection locations are shown. The color-map and percentage are calculated similarly to Eq. (32), although the distribution is cumulative, i.e., it is summed over all values of  $\beta$

$$D^i = \frac{\sum_{\beta} N_{ej}^i}{\sum_{\beta} N_{total}} \times 100 \quad (33)$$

The nominal impact point and the error radius for three standard deviations are also displayed and plotted in red in the

figures.

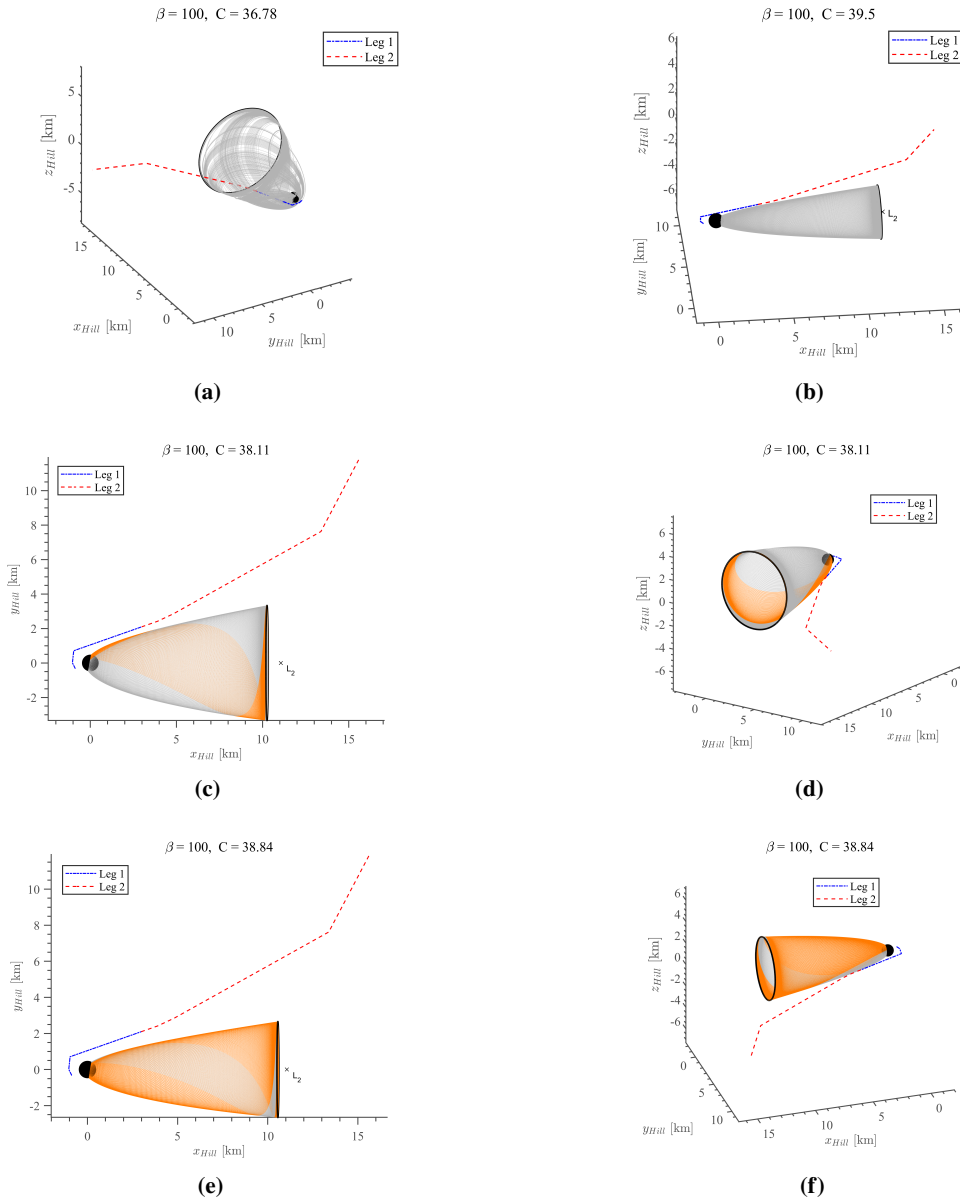


**Fig. 32** Examples of stable manifolds that lead to periodic orbits of terminator family and Hayabusa2's escape trajectory. The manifold trajectories with ejection angles between  $\sigma \in [35^\circ, 50^\circ]$  are shown in orange.

We define the subsolar and anti-subsolar points, which are placed on the intersection between the Sun-asteroid and the asteroid surface on the Sun side and the night side of the asteroid, respectively. Analyzing Figure 33, we see that even when considering all ejection angles, certain locations on the asteroid are never intersected by stable manifold trajectories of the terminator family. These occur around the subsolar ( $\sigma = 180^\circ$ ) and anti-subsolar ( $\sigma = 0^\circ$ ) points, although the region on the Sun side is significantly larger. Moreover, on the night side of the asteroid, we see that this region is surrounded by locations with high concentrations of stable manifold intersections. These high-concentration

regions originate in their majority from the manifolds of the orbits closest to the  $L_2$  point, which, as seen in Figure 32 mainly intersect the asteroid on the night side and around the anti-subsolar point. As the value of  $\beta$  increases and as we approach the  $L_2$  point, the manifolds tend to follow the path of the stable manifolds of the equilibrium point (see Figure 17), which always intersects the asteroid on the night side for sufficiently large values of  $\beta$ . An example of this can be seen in Figure 32b, which displays an orbit that is very close to the equilibrium point; we can see how its stable manifold trajectories intersect the asteroid around the anti-subsolar point. When we only consider  $\sigma \in [35^\circ, 50^\circ]$  (see Figure 34),

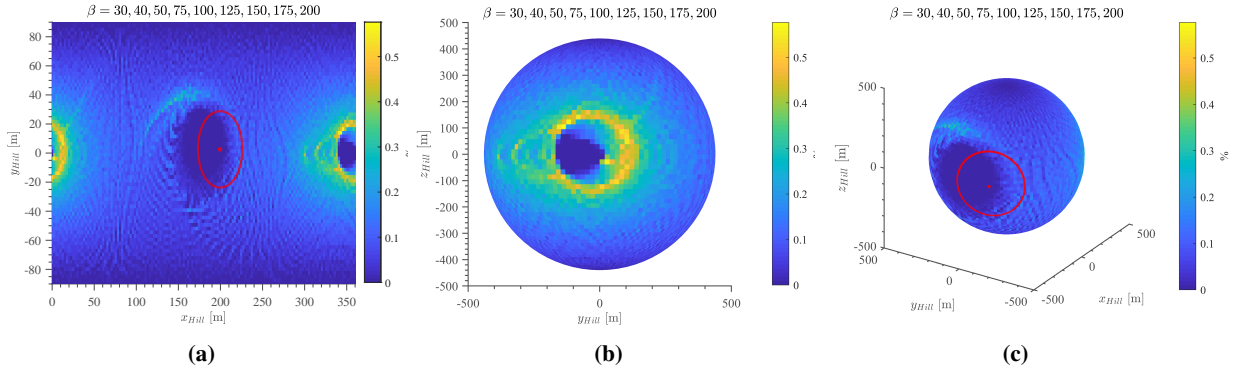


**Fig. 33** Cumulative distribution maps of the ejection locations for particles ejected along the stable manifolds of terminator family when considering any ejection angle.

we see how a well-defined band forms close to the  $yz$ -plane; no manifolds intersect with the asteroid surface outside this band when constraining  $\sigma$ . It is interesting to note that the maximum concentration of intersections occurs near the equator and for  $\zeta \in [70^\circ, 90^\circ]$  and  $\zeta \in [270^\circ, 290^\circ]$ , which are also regions where the manifold intersection distributions of families  $a$  and  $g'$  display maxima. Because the trajectories intersecting those regions have ejection angles outside the defined range, the imposed angle constraint forbids the existence of manifold trajectories in the regions outside the aforementioned band. Figure 35 shows the ejection angles of all the stable manifold trajectories intersecting the asteroid as a function of the right ascension and declination, for an SRP acceleration of  $\beta = 100$ . The figure shows that the ejection angles of the stable manifolds do indeed follow a specific pattern with respect to the ejection location.

Finally, Table 5 provides information regarding the times of flight for the stable manifolds of the terminator family with  $\sigma \in [35^\circ, 50^\circ]$ , as well as the minimum and maximum periods of the orbits in the family for the different values of  $\beta$ . Note that the times of flight and periods are smaller for the terminator family than for families  $a$  and  $g'$ . Moreover, note that for  $\beta \leq 50$  ( $R \leq 3.1$  cm), the times of flight display very small variations with respect to the mean value.

Nonetheless, for  $\beta = 30$  ( $R = 5.2$  cm), a particle ejected along the stable manifolds of a terminator orbit could remain about the asteroid for 160 days (124 + 36). For particles with  $\beta > 150$  ( $R < 1.0$  cm) this time drops to 30 days (19 + 11).

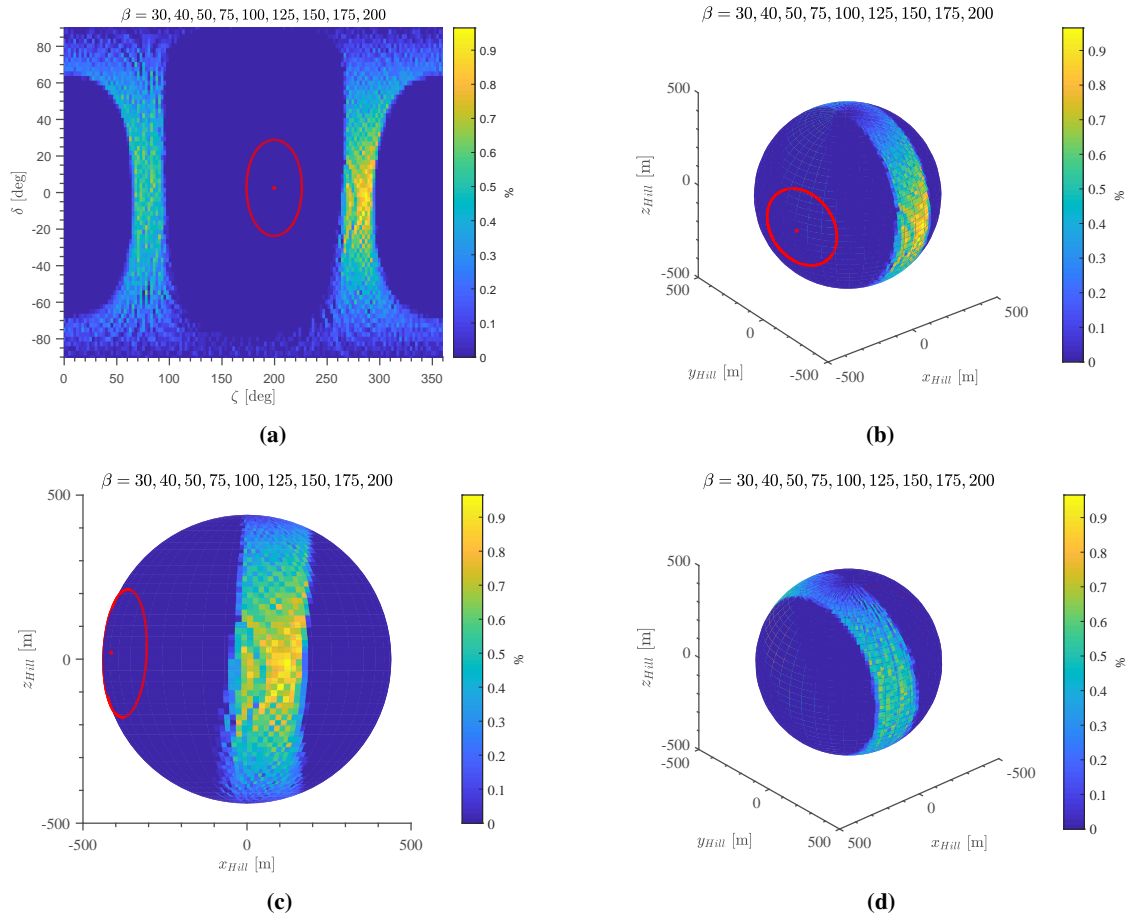


**Fig. 34** Cumulative distribution maps of the ejection locations for particles ejected along the stable manifolds of terminator family for  $\sigma \in [35^\circ, 50^\circ]$ .

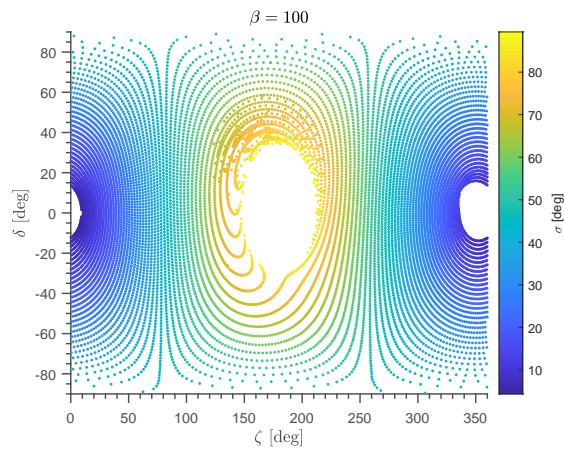


**Fig. 35** Ejection angles  $\sigma$  of stable manifolds of terminator family that intersect asteroid surface as a function of ejection location for  $\beta = 100$ .

**Table 5** Times of flight along the stable manifolds of terminator family, between asteroid surface and periodic orbits, with ejection angles between  $\sigma \in [35^\circ, 50^\circ]$  and minimum and maximum periods in family for different values of  $\beta$ .

$\beta$	$\min\{t_{flight}\}$ [days]	$\max\{t_{flight}\}$ [days]	$mean\{t_{flight}\}$ [days]	$\min\{T\}$ [days]	$\max\{T\}$ [days]
30	59.1	123.9	61.3	35.3	36.2
40	48.1	125.0	48.5	28.6	29.3
50	41.0	41.1	41.0	24.2	24.8
75	30.5	30.6	30.6	17.9	18.3
100	24.8	24.8	24.8	14.4	14.7
125	21.0	21.1	21.1	12.1	12.4
150	18.4	18.5	18.4	10.5	10.8
175	16.5	16.5	16.5	9.4	9.6
200	14.9	15.0	15.0	8.5	8.7

#### D. Implications for Hayabusa2

Although some of the manifold trajectories shown seem to intersect the escape trajectory of the spacecraft, it should be noted that in nominal conditions the SCI should only detonate once the first leg of the escape trajectory is completed, i.e., 40 minutes after the deployment of the SCI [10]. Given the fact that the times of flight of the stable manifold trajectories for the different families are in the order of tens of days and the velocities of the ejecta particles traveling along these trajectories are much smaller than that of the Hayabusa2 spacecraft (and thus cannot reach the spacecraft's position in time), the ejecta moving along the manifold trajectories during the initial segments of Hayabusa2's escape trajectory are considered to be innocuous to the mission.

However, the Hayabusa2 spacecraft is scheduled to return to its nominal position, around 20 km from the asteroid in the direction of the Earth[9], two to four weeks after the SCI operation. An important outcome from the presented results is that, if ejected into the stable manifold trajectories of periodic orbits at the correct velocity, ejecta particles could remain about the asteroid for very long periods of time, captured in periodic orbits. The duration of this temporary capture varies depending on the orbit family and the size of the particle (which translates into different values of  $\beta$ ). The smallest particles will on average remain about the asteroid for shorter periods of time, but can reach values ranging from 21 days to 158 days for particles with a radius of 7.8 mm, and from 81 days to 189 days for particles with a radius of 5.2 cm. These are conservative estimates because the particles are assumed to remain in the periodic orbit for only one orbital revolution. Since these situations would increase the likelihood of ejecta particles colliding with the spacecraft, which, of course, should be avoided, it is useful to take the information here presented into consideration when analyzing the SCI event.

The planned escape trajectory of the spacecraft after the SCI operation consists of a good safety measure for the first period after the impact event. The spacecraft will also be below the  $xy$ -plane (in the negative  $z$ -direction of the Hill frame), which ensures no collision with a planar trajectory can occur.

As mentioned, following the ballistic impact, high-velocity material will also be ejected from the surface. For this reason, it makes sense to place the impact location and the spacecraft on opposite sides of the asteroid during the SCI operation (therefore making sure the spacecraft is not hit by the high-velocity particles). If we assume, from the escape trajectory of Hayabusa2, that the spacecraft will be on the night side of the asteroid when the SCI is detonated, it is appropriate to choose an impact location on the Sun side of the asteroid. Note, however, that both high-velocity and low-velocity material are ejected following a ballistic impact [61, 64]. While the high-velocity ejecta will quickly escape, it is the low-velocity ejecta that could be captured into periodic orbits.

Because the nominal impact location is not situated on the  $xy$ -plane and from Figure 34, we see that the nominal impact location should not lead particles to any of the considered periodic orbits. However, when considering the impact error radius, some particles could be ejected into the stable manifolds of the planar families  $a$  and  $g'$ . We therefore recommend choosing an impact location on the Sun-side whose error radius does not intersect the equator of the asteroid, thereby ensuring no particles will be trapped in the periodic orbits from the  $a$ ,  $g'$ , or terminator families. An impact location on the Sun side of the asteroid at mid-latitudes is thus considered the ideal impact location.

A final remark concerning the safety of Hayabusa2 is made, with respect to the trajectories that ejecta particles might take after their temporary capture. From Figures 1 and 23, we see that for a particle to escape, the ZVCs must be open on the  $L_2$  point. However, because the  $L_2$  point is always on the night side of the asteroid and because the ZVCs do not open on the Sun side the asteroid when considering SRP (only for high-velocity particles, which is not the case of captured ejecta), these particles will not escape into the Sun-direction. For this reason, after being temporarily captured, the ejecta particles will either escape the asteroid's vicinity in the anti-solar direction or re-impact on its surface. Keeping the spacecraft on the Sun side of the asteroid when returning to its vicinity, which as seen in the escape trajectory plots of Figure 20 is the planned scenario, decreases the possibility of ejecta particles colliding with the spacecraft.

## VI. Conclusion

This paper has analyzed the possibility of ejecta particles getting temporarily captured into periodic orbits about asteroid Ryugu following the Small Carry-on Impactor (SCI) operation of the Hayabusa2 mission. Three families of periodic orbits – families  $a$  and  $g'$  from the traditional Hill Problem and the family of southern halo orbits or terminator orbits – have been studied in the dynamical framework of the perturbed Augmented Hill Problem (AHP), which includes the effects of solar radiation pressure (SRP), eclipses, and the oblateness of the asteroid, represented by the  $J_2$  and  $J_4$  terms of its spherical harmonics gravity potential expansion. Under this model, it was shown that centimeter to millimeter sized particles could remain trapped about the asteroid for long periods of time as a consequence of the ballistic impact event, if ejected along the stable manifolds of these periodic orbits. These periods were shown to range from 21 to 189 days in conservative considerations, a value that would limit and possibly jeopardize the mission's

operations. On average, the ejecta particles with smaller radii were shown to remain captured for shorter periods of time than those with larger radii. The conditions for temporary orbital capture into periodic orbits were also investigated, specifically the ejection locations of these particles. We defined the subsolar and anti-subsolar points as the intersection of the Sun-asteroid line with the asteroid surface on the Sun and night sides of the asteroid, respectively. Using this, it was found that a ballistic impact on the equator of the asteroid, approximately  $\pm 80^\circ$  from the anti-subsolar point, would lead to the largest numbers of ejecta particles being captured into the three considered periodic orbits. Specifically, the location at  $-80^\circ$  from the anti-subsolar direction (where the positive direction is given by the angular momentum vector of the asteroid's orbit about the Sun), was shown to be near the maxima for all three families. On the contrary, it was shown that an impact location on the Sun-side of the asteroid, not intersecting the equator, would not cause any particles to be captured into the aforementioned families of periodic orbit. For this reason, and considering an impact error radius, the best impact location for the SCI was considered to be on the Sun-side of the asteroid, at medium latitudes. Additionally, it was found that the ranges of ejection velocities that cause particles to be captured into the three families of periodic orbits were very similar for both different sized particles and different families, ranging between 0.355 and 0.380 m/s. Furthermore, besides verifying the fact that, in general, solar radiation pressure cannot be neglected when studying the dynamical environment around small bodies (both for ejecta particles and spacecraft), other theoretical outcomes were reached in this study. Firstly, it was shown that the stable manifold of the only equilibrium point of the system, which is situated on the night side of the asteroid, intersects the asteroid surface and tends to travel along the Sun-asteroid line for sufficiently large values of solar radiation pressure acceleration (the same will occur for the unstable manifold, although it was not analyzed in this work). Secondly, the effect of the solar radiation pressure on the manifolds of the families of periodic orbits was also analyzed. It was found that their geometry changes significantly and that in the case of libration point orbits (as the terminator and  $a$  families) the shape and direction of their manifolds tend to follow the manifolds of the libration point for increasing values of solar radiation pressure acceleration. Finally, due to the large relative values of solar radiation pressure acceleration, it was concluded that the effect of eclipses should not be neglected. In fact, it was demonstrated that the stability of periodic orbits that pass through eclipse regions changes significantly when including the effect of eclipses. This last observation has not only implications to the study of particle dynamics, but also to the design of space missions.

## References

- [1] Robert, F., "Origin of Water on Earth," *Science*, Vol. 293, No. 5532, 2001, pp. 1056–1058.
- [2] Prockter, L., Murchie, S., Cheng, A., Krimigis, A., Farquhar, R., Santo, A., and Trombka, J., "The NEAR Shoemaker Mission to Asteroid 433 Eros," *Acta Astronautica*, Vol. 51, No. 1-9, 2002, pp. 491–500.
- [3] Fujiwara, A., Kawaguchi, J., Yeomans, D. K., Abe, M., Mukai, T., Okada, T., Saito, J., Yano, H., Yoshikawa, M., Scheeres, D. J.,

- Cheng, A. F., Demura, H., Gaskell, R. W., Hirata, N., Ikeda, H., Kominato, T., Miyamoto, H., Nakamura, A. M., Nakamura, R., Sasaki, S., and Uesugi, K., "The Rubble-Pile Asteroid Itokawa as Observed by Hayabusa," *Science*, Vol. 312, No. June, 2006, pp. 1330–1335.
- [4] Yano, H., Kubota, T., Miyamoto, H., Okada, T., Scheeres, D., Takagi, Y., Yoshida, K., Abe, M., Abe, S., Fujiwara, A., Hasegawa, S., Hashimoto, T., Ishiguro, M., Kato, M., Kawaguchi, J., Mukai, T., Saito, J., Sasaki, S., and Yoshikawa, M., "Touchdown of the Hayabusa Spacecraft at the Muses Sea on Itokawa," *Science*, Vol. 312, No. 5778, 2006, pp. 1350–1354.
- [5] Hechler, M., "Rosetta Mission Design," *Advances in Space Research*, Vol. 19, No. 1, 1997, pp. 127–136.
- [6] Glassmeier, K.-H., Boehnhardt, H., Koschny, D., Kührt, E. K., and Richter, I., "The Rosetta Mission: Flying Towards the Origin," *Space Science Reviews*, Vol. 128, 2007, pp. 1–21. doi:10.1007/s11214-006-9140-8.
- [7] Blume, W. H., "Deep Impact Mission Design," *Space Science Reviews*, Vol. 117, 2005, pp. 23–42. doi:10.1007/s11214-005-3386-4.
- [8] Wissler, S., Rocca, J., and Kubitschek, D., "Deep Impact Comet Encounter: Design, Development and Operations of the Big Event at Tempel 1," *Proceedings of the Space System Engineering Conference*, Pasadena, California, 2005, pp. 1–20.
- [9] Tsuda, Y., Yoshikawa, M., Abe, M., Minamino, H., and Nakazawa, S., "System Design of the Hayabusa 2 - Asteroid Sample Return Mission to 1999 JU3," *Acta Astronautica*, Vol. 91, 2013, pp. 356–362. doi:10.1016/j.actaastro.2013.06.028.
- [10] Saiki, T., Imamura, H., Arakawa, M., Wada, K., Takagi, Y., Hayakawa, M., Shirai, K., Yano, H., and Okamoto, C., "The Small Carry-on Impactor ( SCI ) and the Hayabusa2," *Space Sci Rev*, 2017, pp. 165–186. doi:10.1007/s11214-016-0297-5.
- [11] Scheeres, D. J., and Mazary, F., "Spacecraft Dynamics in the Vicinity of a Comet," *Journal of the Astronautical Sciences*, Vol. 50(1), No. January, 2002, pp. 35–52.
- [12] Snodgrass, C., Tubiana, C., Vincent, J. B., Sierks, H., Hviid, S., Moissl, R., Boehnhardt, H., Barbieri, C., Koschny, D., Lamy, P., Rickman, H., Rodrigo, R., Carry, B., Lowry, S. C., Laird, R. J., Weissman, P. R., Fitzsimmons, A., Marchi, S., A'Hearn, M., Angrilli, F., Barucci, A., Bertaux, J. L., Cremonese, G., Da Deppo, V., Davidsson, B., Debei, S., De Cecco, M., Fornasier, S., Gutiérrez, P., Ip, W. H., Keller, H. U., Knollenberg, J., Kramm, J. R., Kuehrt, E., Kueppers, M., Lara, L. M., Lazzarin, M., López-Moreno, J. J., Marzari, F., Michalik, H., Naletto, G., Sabau, L., Thomas, N., and Wenzel, K. P., "A Collision in 2009 as the Origin of the Debris Trail of Asteroid P/2010 A2," *Nature*, Vol. 467, No. 7317, 2010, pp. 814–816. doi:10.1038/nature09453.
- [13] Vallado, A. D., *Fundamentals of Astrodynamics and Applications*, Microcosm Press/Springer, 1997. doi:10.2514/2.4291.
- [14] Scheeres, D. J., *Orbital Motion in Strongly Perturbed Environments - Applications to Asteroid, Comet and Planetary Satellite Orbiters*, Springer-Verlag Berlin Heidelberg, 2012. doi:10.1007/978-3-642-03256-1.
- [15] Hill, G. W., "Researches in the Lunar Theory," *American Journal of Mathematics*, Vol. 1, No. 4, 1878, pp. 5–26.
- [16] Matakuma, T., "On the Periodic Orbits in Hill's Case," *Proc. Imp. Acad. Tokyo*, Vol. 6, No. 1, 1930, pp. 6–8.

- [17] Henon, M., “Numerical Exploration of the Restricted Problem. V. Hill’s Case: Periodic Orbits and Their Stability,” *Astronomy and Astrophysics*, Vol. 1, No. 2, 1969, pp. 223–238.
- [18] Henon, M., “Numerical Exploration of the Restricted Problem VI. Hill’s Case: Non-Periodic Orbits,” *Astronomy and Astrophysics*, Vol. 9, No. 1, 1970, pp. 24–36.
- [19] Scheeres, D. J., Durda, D. D., and Geissler, P. E., “The Fate of Asteroid Ejecta,” *Asteroids III*, 2002, pp. 527–544.
- [20] Papadakis, K. E., “The Planar Photogravitational Hill Problem,” *International Journal of Bifurcation and Chaos*, Vol. 16, No. 6, 2006, pp. 1809–1821.
- [21] Morrow, E., Scheeres, D. J., and Lubin, D., “Solar Sail Orbit Operations at Asteroids,” *Journal of Spacecraft and Rockets*, Vol. 38, No. 2, 2001, pp. 279–286. doi:10.2514/2.3682.
- [22] Heiligers, J., and Scheeres, D. J., “Solar Sail Orbital Motion About Asteroids and Binary Asteroid Systems,” *Journal of Guidance, Control, and Dynamics*, , No. April, 2018, pp. 1–18. doi:10.2514/1.G003235.
- [23] Farrés, A., Jorba, À., and Mondelo, J.-M., “Orbital Dynamics for a Non-Perfectly Reflecting Solar Sail Close to an Asteroid,” *Advances in the Astronautical Sciences*, Vol. 153, 2015, pp. 1229–1247.
- [24] Basiana Farrés, A., Soldini, S., and Tsuda, Y., “JAXA’s Trojan Asteroids Mission: Trajectory Design of the Solar Power Sail and its Lander,” *4th International Symposium on Solar Sailing*, 2017, pp. 1–7.
- [25] Broschart, S. B., and Villac, B. F., “Identification of Non-Chaotic Terminator Orbits near 6489 Golevka,” *Advances in the Astronautical Sciences*, Vol. 134, No. February 2009, 2009, pp. 861–880. doi:10.13140/2.1.1246.8484.
- [26] Scheeres, D. J., “Satellite Dynamics about Asteroids,” *Advances in the Astronautical Sciences*, Vol. 87, No. 1, 1994, pp. 275–292.
- [27] Dankowicz, H., “Some Special Orbits in the Two-Body Problem with Radiation Pressure,” *Celestial Mechanics & Dynamical Astronomy*, Vol. 58, No. 4, 1994, pp. 353–370. doi:10.1007/BF00692010.
- [28] Scheeres, D. J., Williams, B. G., and Miller, J. K., “Evaluation of the Dynamic Environment of an Asteroid: Applications to 433 Eros,” *Advances in the Astronautical Sciences*, Vol. 102 II, No. 3, 1999, pp. 835–848. doi:10.2514/2.4552.
- [29] Howell, K. C., “Three-Dimensional, Periodic, ‘Halo’ Orbits,” *Celestial Mechanics*, Vol. 32, 1984, pp. 53–71.
- [30] Broschart, S. B., Lantoine, G., and Grebow, D. J., “Quasi-Terminator Orbits near Primitive Bodies,” *Celestial Mechanics and Dynamical Astronomy*, Vol. 120, No. 2, 2014, pp. 195–215. doi:10.1007/s10569-014-9574-3.
- [31] Giancotti, M., Campagnola, S., Tsuda, Y., and Kawaguchi, J., “Families of Periodic Orbits in Hill’s Problem with Solar Radiation Pressure: Application to Hayabusa 2,” *Celestial Mechanics and Dynamical Astronomy*, Vol. 120, No. 3, 2014, pp. 269–286. doi:10.1007/s10569-014-9564-5.

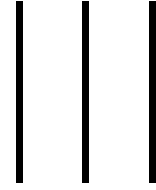
- [32] García Yarnoz, D., and McInnes, C. R., “On the a and g Families of Orbits in the Hill Problem with Solar Radiation Pressure and their Application to Asteroid Orbiters,” *Celestial Mechanics & Dynamical Astronomy*, Vol. 121, 2015, pp. 365–384. doi:10.1007/s10569-015-9604-9.
- [33] Scheeres, D. J., Ostro, S. J., Hudson, R. S., and Werner, R. A., “Orbits close to Asteroid 4769 Castalia,” *Icarus*, Vol. 121, No. 1, 1996, pp. 67–87. doi:10.1006/icar.1996.0072.
- [34] Soldini, S., and Tsuda, Y., “Assessing the Hazard Posed by Ryugu Ejecta Dynamics on Hayabusa2 Spacecraft,” *26th International Symposium of Space Flight Dynamics*, 2017, pp. 1–11.
- [35] Hamilton, D. P., and Krivov, A. V., “Circumplanetary Dust Dynamics: Effects of Solar Gravity, Radiation Pressure, Planetary Oblateness, and Electromagnetism,” *Icarus*, Vol. 123, No. 2, 1996, pp. 503–523. doi:10.1006/icar.1996.0175.
- [36] Szebehely, V., *Theory of Orbits - The Restricted Problem of Three Bodies*, Academic Press, 1967.
- [37] McInnes, C., *Solar Sailing: Technology, Dynamics and Mission Applications*, Springer-Verlag Berlin Heidelberg, 1999. doi:10.2514/2.4604.
- [38] Mueller, T. G., Durech, J., Hasegawa, S., Abe, M., Kawakami, K., Kasuga, T., Kinoshita, D., Kuroda, D., Urakawa, S., Okumura, S., Sarugaku, Y., Miyasaka, S., Takagi, Y., Weissman, P. R., Choi, Y. J., Larson, S., Yanagisawa, K., and Nagayama, S., “Thermo-Physical Properties of 162173 (1999 JU3), a Potential Flyby and Rendezvous Target for Interplanetary Missions,” *Astronomy and Astrophysics*, Vol. 525, No. A145, 2011, pp. 1–6. doi:10.1051/0004-6361/201015599.
- [39] García Yárnoz, D., Sanchez, J.-P., and McInnes, C. R., “Alternating Orbiter Strategy for Asteroid Exploration,” *Journal of Guidance, Control, and Dynamics*, Vol. 38, No. 2, 2015, pp. 280–291. doi:10.2514/1.G000562.
- [40] Han, J., and Moraga, C., “The Influence of the Sigmoid Function Parameters on the Speed of Backpropagation Learning,” *From Natural to Artificial Neural Computation*, edited by J. Mira and F. Sandoval, Springer Berlin Heidelberg, 1995, pp. 195–201.
- [41] Yang, X., Liu, J., Yang, Y., Qing, Q., and Wen, G., “An Efficient Topology Description Function Method Based on Modified Sigmoid Function,” *Mathematical Problems in Engineering*, Vol. 2018, 2018, pp. 1–12.
- [42] Scheeres, D. J., “Orbit Mechanics About Asteroids and Comets,” *Journal of Guidance, Control, and Dynamics*, Vol. 35, No. 3, 2012, pp. 987–997. doi:10.2514/1.57247.
- [43] Markakis, M. P., Perdiou, A. E., and Douskos, C. N., “The Photogravitational Hill Problem with Oblateness: Equilibrium Points and Lyapunov Families,” *Astrophysics and Space Science*, Vol. 315, 2008, pp. 297–306. doi:10.1007/s10509-008-9831-6.
- [44] Sharma, R. K., “The Linear Stability of Libration Points of the Photogravitational Restricted Three-Body Problem when the Smaller Primary is an Oblate Spheroid,” *Astrophysics and Space Science*, Vol. 135, 1987, pp. 271–281.
- [45] Rossi, A., Marzari, F., and Farinella, P., “Orbital Evolution around Irregular Bodies,” *Earth Planets Space*, Vol. 51, 1999, pp. 1173–1180.

- [46] Villac, B. F., and Scheeres, D. J., “Escaping Trajectories in the Hill Three-Body Problem and Applications,” *Journal of Guidance, Control, and Dynamics*, Vol. 26, No. 2, 2003, pp. 224–232. doi:10.2514/2.5062.
- [47] Miele, A., “Revisit of the Theorem of Image Trajectories in the Earth-Moon Space,” *Journal of Optimization Theory and Applications*, Vol. 147, No. 3, 2010, pp. 483–490. doi:10.1007/s10957-010-9734-x.
- [48] Nayfeh, A. H., and Balachandran, B., *Applied Nonlinear Dynamics*, John Wiley & Sons, Inc, New York, 1995.
- [49] Montenbruck, O., and Eberhard, G., *Satellite Orbits - Models, Methods and Applications*, Springer-Verlag Berlin Heidelberg, 2000.
- [50] Parker, J. S., and Anderson, R. L., *Low-Energy Lunar Trajectory Design*, Jet Propulsion Laboratory, Pasadena, California, 2013. doi:10.1002/9781118855065.
- [51] Broucke, R. A., “Periodic Orbits in the Restricted Three-Body Problem with Earth-Moon Masses,” Tech. rep., National Aeronautics and Space Administration, Pasadena, California, 1968.
- [52] Broucke, R., “Stability of Periodic Orbits in the Elliptic, Restricted Three-Body Problem,” *AIAA*, Vol. 7, No. 6, 1969, pp. 1003–1009. doi:10.2514/3.5267.
- [53] Muñoz-Almaraz, F. J., Freire, E., Galán, J., Doedel, E., and Vanderbauwhede, A., “Continuation of Periodic Orbits in Conservative and Hamiltonian Systems,” *Physica D*, Vol. 181, 2003, pp. 1–38. doi:10.1016/S0167-2789(03)00097-6.
- [54] Doedel, E., Keller, B. H., and Kernevez, J. P., “Numerical Analysis and Control of Bifurcation Problems (I) Bifurcation in Finite Dimensions,” *International Journal of Bifurcation and Chaos*, Vol. 1, No. 3, 1991, pp. 493–520.
- [55] Doedel, E. J., Romanov, V. A., Paffenroth, R. C., Keller, H. B., Dichmann, D. J., Galán-Vioque, J., and Vanderbauwhede, A., “Elemental Periodic Orbits Associated with the Libration Points in the Circular Restricted 3-Body Problem,” *International Journal of Bifurcation and Chaos*, Vol. 17, No. 8, 2007, pp. 2625–2677.
- [56] Stramacchia, M., Colombo, C., and Bernelli-Zazzera, F., “Distant Retrograde Orbits for Space-based Near Earth Objects detection,” *Advances in Space Research*, Vol. 58, No. 6, 2016, pp. 967–988. doi:10.1016/j.asr.2016.05.053, URL <http://dx.doi.org/10.1016/j.asr.2016.05.053>.
- [57] Scheeres, D. J., “Satellite Dynamics about Small Bodies: Averaged Solar Radiation Pressure Effects,” *Advances in Astronautical Sciences*, Vol. 47, 1999, pp. 25–46.
- [58] Broschart, S. B., Scheeres, D. J., and Villac, B. F., “New Families of Multi-Revolution Terminator Orbits near Small Bodies,” *Advances in Astronautical Sciences*, Vol. 135, 2010, pp. 1685–1702.
- [59] Scheeres, D. J., and Marzari, F., “Temporary Orbital Capture of Ejecta from Comets and Asteroids: Application to the Deep Impact Experiment,” *Astronomy and Astrophysics*, Vol. 756, 2000, pp. 747–756.

- [60] Yu, Y., Michel, P., Schwartz, S. R., Naidu, S. P., and Benner, L. A., “Ejecta Cloud from the AIDA Space Project Kinetic Impact on the Secondary of a Binary asteroid: I. Mechanical Environment and Dynamical Model,” *Icarus*, Vol. 282, 2017, pp. 313–325. doi:10.1016/j.icarus.2016.09.008.
- [61] Melosh, H. J., *Impact Cratering - A Geologic Process*, Oxford University Press, 1989.
- [62] Hartmann, W. K., “Impact Experiments - 1. Ejecta Velocity Distributions and Related Results from Regolith Targets,” *Icarus*, Vol. 63, 1985, pp. 69–98.
- [63] Gladman, B. J., Burns, J. A., Duncan, M. J., and Levison, H. F., “The Dynamical Evolution of Lunar Impact Ejecta,” *Icarus*, Vol. 118, 1995, pp. 302–321.
- [64] Cintala, M. J., Berthoud, L., and Horz, F., “Ejection-Velocity Distributions from Impacts into Coarse-Grained Sand,” *Meteoritics & Planetary Science*, Vol. 34, 1999, pp. 605–623.
- [65] Anderson, J. L. B., Schultz, P. H., and Heineck, J. T., “Asymmetry of Ejecta Flow during Oblique Impacts using Three-Dimensional Particle Image Velocimetry,” *Journal of Geophysical Research*, Vol. 108, No. E8, 2003, pp. 1–10. doi:10.1029/2003JE002075.
- [66] Gault, D. E., and Wedekind, J. A., “Experimental Studies of Oblique Impact,” *Proceedings of the 9th Lunar and Planetary Science Conference*, 1978, pp. 3843–3875.
- [67] Pierazzo, E., and Melosh, H. J., “Understanding Oblique Impacts from Experiments, Observations, and Modeling,” *Annual Review of Earth Planetary Science*, Vol. 67, 2000, pp. 28–141.
- [68] Melosh, H. J., “Impact Ejection, Spallation, and the Origin of Meteorites,” *Icarus*, Vol. 59, 1984, pp. 234–260.
- [69] Farquhar, R., Muhonen, D., Newman, C., and Heuberger, H., “The First Libration-Point Satellite: Mission Overview and Flight History,” *AAS/AIAA Astrodynamics Specialist Conference*, Provincetown, MA, 1979, pp. 79–126.
- [70] Koon, W. S., Lo, M. W., Marsden, J. E., and Ross, S. D., “Shoot the Moon,” *AAS/AIAA Space Flight Mechanics*, 2000, pp. 1–8.
- [71] Haapala, A. F., and Howell, K. C., “A Framework for Constructing Transfers Linking Periodic Libration Point Orbits in the Spatial Circular Restricted Three-Body Problem,” *International Journal of Bifurcation and Chaos*, Vol. 26, No. 5, 2016, pp. 1–40. doi:10.1142/s0218127416300135.
- [72] Heiligers, J., Mingotti, G., and McInnes, C. R., “Optimal Solar Sail Transfers Between Halo Orbits of Different Sun-Planet Systems,” *Advances in Space Research*, Vol. 55, No. 5, 2015, pp. 1405–1421.
- [73] Heiligers, J., “Homo- and Heteroclinic Connections in the Planar Solar-Sail Earth-Moon Three-Body Problem,” *Frontiers in Applied Mathematics and Statistics*, Vol. 4, No. October, 2018, pp. 1–17. doi:10.3389/fams.2018.00042.
- [74] Koon, W. S., Lo, M. W., Marsden, J. E., and Ross, S. D., *Dynamical Systems, the Three-Body Problem and Space Mission Design*, 2011.

- [75] Gómez, G., Jorba, A., Masdemont, J., and Simó, C., “Study Refinement of Semi-Analytical Halo Orbit Theory, Final Report, ESOC Contract No.:8625/89/D/MD(SC),” Tech. rep., 1991.





# Conclusions and Recommendations

This chapter recovers the research questions and objectives presented in Chapter I in order to understand to which extent these were fulfilled, as well as present recommendations for future work to continue the study developed in this thesis or pursue other applications in which the methodology and conclusions reached could be employed.

## III.1. Review of Research Questions

A final examination of the main research question and subsequent sub-questions follows, with the purpose of retrospectively analyzing the outcomes of the research. We answer each of the sub-questions presented in Chapter I in order to answer the main research question, here restated:

**Can ejecta that is temporarily captured into periodic orbits following Hayabusa2's SCI operation pose a danger to the spacecraft?**

For answering the sub-questions:

1. *What type of dynamical environment exists about asteroid Ryugu and what is the effect of the perturbations posed by the SRP, the eclipses, and the  $J_2$ ,  $J_4$  terms of the asteroid's gravity potential expansion?*

Although it is difficult to quantify and describe the dynamical environment experienced by the ejecta particles in words, we can assertively confirm that the SRP is an essential perturbation to the system. The SRP accelerations were shown to be in the order of magnitude of asteroid Ryugu's gravity and even dominate its gravity for distances larger than 20 and 10 km from the asteroid for particles with radii equal to 5.2 cm and 7.8 mm, respectively. Moreover, the increase in SRP acceleration causes the only equilibrium point of the system, the  $L_2$  point, which is situated on the Sun-asteroid line in the direction opposite to the Sun, to approach the asteroid for increasing values of SRP acceleration (i.e., smaller particles). Although this has previously been studied and is a general remark in the Augmented Hill Problem (AHP), we find it also has important implications in the structure of the manifolds of the equilibrium point. We find that for increasing values of SRP acceleration, the trajectory defined by the interior stable manifold of the  $L_2$  point approaches the asteroid, intersecting it for sufficiently large values of SRP acceleration as the manifold trajectory progressively travels closer to the Sun-asteroid line<sup>1</sup>. Likewise, the manifolds of the families of periodic orbits are also affected by the SRP. For libration point orbits, as the  $a$  and terminator families, their manifolds' shape approach the structure defined by the manifold of the  $L_2$  point, therefore becoming more symmetric with respect to the Sun-asteroid line with the increase in SRP acceleration. For the periodic orbits that are particularly close to the equilibrium point, this also means that their manifolds will intersect with the asteroid similarly to the manifold of the equilibrium

<sup>1</sup>Note that although only the stable manifolds are analyzed, the unstable manifolds will behave similarly, also intersecting the asteroid for sufficiently large values of SRP acceleration

point. The SRP also affects the geometry of the manifolds of non libration point orbits, causing their general size to decrease with the increase in SRP acceleration.

Due to the large values of SRP acceleration considered, we find that eclipses introduce a significant perturbation to the trajectories that cross regions in eclipse. In fact, one of the interesting outcomes of this thesis relates specifically to the effect that eclipses have on periodic orbits. We find that, when considering SRP, the stability of the periodic orbits may be significantly affected by the inclusion of eclipses. Family  $g'$ , which is stable when ignoring eclipses, becomes unstable once said perturbation is included. On the other hand, family  $a$  becomes more stable when including the effect of eclipses, despite remaining unstable. This observation can have important implications in the orbit design of missions to small bodies, proving that accounting for the effect of the SRP and eclipses might lead to different choices in mission design and create a more realistic model of the dynamics. Moreover, not that within the eclipse region, the equilibrium point will occupy the nominal position for the traditional Hill Problem, i.e., when the SRP is not considered. This allows periodic orbits to populate regions in space which would otherwise not maintain said orbits. The inclusion of the  $J_2$ ,  $J_4$  terms of the asteroid's gravity spherical harmonics expansion do not have such a significant effect on the dynamical environment and the periodic orbits of the system. Nonetheless, it accounts for a more truthful representation of the system.

Finally, we can compare the considerations of the model used in this thesis and the actual environment about asteroid Ryugu. In our model, we assume that the asteroid is in a circular orbit about the Sun, at a constant distance. In reality this is not the case, which will mainly affect the intensity of the SRP. However, due to Hayabusa2's mission timeline - the spacecraft plans to return to the asteroid two weeks after the SCI operation - and the asteroid's 1.3 year period about the Sun [13], we consider the variation in the distance to the Sun to be negligible in our model. We also consider the ejecta particles to be perfect spheres with a constant exposed surface area (to the SRP). In reality the ejecta particles will likely have irregular shapes with non-constant exposed areas and varying angles between the surface normal and the incident SRP, which will make the local SRP acceleration to each particle change as a function of time. We are also neglecting the collisions between the ejecta particles, although sufficient ejecta material is expected to be excavated so that a large enough number of ejecta trajectories do not collide with one another. Another perturbation we neglect in our analysis relates to the non-oblate terms of the asteroid's gravity. Given that these terms vary with the local longitude of the asteroid, the spin of the asteroid would create a time-varying gravity field and restrict the type of ideal periodic motion studied in this thesis. Despite all this, we note that the conclusions reached in this study still hold a very relevant significance. While the aforementioned perturbations will most definitely affect the ideal trajectories and orbits described in this thesis, the fact that these perturbations are significantly smaller than the ones included in our model, means that the dynamics of the latter will dominate over the dynamics of the former. In reality we will not observe the ideal trajectories plotted in some of the figures in this thesis, but that is not to say we will not observe trajectories that are very similar to those described. For this reason, the conclusions reached in this thesis should not be regarded as the result of an analytical calculation and demonstration that completely describes the physical world - *they* are not -, but rather, as results that correlate significantly to real dynamics of the physical environment and from which we can take approximate quantitative and qualitative conclusions, and possibly test the reached results in other high-fidelity models.

## 2. *What are the initial conditions that lead ejecta particles to periodic orbits and thus temporary capture?*

We find that, due to the small mass of the asteroid, the velocities for which asteroid ejecta are trapped in periodic orbits are, likewise, very small. However, and most interestingly, the ranges of ejection velocities that cause periodic orbit capture were found to be very similar for both different sized particles and different families of periodic orbits. In the case of Ryugu, this range consists of velocities between 0.355 m/s and 0.380 m/s, or 20.886 and 22.357 in dimensionless units<sup>2</sup>.

Regarding the locations on the asteroid that lead to periodic orbit capture, we show they vary from family to family but that their distribution does not change significantly for different sized particles. By mapping the intersections of the stable manifolds of the periodic orbits with the asteroid surface, we were able to derive the relation between impact location and capture of ejecta into periodic orbits. We found that for family  $a$ , the impact locations that lead to the largest number of trapped ejecta exist close to

<sup>2</sup>The unit of length used corresponds to  $(\mu/\omega^2)^{1/3}$ , where  $\mu$  is the asteroid's gravitational parameter and  $\omega$  is its mean motion about the Sun, and the unit of time corresponds to  $1/\omega$ .

$\pm 80^\circ$  from the anti-subsolar point<sup>3</sup> on the asteroid's equator. For family  $g'$ , this location exists also on the equator, approximately  $60^\circ$  degrees from the asteroid's anti-subsolar point in negative direction<sup>4</sup>. Two minima for the locations that lead to the least number of captured ejecta for family  $g'$  are identified for  $\pm 90^\circ$  from the anti-subsolar point on the asteroid's equator. Finally, for the terminator family, we find that ejecta arising from the SCI event can only be captured if the impact location is placed on a "ring-like" section situated between the  $yz$ -plane<sup>5</sup> and a plane offset 200 m from the  $yz$ -plane in the anti-solar direction. Within this section, the locations that cause the largest number of captured ejecta are situated close to the equator, with the maximum between  $70^\circ$  to  $80^\circ$  from the anti-subsolar point on the asteroid's equator in negative direction.

3. *For what duration do the ejecta particles remain captured about the asteroid?*

The duration of the capture periods varies with the size of the particles and the family of orbits considered. The capture time comprises the time of flight between the asteroid and the periodic orbit and one period (one revolution) of the orbit. This is a conservative consideration, given that a particle arriving at an orbit through its stable manifolds is likely to remain in orbit for longer than one revolution. However, to consider the effect of neglected perturbations, we assume that the particles only remain in orbit for one revolution. Taking this into account, we find average capture periods ranging between 21 and 189 days, which, considering the timeline of the mission, could limit Hayabusa2's future operations. These values are based on the overall minimum and maximum expected capture times, which refer to the minimum capture time of an ejecta particle with a radius of 7.8 mm and the maximum capture time of a particle with a radius of 5.2 cm, respectively. Finally, the capture times for families  $a$  and  $g'$ , which are very similar, are on average larger than those for the terminator family.

4. *What is the effect of particle radius in the dynamics experienced by the ejecta particles, in terms of temporary capture?*

The decrease in particle radius causes the SRP acceleration to increase, as it depends on the area-to-mass ratio of the particles, which decreases for smaller ejecta radii. This increase in the SRP acceleration represents a decrease in the period and size of the periodic orbits, although we find it does not particularly affect the stability of the families for the values of particle radii studied. Nonetheless, we find that, on average, the times of flight between ejection and arrival at the periodic orbits also decrease with a decrease in particle size, meaning that the captured periods decrease for decreasing particle radii. Finally, and although, as mentioned, the ejection velocities that cause periodic orbit capture do not vary significantly with particle radius, the minimum ejection velocities increase slightly with particle radius (i.e., decrease in SRP acceleration). Moreover, the maximum ejection velocities of the terminator family also increase with particle size, while for the  $a$  and  $g'$  families the maximum ejection velocities remain approximately constant for the different particle sizes.

5. *What trajectories do the captured ejecta particles follow and do they pose a danger to the Hayabusa2 spacecraft?*

The immediate danger to the mission is that the ejecta trajectories may collide with the Hayabusa2 spacecraft during its escape trajectory after the SCI deployment. The escape trajectory consists of three legs [14]:

- (a) The first starts immediately after the deployment of the SCI, lasts for 40 min, and consists of the Hayabusa2 spacecraft hiding behind the asteroid, in order to protect itself from the debris created by the detonation of the SCI.
- (b) The second begins once the spacecraft is already behind the asteroid and once the SCI is detonated. During this section the spacecraft proceeds to increasing the distance to the asteroid.
- (c) The third and final segment starts once the spacecraft is further away from the asteroid. It consists of a long trajectory arc that increases the distance to the asteroid by over 100 km and then returns to the nominal "Home Position" of the spacecraft, 20 km away from the asteroid along the asteroid-Earth line, which will situate the spacecraft on the Sun-side of the asteroid.

<sup>3</sup>The anti-subsolar point is defined as the point, on the night-side of the asteroid (side facing the direction opposite to the Sun), where the Sun-asteroid line intersects the asteroid surface.

<sup>4</sup>The positive direction is given by the angular momentum vector of the asteroid's orbit about the Sun.

<sup>5</sup>The  $yz$ -plane is perpendicular to the Sun-asteroid line where the  $z$ -axis points in the direction of the angular momentum vector of the asteroid's orbit about the Sun.

If the nominal conditions are followed, and the SCI is detonated, as planned, 40 min after deployment – when the spacecraft starts the second leg of the escape trajectory –, the average velocity of the spacecraft would be approximately one order of magnitude larger than the ejection velocities that lead the particles to the periodic orbits through their stable manifolds. This means that even though some of the stable manifold trajectories cross points in the escape trajectory, they will do so after the spacecraft has passed that part of the escape trajectory. One could argue that particles with ejection velocities larger than the ejection velocities that lead to periodic orbits could reach the spacecraft sooner, possibly colliding with the spacecraft. The problem with this argument is that the ejection velocities that cause periodic orbit capture are very close to the escape velocity<sup>6</sup>, which is approximately 0.381 m/s from the surface of asteroid Ryugu. Given that the average velocity of the spacecraft will still be approximately an order of magnitude larger than this value, for a particle to reach the spacecraft during the escape trajectory, its velocity would have to be, on average, almost 10 times larger than the escape velocity. Given the fact that the location of the planned impact is on the Sun side of the asteroid and the escape trajectory is on the night side, the trajectories of these particles would likely not intersect the escape trajectory of the spacecraft. In this regard, what is identified as a potential hazard to the mission is the possibility of ejecta particles still remaining about the asteroid when the spacecraft returns to its proximity. This could affect the mission’s nominal operations and the planned touchdown on the impact site.

6. *What are the best and worst impact locations for the SCI in terms of possibility of orbital capture and safety of the spacecraft?*

The best impact locations for the SCI are found to be on the Sun-side of the asteroid at medium latitudes, in such a way that the impact error radius does not intersect the equator nor the plane normal to the Sun-asteroid line that passes through the center of the asteroid. The worst impact location was found to be on the equator of the asteroid, approximately 80° from the anti-subsolar point in negative direction.

## III.2. Recommendations

### III.2.1. Future Work

Following the work developed in this thesis and the conclusions reached, a list of recommendations regarding points that are deemed as possible continuations of said work are presented. We consider the pursuit of these points to be interesting additions to the topic, and that future work on it would benefit from their consideration.

1. *Studying other families of three-dimensional periodic orbits.*

While the two families of planar periodic orbits studied in this thesis provide representative results of the planar motion about the asteroid, additional three-dimensional orbits would present an interesting addition to the results obtained. The terminator orbits are libration point that leads to a large variety of other orbits by means of different numerical or mathematical methods, such as bifurcation theory or invariant tori [31, 32]. For that reason, the terminator orbits studied in this report provide significant and representative conclusions for possible three-dimensional motion about the asteroid. Moreover, being a libration point orbit implies a relation with the gateway that is represented by the L<sub>2</sub> point between impacting, orbiting, and escaping motion, due to the regions of forbidden and allowed motion represented by the Zero Velocity Curves (ZVCs) of the system [5]. However, it would be interesting to study the results of other well-known libration point orbits, like the vertical Lyapunov orbits [33], as well as other non-libration point orbits that directly orbit the asteroid, such as the ones studied in [31] or [32].

2. *Performing a grid-search simulation close to the initial conditions found.*

Although the subject of this thesis was related to studying ejecta particles captured into periodic orbits, it could be beneficial to perform an extensive, brute-force search with ranges close to the initial conditions that were found to cause temporary periodic orbit capture. While the trajectories resulting from these simulations will likely not lead to periodic orbits, they may provide insight into temporary capture into chaotic motion about the asteroid, leading from the conclusions reached in this thesis. A good starting point, to limit the computational effort, could be to simulate the ranges of ejection velocities found in

---

<sup>6</sup>The escape velocity is computed as  $v_{esc} = \sqrt{2\mu/R_a}$ , where  $\mu$  is the asteroid’s gravitational parameter and  $R_a$  is the asteroid’s radius [30].

this thesis, from the planned impact location, at ejection angles between  $35^\circ$  and  $50^\circ$  with respect to the surface normal. The same analysis could then be followed by changing the ejection site to the locations identified as leading to the greatest and smallest number of capture particles in this thesis. If one were capable of using a computer with very powerful computational capabilities, the ideal choice would be to run these simulations for the entire surface of the asteroid.

### 3. Simulate the ejection conditions that cause temporary orbit capture in a high-fidelity model.

In order to understand the extent to which the trajectories and results obtained in this thesis hold in the real dynamics of the system, we propose as a future addition to this work to simulate the initial conditions that cause temporary periodic orbit capture in a high-fidelity model. These simulations could be tied with the previous recommendation, in the sense that one could simulate ranges of initial conditions for the ejection velocities, angles, and locations close to the initial conditions found in this thesis, but in a high-fidelity and realistic model, that should include a high-fidelity model of the asteroid's gravity. Recommendations for the gravity model include using a spherical harmonics expansion that considers the non-oblate terms of the asteroid, using a Constant Density Ellipsoid model (CDE) with elliptic integrals [34], a Constant Density Polyhedron [35], and mascon approach [36, 37]. Note, however, that the inclusion of a complex gravity model and the spin of the asteroid in the Hill frame<sup>7</sup> would generally make the problem twice time dependent and significantly increase computation time. Moreover, a gravity model that varies with longitude would lead to ejections locations in the local longitude and latitude of the asteroid (as opposed to the defined right ascension and declination), where the asteroid spins at a period of 7.6 h [38, 39].

## III.2.2. Other Applications

During the development of this thesis, arising from fruitful discussions and results obtained, an idea for another application using the methodology and process implemented in this work was identified. Here we present preliminary results that stem from that application, which could be pursued in the future, despite not being directly tied to the topic of this thesis.

### Landing Trajectories from Periodic Orbits

If we follow a reverse approach to the one presented in this thesis, and integrate the unstable manifolds of the periodic orbits forward in time (as opposed to integrating the stable manifolds backwards in time) we can obtain landing trajectories from periodic orbits, which could be followed by spacecraft or landers. Other works have previously considered landing trajectories to small bodies [40–42]. In this short preliminary analysis we compute landing trajectories from periodic orbits of family *a* and the terminator family for asteroid Ryugu. However, this approach could be applied to any asteroid and any unstable periodic orbit. We re-state the equation for non-dimensional SRP acceleration

$$\beta = \frac{(1 + C_R)P_0}{m/A \mu^{1/3} \mu_S^{2/3}} \quad (\text{III.1})$$

where  $C_R$  is the reflectivity coefficient or albedo,  $P_0 \approx 1.02 \times 10^{17} \text{ kg m s}^{-2}$  is the solar pressure constant,  $m/A$  is the mass-to-area ratio, and  $\mu_S$  is the gravitational parameter of the Sun.

We take SRP acceleration values close to those experienced by spacecraft and landers about the asteroid, as well as an SRP acceleration value appropriate for a solar-sail [19]. To represent spacecraft as Hayabusa2 [31] and OSIRIS-REx [43] we take the values  $\beta = \{20, 40, 50\}$ , and to represent a solar-sail like that launched by JAXA's IKAROS mission [44], we take  $\beta = \{1000\}$ . For completeness we consider also  $\beta = \{75, 100, 200\}$ .

The main outcome investigated in this preliminary analysis refers to the touchdown or impact conditions of the spacecrafts when landing on the asteroid. We focus particularly on the impact angle,  $\sigma_{imp}$ , the time of flight,  $t_{flight}$ , between the departure from the periodic orbit and arrival at the asteroid, and the impact velocity,  $v_{imp}$ . The impact angle is measured with respect to the surface normal and ranges from  $\sigma_{imp} = 90^\circ$ , which corresponds to an impact angle tangential to the local surface, to  $\sigma_{imp} = 180^\circ$ , which corresponds to a vertical impact. We aim to minimize this angle so as to arrive as tangentially as possible to the asteroid surface, i.e., as close as possible to  $\sigma_{imp} = 90^\circ$ , as well as minimizing the impact velocity and the time of flight.

<sup>7</sup>The Hill frame rotates with the Sun-asteroid system, its *x*-axis pointing from the Sun to the asteroid, is centered on the asteroid, and whose *z*-axis points in the direction of the asteroid's orbit angular momentum vector

Taking into account the fact that the time of flight might pose an important constraint to the mission - a transfer time between the orbit and the asteroid surface of six months is not conceivable - we first present the results as a function of the time of flight. Figure III.1 shows the times of flight as a function of the impact angle for the different values of SRP acceleration for the  $a$  and terminator families. We see that lower values of  $\beta$  lead to very long times of flight, above 70 days for  $\beta = 20$ . The vertical lines seen for the terminator family in Figure III.1b refer to orbits that are very close to the equilibrium point; due to their small size and proximity to the  $L_2$  point, their manifolds lead to the asteroid in an almost straight line and considerably faster than the other manifold trajectories for the same  $\beta$  value and same family. Figure III.2 shows an example of such a trajectory of the terminator family, which represents the landing trajectory with the smallest time of flight for  $\beta = 40$  in Figure III.1b ( $\approx 3$  days). While this type of trajectory decreases the time of flight significantly, it forces a near vertical landing, which may not be desirable due to bouncing dynamics on the surface of the asteroid. However, it is the approximately horizontal "lines" in Figure III.1b, which contain most of the landing trajectories of the terminator family, that give us an idea of the average time of flight for that SRP acceleration. For each  $\beta$ , the values that are significantly larger than these times refer to trajectories that orbit the asteroid a few times before landing. An example of such a trajectory is shown in Figure III.3, which represent the trajectory with the largest time of flight for  $\beta = 100$  in Figure III.1b (over 100 days).

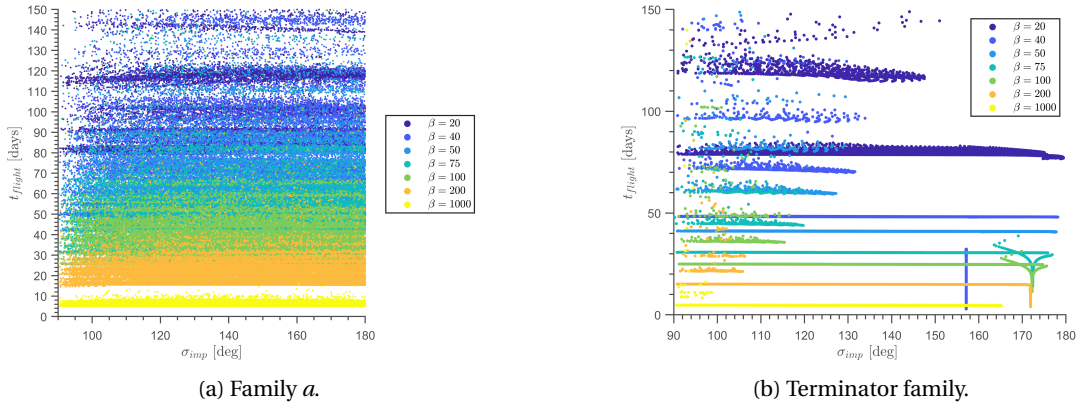


Figure III.1: Times of flight for the landing trajectories following the unstable manifolds of the  $a$  and terminator families.

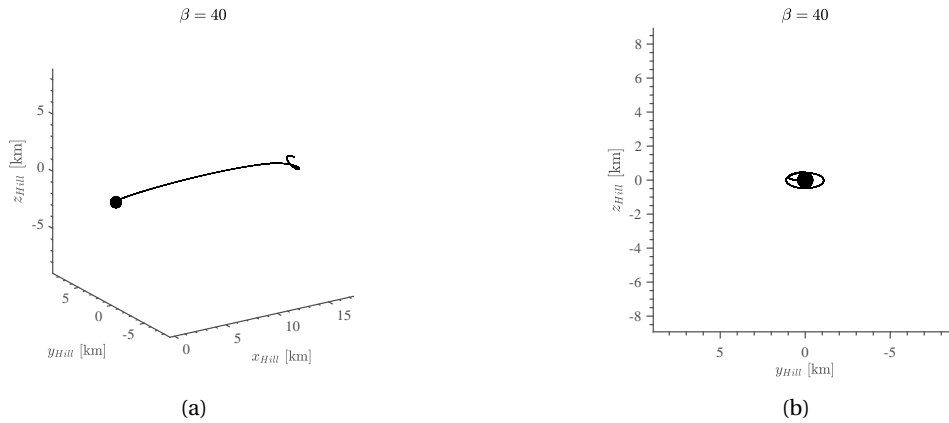


Figure III.2: Example of a landing trajectory for a terminator orbit that is very close to the  $L_2$  point.

In order to take into account general mission constraints, we limit the time of flight of the results to 30 days, which is by itself already a large value, and analyze the impact velocities and impact angles. Figure III.4 presents the impact velocities and impact angles for both families, taking into account the time of flight constraint. We see that for family  $a$  (Figures III.4a and III.4c) no trajectories for  $\beta$  values representative of spacecraft like Hayabusa2 or OSIRIS-REx ( $\beta = [20, 50]$ ) remain after the time of flight constraint. Although the terminator family still shows possible landing trajectories for these values of  $\beta$  after the time constraint (see

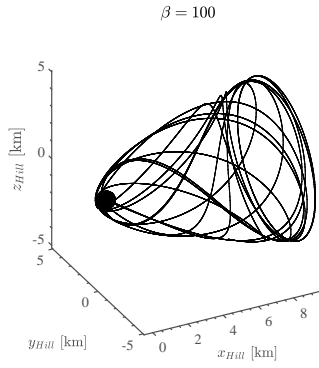
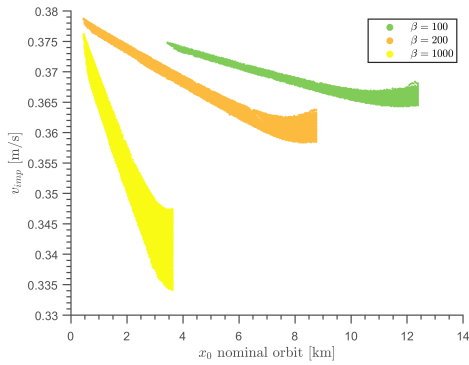


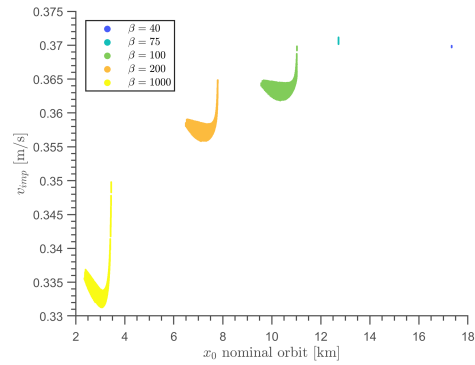
Figure III.3: Example of a landing trajectory from a terminator orbit that orbits the asteroid several times before landing.

Figures III.4b and III.4d), these trajectories correspond to the aforementioned near vertical impacts, which also have larger impact velocities that could cause the spacecraft or lander to bounce on the asteroid and escape.

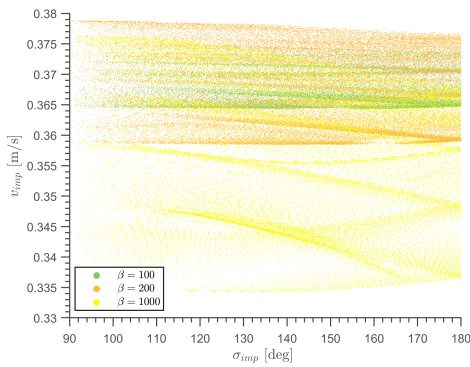
As shown in Figure III.4, the variation in impact velocities is very small for both families. Nonetheless, we note that for the terminator family the largest velocities always occur for the trajectories closest to vertical impacts, while the smallest velocities occur for impacts with  $\sigma_{imp} = 140^\circ$ , i.e.,  $50^\circ$  with the surface (see Figure III.4d). However, as shown in Figure III.4c, family *a* does not show a relation between impact angle and impact velocity, although we see that the minimum impact velocities decreases with the increase in  $\beta$ .



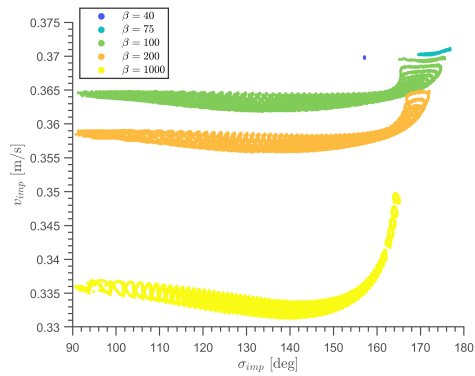
(a) Family *a*.



(b) Terminator family.



(c) Family *a*.



(d) Terminator family.

Figure III.4: Impact velocities and angles for the *a* and terminator families.

Figures III.4a and III.4b also show how the increase in  $\beta$  causes the nominal orbits to approach the asteroid, as detailed in the body of this thesis. Depending on the mission design constraints and objectives this could either be an advantage or disadvantage, and should be considered in the decision process when designing a

landing trajectory.

As seen from Figures III.4c and III.4d, the larger values of  $\beta$  all allow for near tangential impact conditions below the 30 days time of flight constraint. The most promising results are obtained for SRP acceleration values equivalent to those of a solar-sail, which allow for (virtually) fuel-free landing trajectories within a five-day period (see Figure III.1) and near minimum impact velocities for tangential landing conditions (see Figures III.4c and III.4d).

Comparing the  $a$  and terminator families, the advantages of using a terminator orbit relate to the possibility of directly reaching high local latitudes on the asteroid's surface, its flight heritage - as the OSIRIS-REx mission is currently orbiting asteroid Bennu in a terminator orbit [43], and its robustness against gravity model uncertainties [45, 46]. Figure III.5 shows landing locations on the asteroid's surface as a function of the impact angle from the terminator family. Considering the fact that we aim to minimize the impact angle and achieve a tangential impact trajectory, Figure III.5 shows we can still reach latitudes of up to  $60^\circ$ , whereas for family  $a$  we can only land on the equator of the asteroid.

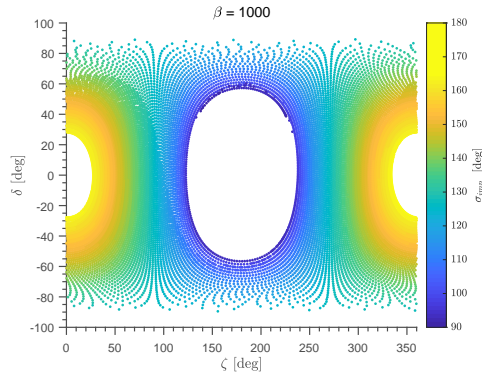


Figure III.5: Impact locations for terminator family with  $\beta = 1000$  as a function of the impact angle.

Finally, a few examples of landing trajectories that intersect the asteroid almost tangentially are presented for both families in Figures III.6 and III.7.

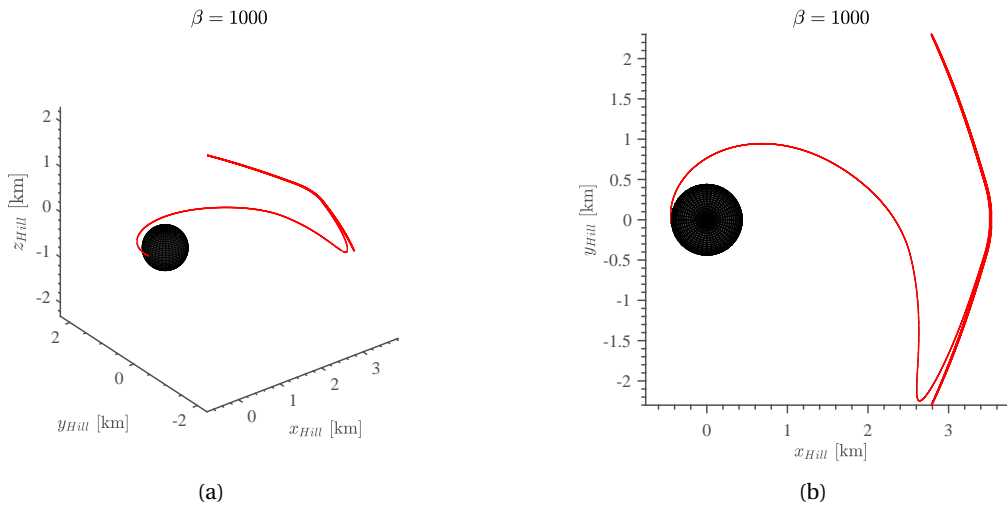


Figure III.6: Landing trajectory from family  $a$  orbit, with the following conditions:  $t_{flight} = 5.00$  days,  $\sigma_{imp} = 91.617^\circ$ ,  $v_{imp} = 0.3353$  m/s.

Although the results here presented comprise a short and preliminary analysis, we show that the method employed in this thesis can be used to successfully obtain landing trajectories for spacecraft or landers to small bodies. We note that landing trajectories for solar-sails look particularly promising, due to the shorter times of flight they allow. We also should not immediately discard the landing possibilities for spacecraft with lower SRP acceleration values when using this method. Although the times of flight presented here may be too long or, when selecting those with short times of flight, the impact angle too vertical, further analysis

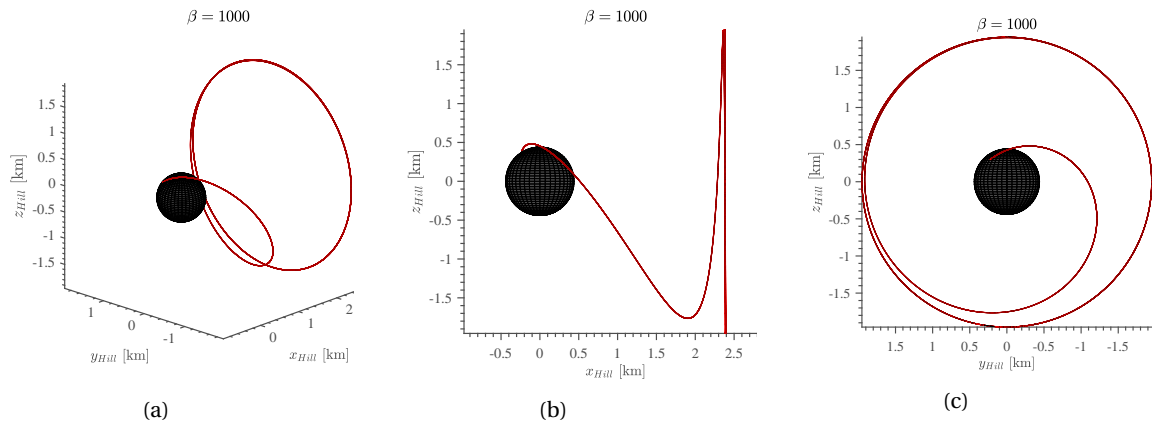


Figure III.7: Landing trajectory from terminator orbit, with the following conditions:  $t_{flight} = 4.75$  days,  $\sigma_{imp} = 90.63^\circ$ ,  $v_{imp} = 0.3358$  m/s.

should take place. Firstly, we are assuming that a vertical impact would likely lead to a bouncing-enabled escape motion. Although this assumption may seem rational at a first glance, it would be necessary to simulate possible bouncing motions in these scenarios to make an accurate assessment. Secondly, we are assuming the spacecraft or lander would depart the orbit asymptotically. In reality, a small delta-V would likely be used to depart from the orbit. This would decrease the time of flight significantly, as it would be translated in a larger perturbation value when calculating the unstable manifolds of the orbit [47]. Lastly, a solar-sail could be used merely as mother-spacecraft, deploying a lander with a different area-to-mass value (and thus different SRP acceleration), which could forbid its escape from the system if the ZVCs of the motion described by the lander were to close on the equilibrium point.



# Bibliography

- [1] G. W. Kronk, *Cometography, Vol. 1*. Cambridge Univ. Press., 1999.
- [2] H. Scholl and L. D. Schmadel, “Discovery Circumstances of the First Near-Earth Asteroid (433) Eros,” *Acta Historica Astronomiae*, vol. 15, pp. 210–220, 2002.
- [3] N. R. Augustine, W. M. Austin, C. Chyba, C. F. Kennel, B. I. Bejmuk, E. F. Crawley, L. L. Lyles, L. Chiao, J. Greason, and S. K. Ride, “Seeking a Human Spaceflight Program Worthy of a Great Nation,” tech. rep., Review of U.S. Human Spaceflight Plans Committee, 2009.
- [4] D. G. Korycansky and E. Asphaug, “Simulations of Impact Ejecta and Regolith Accumulation on Asteroid Eros,” *Icarus*, vol. 171, no. 1, pp. 110–119, 2004.
- [5] D. J. Scheeres, D. D. Durda, and P. E. Geissler, “The Fate of Asteroid Ejecta,” *Asteroids III*, pp. 527–544, 2002.
- [6] L. Prockter, S. Murchie, A. Cheng, A. Krimigis, R. Farquhar, A. Santo, and J. Trombka, “The NEAR Shoemaker Mission to Asteroid 433 Eros,” *Acta Astronautica*, vol. 51, no. 1-9, pp. 491–500, 2002.
- [7] J. Veverka, P. C. Thomas, M. Robinson, S. Murchie, C. Chapman, M. Bell, A. Harch, W. J. Merline, J. F. Bell, B. Bussey, B. Carcich, A. Cheng, B. Clark, D. Domingue, D. Dunham, R. Farquhar, M. J. Gaffey, E. Hawkins, N. Izenberg, J. Joseph, R. Kirk, H. Li, P. Lucey, M. Malin, L. McFadden, J. K. Miller, W. M. Owen, C. Peterson, L. Prockter, J. Warren, D. Wellnitz, B. G. Williams, and D. K. Yeomans, “Imaging of Small-Scale Features on 433 Eros from NEAR: Evidence for a Complex Regolith,” *Science*, vol. 292, pp. 484 LP – 488, apr 2001.
- [8] H. Yano, T. Kubota, H. Miyamoto, T. Okada, D. Scheeres, Y. Takagi, K. Yoshida, M. Abe, S. Abe, A. Fujiwara, S. Hasegawa, T. Hashimoto, M. Ishiguro, M. Kato, J. Kawaguchi, T. Mukai, J. Saito, S. Sasaki, and M. Yoshikawa, “Touchdown of the Hayabusa Spacecraft at the Muses Sea on Itokawa,” *Science*, vol. 312, no. 5778, pp. 1350–1354, 2006.
- [9] A. Fujiwara, J. Kawaguchi, D. K. Yeomans, M. Abe, T. Mukai, T. Okada, J. Saito, H. Yano, M. Yoshikawa, D. J. Scheeres, A. F. Cheng, H. Demura, R. W. Gaskell, N. Hirata, H. Ikeda, T. Kominato, H. Miyamoto, A. M. Nakamura, R. Nakamura, S. Sasaki, and K. Uesugi, “The Rubble-Pile Asteroid Itokawa as Observed by Hayabusa,” *Science*, vol. 312, no. June, pp. 1330–1335, 2006.
- [10] J. Saito, H. Miyamoto, R. Nakamura, M. Ishiguro, T. Michikami, A. M. Nakamura, H. Demura, S. Sasaki, N. Hirata, C. Honda, A. Yamamoto, Y. Yokota, T. Fuse, F. Yoshida, D. J. Tholen, R. W. Gaskell, T. Hashimoto, T. Kubota, Y. Higuchi, T. Nakamura, P. Smith, K. Hiraoka, T. Honda, S. Kobayashi, M. Furuya, N. Matsumoto, E. Nemoto, A. Yukishita, K. Kitazato, B. Dermawan, A. Sogame, J. Terazono, C. Shinohara, and H. Akiyama, “Detailed Images of Asteroid 25143 Itokawa from Hayabusa,” *Science*, vol. 312, pp. 1341 LP – 1344, jun 2006.
- [11] M. F. A. Hearn, M. J. S. Belton, W. A. Delamere, J. Kissel, K. P. Klaasen, L. A. Mcfadden, H. J. Melosh, P. H. Schultz, J. M. Sunshine, P. C. Thomas, J. Veverka, D. K. Yeomans, W. Baca, I. Busko, C. J. Crockett, S. M. Collins, M. Desnoyer, C. A. Eberhardy, C. M. Ernst, L. Feaga, O. Groussin, D. Hampton, S. I. Ipatov, J. Li, D. Lindler, C. M. Lisse, W. M. O. Jr, J. E. Richardson, D. D. Wellnitz, and R. L. White, “Deep Impact: Excavating Comet Tempel 1,” *Science*, vol. 310, p. 258, 2005.
- [12] S. Wissler, J. Rocca, and D. Kubitschek, “Deep Impact Comet Encounter: Design, Development and Operations of the Big Event at Tempel 1,” in *Proceedings of the Space System Engineering Conference*, (Pasadena, California), pp. 1–20, 2005.
- [13] Y. Tsuda, M. Yoshikawa, M. Abe, H. Minamino, and S. Nakazawa, “System Design of the Hayabusa 2 - Asteroid Sample Return Mission to 1999 JU3,” *Acta Astronautica*, vol. 91, pp. 356–362, 2013.
- [14] T. Saiki, H. Imamura, M. Arakawa, K. Wada, Y. Takagi, M. Hayakawa, K. Shirai, H. Yano, and C. Okamoto, “The Small Carry-on Impactor ( SCI ) and the Hayabusa2,” *Space Sci Rev*, pp. 165–186, 2017.

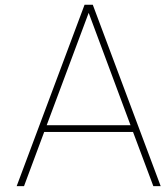
- [15] B. Hapke, "Space Weathering from Mercury to the Asteroid Belt," *Geology*, vol. 106, pp. 39–73, 2001.
- [16] K. Berry, B. Sutter, A. May, K. Williams, B. W. Barbee, M. Beckman, and B. Williams, "OSIRIS-REx Touch-And-Go (TAG) Mission Design and Analysis," in *36th Annual AAS Guidance and Control Conference*, (Breckenridge, Colorado), pp. 0–12, 2013.
- [17] A. Galvez, I. Carnelli, P. Michel, A. F. Cheng, C. Reed, S. Ulamec, J. Biele, P. A. Abell, and P. Landis, "AIDA: The Asteroid Impact & Deflection Assessment Mission," in *European and Planetary Science 2013, Congress Abstracts*, vol. 8, p. Abstract 1043, 2013.
- [18] D. J. Scheeres, *Orbital Motion in Strongly Perturbed Environments - Applications to Asteroid, Comet and Planetary Satellite Orbiters*. Springer-Verlag Berlin Heidelberg, 2012.
- [19] C. McInnes, *Solar Sailing: Technology, Dynamics and Mission Applications*. Springer-Verlag Berlin Heidelberg, 1999.
- [20] K. Richter and H. U. Keller, "On the Stability of Dust Particle Orbits around Cometary Nuclei," 1995.
- [21] D. J. Scheeres and F. Marzari, "Temporary Orbital Capture of Ejecta from Comets and Asteroids: Application to the Deep Impact Experiment," *Astronomy and Astrophysics*, vol. 756, pp. 747–756, 2000.
- [22] D. J. Scheeres, S. J. Ostro, R. S. Hudson, and R. A. Werner, "Orbits close to Asteroid 4769 Castalia," *Icarus*, vol. 121, no. 1, pp. 67–87, 1996.
- [23] K. R. Housen and K. A. Holsapple, "Ejecta from Impact Craters," *Icarus*, vol. 211, pp. 856–875, 2011.
- [24] K. A. Holsapple and K. R. Housen, "A Crater and its Ejecta: An Interpretation of Deep Impact," *Icarus*, vol. 187, pp. 345–356, 2007.
- [25] J. E. Richardson and H. J. Melosh, "Impact Cratering Theory and Modeling for the Deep Impact Mission: From Mission Planning to Data Analysis," *Space Science Reviews*, vol. 117, pp. 241–267, 2006.
- [26] G. W. Hill, "Researches in the Lunar Theory," *American Journal of Mathematics*, vol. 1, no. 4, pp. 5–26, 1878.
- [27] M. Henon, "Numerical Exploration of the Restricted Problem. V. Hill's Case: Periodic Orbits and Their Stability," *Astronomy and Astrophysics*, vol. 1, no. 2, pp. 223–238, 1969.
- [28] E. Morrow, D. J. Scheeres, and D. Lubin, "Solar Sail Orbit Operations at Asteroids," *Journal of Spacecraft and Rockets*, vol. 38, no. 2, pp. 279–286, 2001.
- [29] D. García Yarnoz and C. R. McInnes, "On the a and g Families of Orbits in the Hill Problem with Solar Radiation Pressure and their Application to Asteroid Orbiters," *Celestial Mechanics & Dynamical Astronomy*, vol. 121, pp. 365–384, 2015.
- [30] A. D. Vallado, *Fundamentals of Astrodynamics and Applications*. Microcosm Press/Springer, 1997.
- [31] M. Giancotti, S. Campagnola, Y. Tsuda, and J. Kawaguchi, "Families of Periodic Orbits in Hill's Problem with Solar Radiation Pressure: Application to Hayabusa 2," *Celestial Mechanics and Dynamical Astronomy*, vol. 120, no. 3, pp. 269–286, 2014.
- [32] S. B. Broschart, G. Lantoine, and D. J. Grebow, "Quasi-Terminator Orbits near Primitive Bodies," *Celestial Mechanics and Dynamical Astronomy*, vol. 120, no. 2, pp. 195–215, 2014.
- [33] K. Howell, "Families of Orbits in the Vicinity of the Collinear Libration Points," in *AAS/AIAA Astrodynamics Specialist Conference and Exhibit*, p. 4465, 1998.
- [34] D. J. Scheeres, "Dynamics about Uniformly Rotating Triaxial Ellipsoids: Applications to Asteroids," *Icarus*, vol. 110, pp. 225–238, 1994.
- [35] R. A. Werner, "Spherical Harmonic Coefficients for the Potential of a Constant-Density Polyhedron," *Computers and Geosciences*, vol. 23, no. 10, pp. 1071–1077, 1997.

- [36] A. Rossi, F. Marzari, and P. Farinella, “Orbital Evolution around Irregular Bodies,” *Earth Planets Space*, vol. 51, pp. 1173–1180, 1999.
- [37] S. Soldini, S. Takanao, and T. Yuichi, “SPH-Mascon Gravity Field for Ejecta Particles Dynamics: an Analytic Construction of Ryugu Asteroid,” *Planetary and Space Science*, no. Under review, 2019.
- [38] S. Soldini and Y. Tsuda, “Assessing the Hazard Posed by Ryugu Ejecta Dynamics on Hayabusa2 Spacecraft,” *26th International Symposium of Space Flight Dynamics*, pp. 1–11, 2017.
- [39] T. G. Mueller, J. Durech, S. Hasegawa, M. Abe, K. Kawakami, T. Kasuga, D. Kinoshita, D. Kuroda, S. Urakawa, S. Okumura, Y. Sarugaku, S. Miyasaka, Y. Takagi, P. R. Weissman, Y. J. Choi, S. Larson, K. Yanagisawa, and S. Nagayama, “Thermo-Physical Properties of 162173 (1999 JU3), a Potential Flyby and Rendezvous Target for Interplanetary Missions,” *Astronomy and Astrophysics*, vol. 525, no. A145, pp. 1–6, 2011.
- [40] S. Tardivel and D. J. Scheeres, “Ballistic Deployment of Science Packages on Binary Asteroids,” *Journal of Guidance, Control, and Dynamics*, vol. 36, no. 3, pp. 700–709, 2013.
- [41] S. Tardivel, P. Michel, and D. J. Scheeres, “Deployment of a Lander on the Binary Asteroid (175706) 1996 FG3, Potential Target of the European MarcoPolo-R Sample Return Mission,” *Acta Astronautica*, vol. 89, pp. 60–70, 2013.
- [42] A. Basiana Farrés, S. Soldini, and Y. Tsuda, “JAXA’s Trojan Asteroids Mission: Trajectory Design of the Solar Power Sail and its Lander,” *4th International Symposium on Solar Sailing*, pp. 1–7, 2017.
- [43] D. J. Scheeres and A. J. Rosengren, “Design , Dynamics and Stability of the OSIRIS-REx Sun-Terminator Orbits,” in *Advances in the Astronautical Sciences*, no. 148, pp. 3263–3282, 2013.
- [44] Y. Tsuda, O. Mori, R. Funase, H. Sawada, T. Yamamoto, T. Saiki, T. Endo, and J. Kawaguchi, “Flight Status of IKAROS Deep Space Solar Sail Demonstrator,” *Acta Astronautica*, vol. 69, no. 9-10, pp. 833–840, 2011.
- [45] D. J. Scheeres, B. G. Williams, and J. K. Miller, “Evaluation of the Dynamic Environment of an Asteroid: Applications to 433 Eros,” *Advances in the Astronautical Sciences*, vol. 102 II, no. 3, pp. 835–848, 1999.
- [46] S. B. Broschart and B. F. Villac, “Identification of Non-Chaotic Terminator Orbits near 6489 Golevka,” *Advances in the Astronautical Sciences*, vol. 134, no. February 2009, pp. 861–880, 2009.
- [47] W. S. Koon, M. W. Lo, J. E. Marsden, and S. D. Ross, *Dynamical Systems, the Three-Body Problem and Space Mission Design*. 2011.
- [48] M. Giancotti, *Stable Orbits in the Proximity of an Asteroid: Solutions for the Hayabusa 2 Mission*. PhD thesis, Sapienza – University of Rome, 2014.
- [49] L. F. Shampine and M. W. Reichelt, “The MATLAB ODE Suite,” *SIAM Journal on Scientific Computing*, vol. 18, no. 1, pp. 1–22, 1997.
- [50] J. Han and C. Moraga, “The Influence of the Sigmoid Function Parameters on the Speed of Backpropagation Learning,” in *From Natural to Artificial Neural Computation* (J. Mira and F. Sandoval, eds.), pp. 195–201, Springer Berlin Heidelberg, 1995.
- [51] X. Yang, J. Liu, Y. Yang, Q. Qing, and G. Wen, “An Efficient Topology Description Function Method Based on Modified Sigmoid Function,” *Mathematical Problems in Engineering*, vol. 2018, pp. 1–12, 2018.
- [52] K. C. Howell, “Three-Dimensional, Periodic, ‘Halo’ Orbits,” *Celestial Mechanics*, vol. 32, pp. 53–71, 1984.
- [53] B. D. Tapley, B. E. Schutz, and G. H. Born, *Statistical Orbit Determination Theory*. Elsevier Academic Press, 2004.
- [54] J. S. Parker, K. E. Davis, and G. H. Born, “Chaining Periodic Three-Body Orbits in the Earth-Moon System,” *Acta Astronautica*, vol. 67, no. 5-6, pp. 623–638, 2010.



# **Appendices**





# Verification and Validation

In order to verify and validate the models developed for the work presented in this thesis, a series of tests were performed. This chapter explores and presents said tests together with the results.

The model developed for this work can be seen as a combination of three sub-models:

- Augmented Hill Problem (AHP) model
- Eclipse model
- Spherical harmonics model with  $J_2$  and  $J_4$

The AHP (sub)-model serves as the basis to the entire model in the sense that the other two can only be used in combination with the AHP (sub)-model, or, of course, by using all three together. For simplification we drop the term "sub-model" and refer to each as a "model". Within these models, three main operations are identified:

1. State vector integration
2. State Transition Matrix (STM) integration
3. Differential correction

A remark should be made as to the fact that the computation of the invariant manifolds is not regarded as a "main operation" of the model. The reason for this relays with the fact that said computation is performed using the operations (1) to (3). That is, we first obtain a periodic orbit using the differential corrector, integrate its state vector and STM for one period, then add a perturbation along the stable eigenvectors for several points along the orbit, and finally integrate its state vector backwards in time until it either intersects the asteroid, escapes the system, or the set time limit is reached. We can see that the only "new" operation mentioned in this set of actions is the perturbation along the stable eigenvectors of the orbit, and even that comes from the integration of STM along the orbit and then using MATLAB<sup>®</sup> functions to compute its eigenvectors. For this reason, it is deemed that the verification of the other main operations (1)-(3) serves to verify the computation of the invariant manifolds. For completeness, however, a qualitative verification is included in Figure A.1 regarding the magnitude of the perturbation used to compute the manifolds, to check that by integrating a stable manifold forwards in time from, for instance, the asteroid surface, we do indeed reach the periodic orbit and remain there for at least a period.

That being said, we can then assume that by verifying each of the main operations (1) to (3) within the three models, we will verify the model as a whole. We do this by testing each of the operations within the different models, going through each main operation at a time. Table A.1 shows a schematic representation of these tests, which consist, when possible, of two iterations. The first aims at expressing the numerical and mathematical correctness of the model, comparing the results with those predicted by the analytical models, while the second makes use of a more qualitative analysis, comparing the obtained plots or results with those from literature. This second iteration depends on the existence of relevant data from other sources, and as such is not always available.

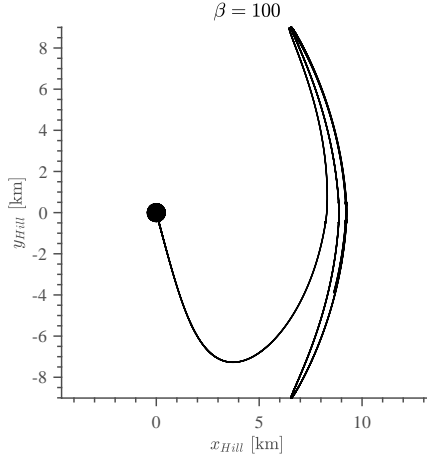


Figure A.1: A stable manifold trajectory from family *a* integrated forwards in time from the asteroid surface up to its period orbit.

Table A.1: The two testing iterations for the validation and verification of the model.

Operation	First iteration	Second iteration
1	Jacobi constant	Orbits in [28, 29]
2	Determinant of STM Unity eigenvalue pair	Stability diagrams in [27, 29]
3	Value of iterative correction Position error after one period	Initial conditions in [27, 48]

## A.1. State vector integration

**AHP model:** The operation (1) refers to the general integration and propagation of the state vectors through time, i.e., solving the initial value problem for the ordinary differential equations defined by the equations of motion, and sets the basis to the entire model.

The state vector is always integrated via MATLAB<sup>®</sup>'s *ode45* function (Ordinary Differential Equation, orders 4 and 5), which uses an adaptive step-size Runge-Kutta Dormand-Price integrator [49]. The relative and absolute error tolerances are both set to  $10^{-13}$ , close to the minimum allowed by the integrator. As mentioned during the body of this thesis, because the AHP model is time-invariant, it admits an energy integral, which is formally known as the Jacobi constant,  $C$ . In a perfect, analytical consideration, the value of  $C$  must remain constant for any trajectory within the AHP model [30]. Of course, due to the numerical error associated with the machine, this value will always vary by a very small amount; but it should remain very close to zero. By quantifying this variation we can assess whether the state vector is being accurately integrated and propagated and thus if the equations of motion and this section of the model are correctly implemented.

We first consider the AHP model and select three pairs of orbits, pertaining to three different orbit families, each pair consisting of an orbit without SRP and one with SRP. We also consider two non-periodic random trajectories, one with and one without SRP, for the purpose of completeness. For each of these trajectories we look at the maximum variation of the value of the Jacobi constant,  $\Delta C_{max}$ . Since the values of the initial position along the  $y$ -axis and initial velocity along the  $x$ -axis are always set to zero, they are excluded from Table A.2 for simplification.

From Table A.2, we see that the maximum variation of the Jacobi constant is indeed negligibly small, in the orders of  $10^{-12}$  to  $10^{-14}$ . Although a source could not be found that specifies the acceptable limits for these errors, an error 12 orders of magnitude smaller than the nominal value is deemed acceptable, and we thus confirm the correct integration and propagation of the state vector in the AHP model. The differences between the orders of magnitude of  $\Delta C_{max}$  for the different trajectories are tied with the number of state vector integrations, or time steps, that the algorithm takes. Because *ode45* uses a variable time-step, this number changes depending on how "demanding" the integration is, which leads, in the cases of more time-steps, to a higher accumulated numerical error. Other than this test, using initial conditions stated in [28, 31], orbits

Table A.2: Error associated with the maximum variation of the Jacobi constant for different trajectories in the AHP model. Initial conditions and period (or in the case of the random trajectories, integration time) are presented in non-dimensional units.

$\beta$	Family	$\Delta C_{max}$	$x_0$ [-]	$z_0$ [-]	$\dot{y}_0$ [-]	$\dot{z}_0$ [-]	$t$ [-]
0	$a$	$1.56319402 \times 10^{-13}$	0.32125800	0	2.08969372	0	3.56886117
100	$a$	$3.55271368 \times 10^{-13}$	0.07112700	0	3.63083747	0	0.17727777
0	$g'$	$1.03028697 \times 10^{-12}$	0.25546700	0	2.50181945	0	4.73721046
100	$g'$	$2.24531505 \times 10^{-12}$	0.06333400	0	4.18020864	0	0.18556618
0	terminator	$3.37507799 \times 10^{-14}$	0.30433087	0.34000788	1.48923206	0	2.97697355
100	terminator	$4.26325641 \times 10^{-14}$	0.08519857	0.04001235	1.39565598	0	0.18390886
0	-	$6.62225830 \times 10^{-12}$	0.1400	0	1.00	0.100	0.700
100	-	$6.37001563 \times 10^{-12}$	0.00800	0.0500	3.800	0	0.700

referenced in said sources were integrated and plotted, and found to qualitatively match the plots from those sources. An example of this can be seen in Figure A.2, where the initial conditions for an orbit about asteroid Vesta from [28] are integrated for the same period of time, 116 days, using the same point mass gravity of Vesta and SRP acceleration. Since both works use an AHP model for the dynamics of the system, we are able to qualitatively verify the matching between both.

Table A.3: Error associated with the maximum variation of the Jacobi constant for different trajectories in the AHP model with the  $J_2$  and  $J_4$  gravity perturbations. Initial conditions are presented in non-dimensional coordinates.

$\beta$	Family	$\Delta C_{max}^*$	$x_0$ [-]	$z_0$ [-]	$\dot{y}_0$ [-]	$\dot{z}_0$ [-]	$t$ [-]
0	$a$	$1.55431223 \times 10^{-13}$	0.32125800	0	2.08969372	0	3.56886291
100	$a$	$3.16191517 \times 10^{-13}$	0.07308700	0	3.47098014	0	0.17883415
0	$g'$	$5.22959453 \times 10^{-12}$	0.40585900	0	1.56742432	0	3.84512642
100	$g'$	$3.08375547 \times 10^{-12}$	0.0698400	0	3.65116038	0	0.18990892
0	terminator	$2.66453526 \times 10^{-14}$	0.48016178	0.23903830	0.99004071	0	3.05848156
100	terminator	$7.81597009 \times 10^{-14}$	0.04885286	0.06047993	2.81732643	0	0.14002169
0	-	$1.21502808 \times 10^{-12}$	0.00800	0.0500	3.800	0	0.1400
0	-	$2.54374299 \times 10^{-12}$	0.001600	0.0500	3.500	0	0.1400

**Gravity model:** We focus next on the gravity model with the  $J_2$  and  $J_4$  ( $C_{20}$  and  $C_{40}$  Stokes coefficients) gravity perturbations of the spherical harmonics potential. Because they do not depend on the spin of the asteroid, the problem remains time-invariant, although the expression for the Jacobi constant changes slightly since it must now include the new gravity potential with the  $J_2$  and  $J_4$  terms. Nonetheless, this means we can also test the integration and propagation of the state vector in this model by assessing the variation of the modified Jacobi constant,  $\Delta C_{max}^*$ . The error associated with this can be seen in Table A.3, where once again we select three pairs of periodic orbits and a pair of non-periodic trajectories, each pair with an orbit or trajectory with and without SRP. From Table A.3 we see that the values of  $\Delta C_{max}^*$  remain within acceptable limits, between  $10^{-12}$  and  $10^{-14}$ .

**Eclipse model:** When considering the eclipse effect, the constant energy integral of the system disappears. This occurs because the system is no longer time-invariant, as it depends on when and for how long it stays within the eclipse region. Of course, this constraint is only implicitly dependent on time, as it depends on the position of a particle at a time  $t$ . Nonetheless, when considering a periodic orbit, we can say that the variation of the Jacobi constant will also be periodic, as its energy level must be the same at  $t = nT, \forall n \in \mathbb{N}$ , or the orbit would not be periodic. Furthermore, while in the total eclipse or no eclipse regions, the Jacobi constant should not vary, since these regions are, by themselves, time-invariant. This means we can verify the integration of the state vector within the eclipse model by analyzing how the Jacobi constant varies over the course of a periodic orbit. Moreover, when considering the eclipse model but setting  $\beta = 0$ , the Jacobi constant should not vary, as in the cases shown above for the AHP and gravity models.

We use a cylindrical eclipse model and simulate a smooth transition between the non-eclipse and total eclipse regions by means of a sigmoid function [50,51], which acts as a smooth step function for the SRP taking

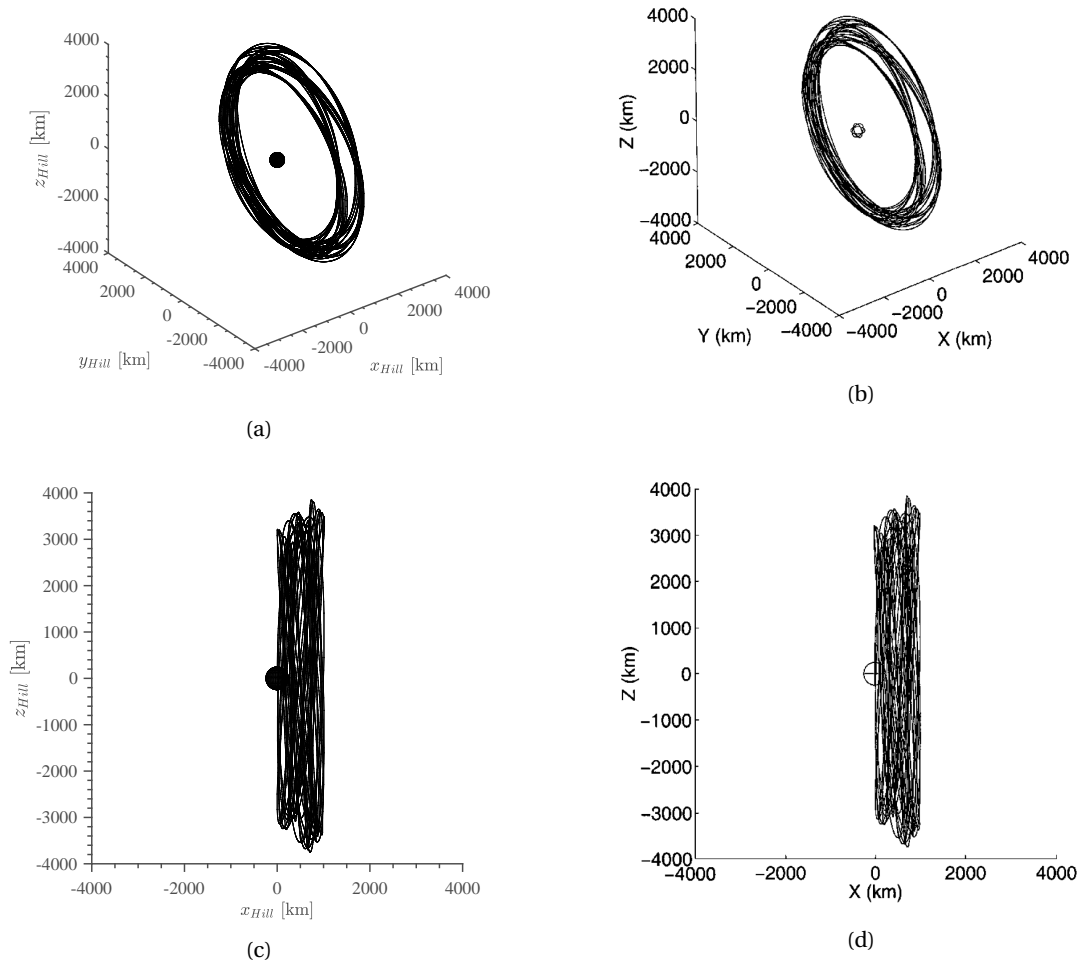


Figure A.2: o

$r_{aSRP} = 1.79546 \times 10^{-4}$  [m/s<sup>2</sup>]. Comparison between between orbit obtained in [28] (Figures A.2b and A.2d) and the model developed in this work (Figures A.2a and A.2c), for the same initial conditions, about asteroid Vesta. The SRP acceleration is  $\beta = 354.7336$  [-] or  $a_{SRP} = 1.79546 \times 10^{-4}$  [m/s<sup>2</sup>]. Courtesy of Figures A.2b and A.2d: [28].

its value from  $\beta$  to zero. We select two pairs of periodic orbits that pass through the eclipse region, each pair including one orbit with SRP and another without, to verify that the Jacobi constant varies periodically for the first case and remains constant for the second. Figures A.3 and A.4 show the variation of the Jacobi constant and the non-dimensional SRP acceleration  $\beta$  of two periodic orbits that pass through the eclipse region, for one and two periods. The nominal SRP acceleration considered when not in eclipse is  $\beta = 100$ . Figure A.3 shows these values for an orbit of the planar family  $a$ , also known as planar Lyapunov orbits, and Figure A.4 for an orbit of the planar family  $g'$ .

We verify the Jacobi constant does indeed vary periodically, where each of these transitions in value occur when a particle enters or exits the eclipse region and correspond to the respective variation of  $\beta$ . For each, the maximum error in the sections where the energy integral should be constant, i.e., when the particle is not transitioning between the eclipse and non-eclipse regions, is respectively  $1.78701498 \times 10^{-12}$  and  $7.94386778 \times 10^{-12}$  for families  $a$  and  $g'$ . Furthermore, we see that the errors between the Jacobi constant at  $t = 0$  and  $t = T$  are, respectively,  $6.97095652 \times 10^{-6}$  and  $1.04531352 \times 10^{-8}$ . While these values are larger than those shown before, they are expected due to the variations of the Jacobi constant over one orbit. Because these variations are significantly larger than the errors (up to 10 orders of magnitude), the computer is less capable of dealing with very high decimal point precision, and thus the errors are more likely to accumulate. Finally, Table A.4 shows the errors of the Jacobi constant in the eclipse model when setting  $\beta$  to zero.

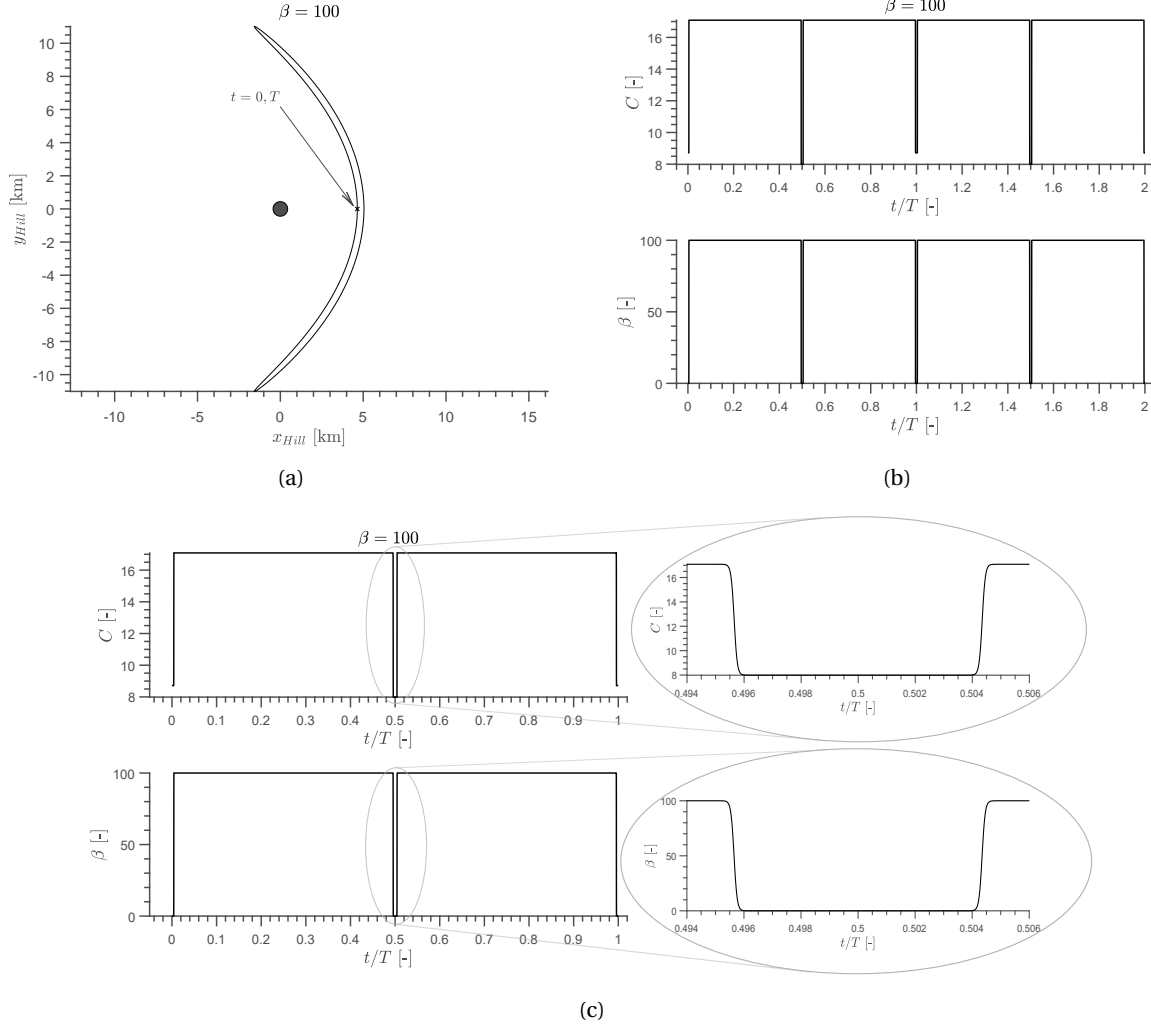


Figure A.3: Variation of the Jacobi constant and  $\beta$  in the AHP model eclipses for the orbit of family  $a$ , seen in (a). (b) two periods; (c) one period. The initial conditions are  $x_0 = 0.04195325$ ,  $\dot{y}_0 = 6.24192578$  [-] and  $y_0, z_0, \dot{x}_0, \dot{z}_0 = 0$ .

Table A.4: Error associated with the maximum variation of the Jacobi constant for different trajectories in the AHP model with eclipses. Initial conditions are presented in non-dimensional coordinates.

$\beta$	Family	$\Delta C_{max}$	$x_0$ [-]	$z_0$ [-]	$\dot{y}_0$ [-]	$\dot{z}_0$ [-]	$t$ [-]
0	$a$	$1.70086167 \times 10^{-13}$	0.30212800	0	2.21025245	0	3.64078384
0	$g'$	$1.03028696 \times 10^{-12}$	0.25546700	0	2.50181945	0	4.73721046

We can also perform a qualitative check of the eclipse model by plotting the shape of certain orbit families for high values of SRP. By doing so, we can then observe if they match the shape of those presented in the work of García Yarnoz et al. in [29], which studies the  $a$  and  $g'$  orbit families of the AHP for high values of SRP. Again, this does not substitute the actual numerical verification that was carried out; it serves only to support the conclusions drawn from said verification in a more visual and qualitative way. Figure A.5 shows this comparison for  $\beta = 30$ .

## A.2. STM integration

The main operation (2) of the model refers to the integration and propagation of the state transition matrix (STM),  $\Phi(t)$ , through time. In order to test its correct implementation we look at two features. The first is the

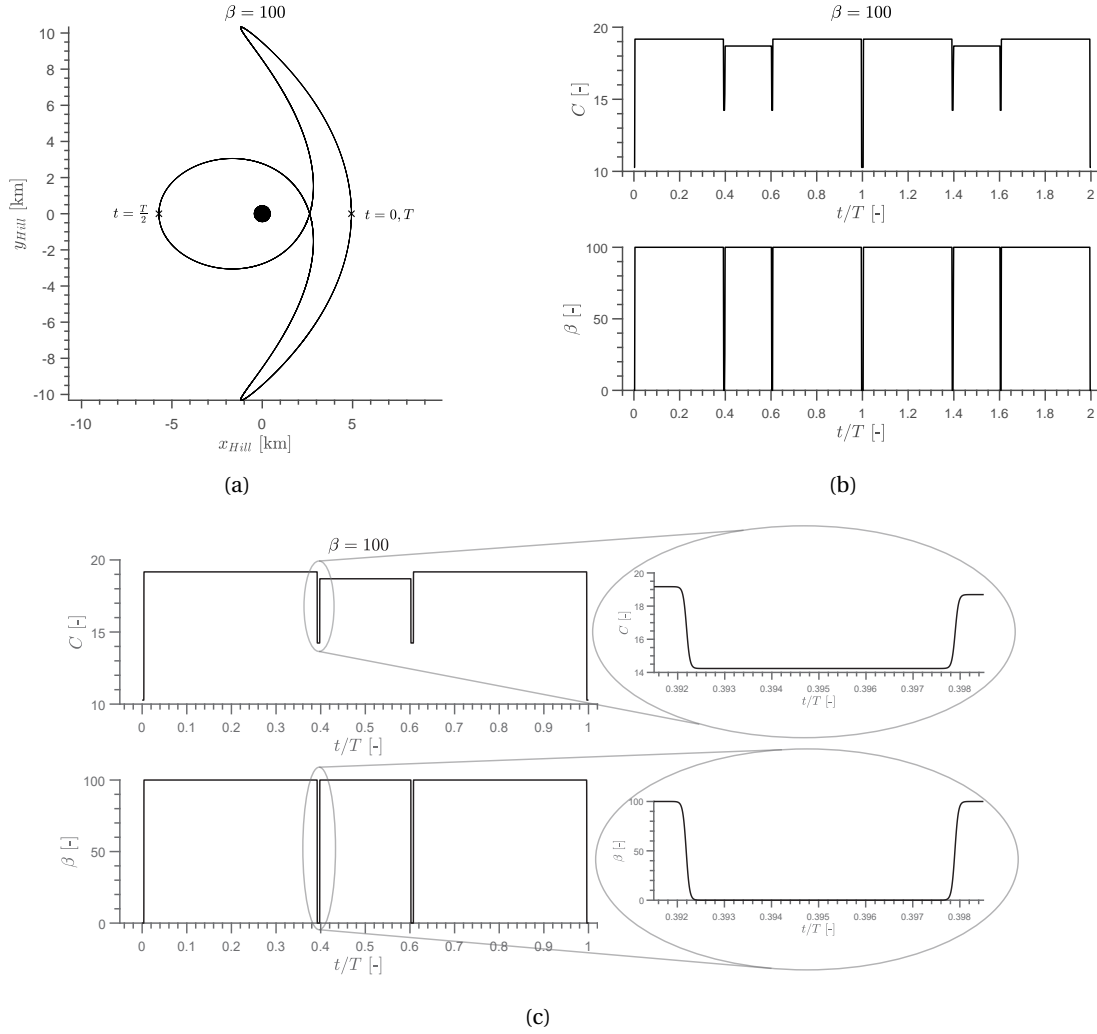


Figure A.4: Variation of the Jacobi constant and  $\beta$  in the AHP model with eclipses for an orbit of family  $g'$ , seen in (a). (b) two periods; (c) one period. The initial conditions are  $x_0 = 0.04458068$ ,  $y_0 = 5.88143855$  [-] and  $y_0, z_0, \dot{x}_0, \dot{z}_0 = 0$ .

fact that the symplectic nature of the STM means its determinant is always equal to one [18]. Secondly, when integrated over a period  $T$  of a periodic orbit (in which case the STM is known as the *Monodromy matrix*,  $\Phi_M$ ), at least a pair of the eigenvalues of  $\Phi(T)$  is always situated on the unit circle, i.e., their norm is always one [52]. Again, by verifying the variations to these nominal values – which, as before, should be negligibly small and caused by numerical error from the machine – we assess the correct implementation of this section of the model. It should be mentioned that the errors inherent to this integration and propagation are expected to be larger, due the larger number of operations necessary to calculate the STM at each point, and error associated with large matrix operations in MATLAB<sup>®</sup>. Since the STM is integrated using the Jacobian,  $J$ , of the equations of motion [53],  $F(\mathbf{X}) = [\dot{x}, \dot{y}, \dot{z}, \ddot{x}, \ddot{y}, \ddot{z}]^T$

$$J(t) = \frac{\partial F(\mathbf{X})}{\partial \mathbf{X}} \quad (\text{A.1})$$

it does not depend on the SRP parameter,  $\beta$ , and thus it is not affected by the inclusion of the eclipse. This means that, contrary to the case of the Jacobi constant, we can analyze the integration of the STM in the eclipse model too. We then test again the AHP and AHP with gravity perturbations models by analyzing the two aforementioned criteria in three pairs of periodic orbits.

The results of these tests can be seen in Tables A.5, A.6, and A.7, which show the errors associated with the integration and propagation of the state transition matrix for the AHP, gravity, and eclipse models, respectively. All the orbits in these tables have  $y_0, \dot{x}_0, \dot{z}_0 = 0$ , and as such these coordinates are not shown. As expected, these

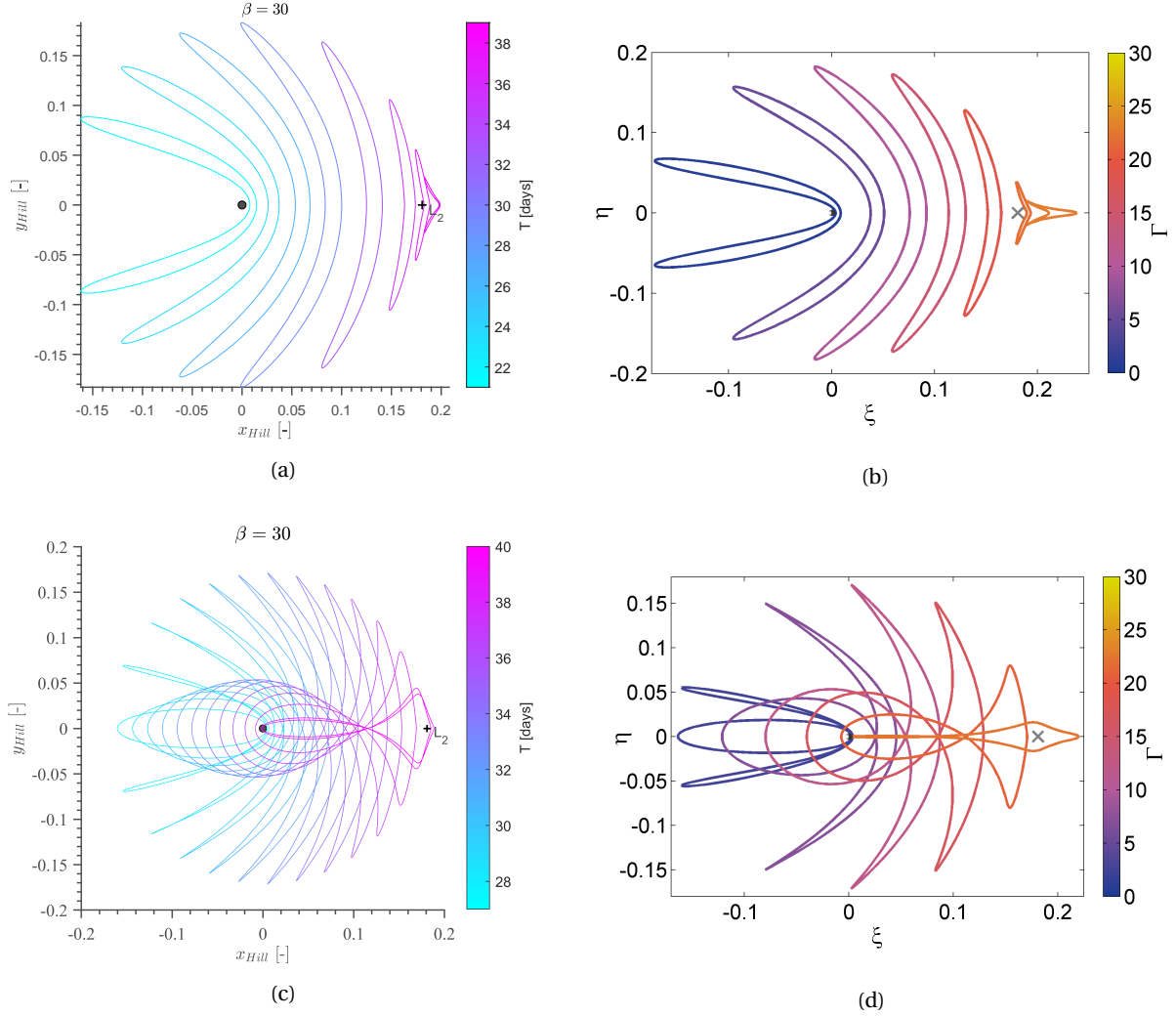


Figure A.5: Comparison between the geometry of families of periodic orbits  $a$  and  $g'$  in the AHP model with eclipses and from source [29] for  $\beta = 30$ . (a) Orbit family  $a$ ; (b) orbit family  $a$  from source [29]; (c) orbit family  $g'$  in eclipse model; (d) orbit family  $g'$  from source [29]. All plots are shown in non-dimensional units, where the plots from [29] use a different notation:  $\xi$  instead of  $x$ ;  $\eta$  instead of  $y$ ; and  $\Gamma$  instead of  $C$ , the Jacobi constant.

errors are in general larger than those found for  $\Delta C_{max}$  but are found to be within reasonable limits. The error associated to the unit eigenvalue pair is in general larger for more unstable orbits, given the machine must accommodate the values of large unstable eigenvalues with high decimal-point precision. Moreover, for the case of the eclipse model, we see that the error for the unit eigenvalue is particularly large. This is due to the fact that the unit eigenvalue pair is associated with the existence of the energy integral of motion [18]. When including the eclipse, the problem is no longer time-invariant and as such the energy integral varies proportionally to the time spent in eclipse; this causes a proportional variation in the unit eigenvalue pair. Nonetheless, this does not affect the symplectic nature of the STM, and we can see that the error associated with the determinant of  $\Phi_M$  is always smaller than  $10^{-7}$ , a value which in fact is smaller than that deemed acceptable in [32]. Finally, we see that the rows for  $\beta = 0$  of families  $a$  and  $g'$  and the terminator orbits in Tables A.5 and A.7 are in fact identical between the AHP and eclipse models. We purposely select the same initial conditions for both models and since the terminator orbits never fall in the eclipse region, we verify that the eclipse model behaves correctly and does not alter the dynamics of the system when either the SRP is set to zero, or when a particle does not enter the eclipse region.

For the AHP model we present also a qualitative comparison of the stability of families  $a$ ,  $g'$ , and  $f$ . Family  $f$  corresponds to the distant retrograde orbits presented in [27], and although it is not part of the analysis undertaken in this work, it is here presented for the purposes of verification. A more thorough analysis of

Table A.5: Error associated with the integration and propagation of the state transition matrix for different trajectories in the AHP model. Initial conditions are presented in non-dimensional coordinates, and  $z_0$  is zero for all orbits except for the terminator family, where  $z_0 = 0.19962821$  for  $\beta = 0$  and  $z_0 = 0.03303122$  for  $\beta = 100$ .

$\beta$	Family	$1 - \det(\Phi_M)$	$1 -  \lambda_i $	$x_0 [-]$	$\dot{y}_0 [-]$	$t [-]$
0	<i>a</i>	$-1.30707001 \times 10^{-10}$	$3.44643164 \times 10^{-5}$	0.38036000	1.74472173	3.39128018
100	<i>a</i>	$4.89876061 \times 10^{-9}$	$2.21164586 \times 10^{-6}$	0.07788700	3.07137082	0.18258031
0	<i>g'</i>	$-3.08268506 \times 10^{-8}$	$3.81481002 \times 10^{-9}$	0.46164800	1.26595777	3.64089673
100	<i>g'</i>	$-5.18727283 \times 10^{-11}$	$2.67394995 \times 10^{-11}$	0.07491600	3.23359776	0.19327453
0	terminator	$1.43824952 \times 10^{-11}$	$6.70574706 \times 10^{-14}$	0.51349110	0.88923937	3.06736742
100	terminator	$-1.756482754 \times 10^{-9}$	$1.37667655 \times 10^{-13}$	0.09017801	1.11840638	0.18901436

Table A.6: Error associated with the integration and propagation of the state transition matrix for different trajectories in the AHP model with the  $J_2$  and  $J_4$  gravity perturbations. Initial conditions are presented in non-dimensional coordinates, and  $z_0$  is zero for all orbits except for the terminator family, where  $z_0 = 0.32021070$  for  $\beta = 0$  and  $z_0 = 0.04221324$  for  $\beta = 100$ .

$\beta$	Family	$1 - \det(\Phi_M)$	$1 -  \lambda_i $	$x_0 [-]$	$\dot{y}_0 [-]$	$t [-]$
0	<i>a</i>	$1.80744874 \times 10^{-9}$	$1.04155951 \times 10^{-4}$	0.35551600	1.88562005	3.45874693
100	<i>a</i>	$4.66854443 \times 10^{-10}$	$6.10267392 \times 10^{-12}$	0.02808100	8.06377600	0.13891974
0	<i>g'</i>	$6.69358458 \times 10^{-10}$	$2.86086621 \times 10^{-4}$	0.30466100	2.16127598	4.36297269
100	<i>g'</i>	$-3.77606835 \times 10^{-11}$	$6.66133814 \times 10^{-15}$	0.02559400	8.41711631	0.16059013
0	terminator	$2.61920485 \times 10^{-11}$	$1.66644476 \times 10^{-13}$	0.11439490	2.10694079	2.73260919
100	terminator	$-4.02566869 \times 10^{-13}$	$5.06261699 \times 10^{-14}$	0.09017801	4.79674217	0.05886014

Table A.7: Error associated with the integration and propagation of the state transition matrix for different periodic orbits in the AHP model with eclipses. Initial conditions are presented in non-dimensional coordinates, and  $z_0$  is zero for all orbits except for the terminator family, where  $z_0 = 0.19962821$  for  $\beta = 0$  and  $z_0 = 0.03303122$  for  $\beta = 100$ .

$\beta$	Family	$1 - \det(\Phi_M)$	$1 -  \lambda_i $	$x_0 [-]$	$\dot{y}_0 [-]$	$t [-]$
0	<i>a</i>	$-1.30707001 \times 10^{-10}$	$3.44643164 \times 10^{-5}$	0.38036000	1.74472173	3.39128018
100	<i>a</i>	$2.26441676 \times 10^{-9}$	$6.081918 \times 10^{-2}$	0.0303541	7.71115245	0.14154648
0	<i>g'</i>	$1.046029929 \times 10^{-11}$	0.04110205	0.03724100	6.68391892	0.16894245
100	<i>g'</i>	$-5.18727283 \times 10^{-11}$	$2.67394995 \times 10^{-11}$	0.07491600	3.23359776	0.19327453
0	terminator	$1.43824952 \times 10^{-11}$	$6.70574706 \times 10^{-14}$	0.51349110	0.88923937	3.06736742
100	terminator	$-1.756482754 \times 10^{-9}$	$1.37667655 \times 10^{-13}$	0.09017801	1.11840638	0.18901436

the stability indices of these families can be seen in Table ??, in Section A.3, where the differential correction algorithm is verified. Figures A.6 and A.7 present a qualitative comparison with the work presented by Heñon in [27] and by García Yárnoz et al. in [29]. Note also that in [27], family *a* continues for negative values of energy, which are not analyzed in the work for this thesis. Also, in [27], the stability index is referenced as *a* and is equal to  $\frac{1}{2}k_i$ ; Hénon plots only one of the stability indices in his work. We show also only one of the stability indices from [29] since the other is equal to two.

### A.3. Differential correction algorithm

Finally, we analyze operation (3), which refers to the single-shooting differential correction algorithm implemented to find periodic orbits. In order to verify this operation, we analyze the magnitudes of the correction applied to each iteration of the algorithm, to verify that it asymptotically leads to zero. From this we check the position error after a period of a periodic orbit obtained with the algorithm. Finally, we compare the results obtained for the initial conditions of periodic orbits with the values found in [27, 48] for the AHP model.

Figure A.8 shows an example of the magnitudes of the implemented corrections per iteration, by the algorithm, to an initial guess that is close enough to the solution <sup>1</sup>.

<sup>1</sup>The correct convergence of single-shooting differential correction algorithm depends on how close to the actual solution the first guess is [54]. The values for this error depend on the orbits, their stability, and model considered, and as such as not detailed here.

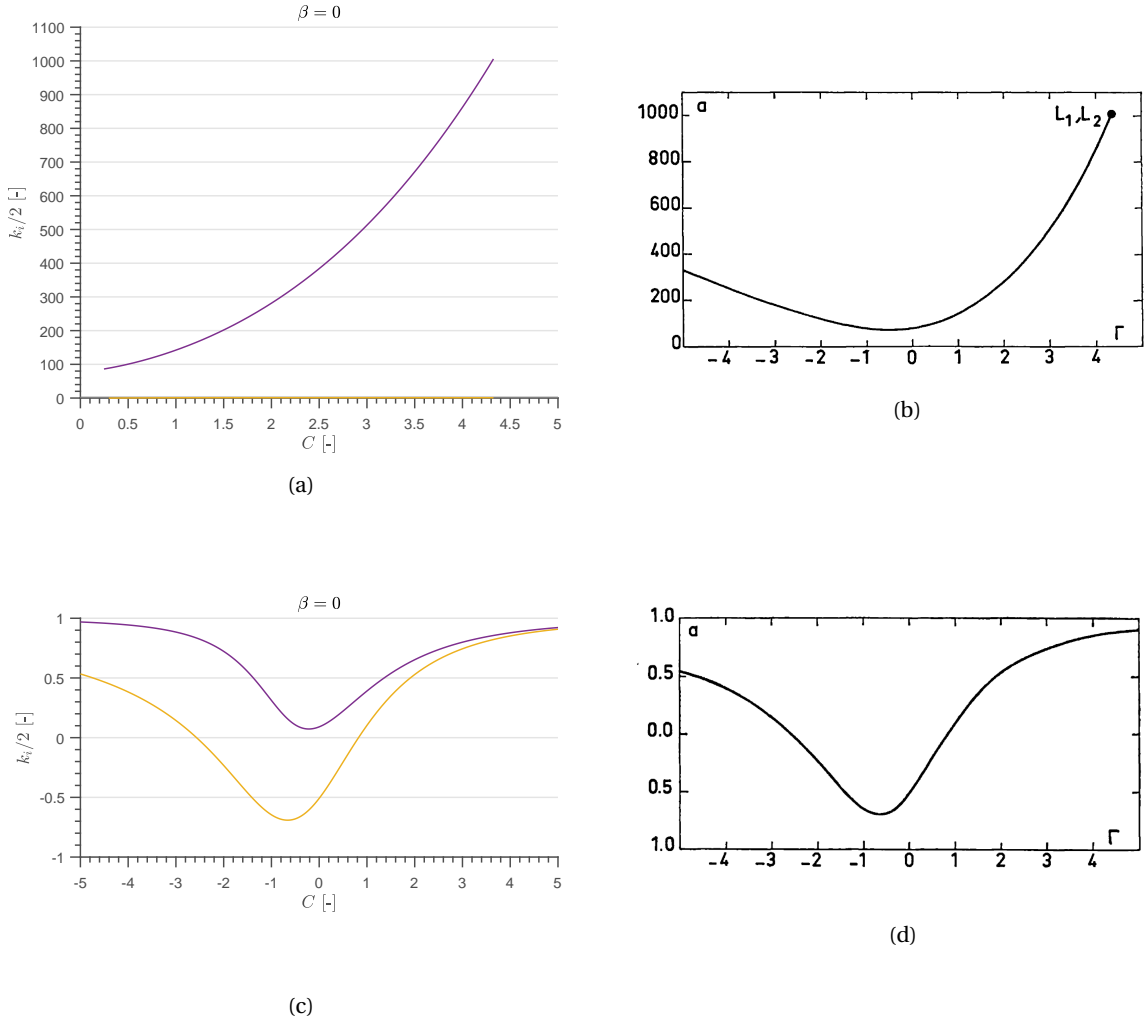


Figure A.6: Comparison of the stability index of families of periodic orbits  $a$  and  $f$  from the AHP model and from source [27] for  $\beta = 0$ . The  $x$ -axis displays the Jacobi constant, represented by  $\Gamma$  in [27]. (a) Stability indices of orbit family  $a$  in AHP model; (b) stability index of orbit family  $a$  from source [27]; (c) stability indices of orbit family  $f$  in AHP model; (d) stability index of orbit family  $f$  from source [27].

Tables A.8 to A.11 show the position error after one period of different orbits of the orbit families  $a$  and  $g'$  obtained by the differential corrector algorithm for the different models. We can see that for a tolerance of  $10^{-9}$ , i.e., the algorithm deems a solution has converged when the magnitude of the correction is smaller than  $10^{-9}$ , the largest position errors between the initial and final states are in the order of millimeter. Considering the position magnitudes reach the orders of  $10^4$  m, a position error  $10^7$  orders of magnitude smaller is deemed acceptable. Moreover, we see these errors are largest when considering the full model, which includes the gravity and eclipse models. This is again due to the fact that *ode45* must take more steps for the "more demanding dynamics" and thus the integration error accumulates, becoming larger. The tables thus present not only the error relative to the differential corrector algorithm but also the error inherent to the integration of the state vector by MATLAB<sup>®</sup>, complementing the verification undertaken in Section A.A.1.

As a final step, in Tables ?? and ?? we compare the results of the algorithm with results found in literature, so as to further verify differential corrector. In Table ?? we include also the values for the stability index of some of the periodic families of orbits, so as to complete the verification done in Section A.2. From these tables we can see that the values for the initial conditions (and stability indices) of these orbits match with small errors. This is particularly true for Table ??, where, since we consider only planar orbits, the single-shooting differential correction algorithm varies only the initial velocity in the  $y$  direction to correct for the periodic orbit. The small differences between the results of the differential corrector and those from [27] may originate from a variety of different places: the use of different integrators, the use of different algorithms for finding periodic orbits and different tolerances, the precision of the machine, among others. Nonetheless, the closeness in results verifies

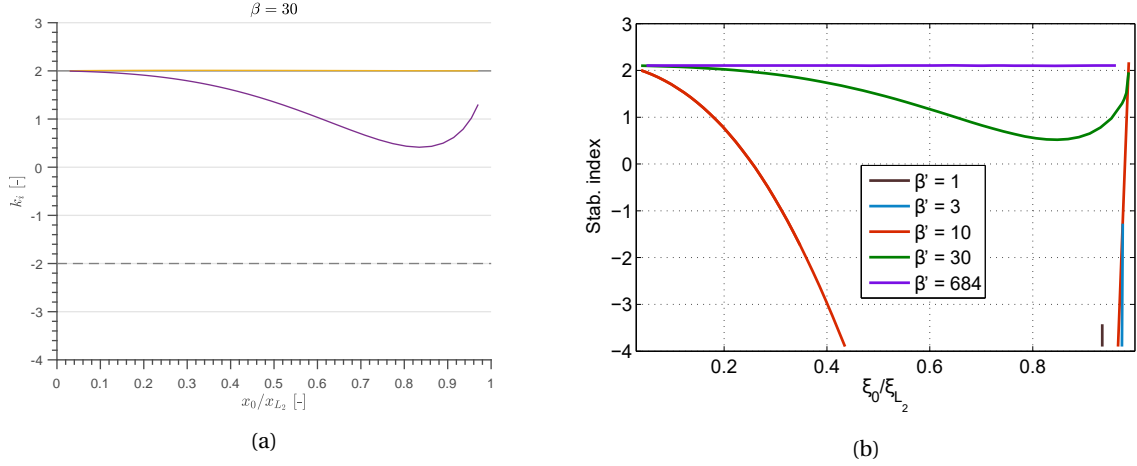


Figure A.7: Comparison of the stability index from family of periodic orbits  $g'$  from the AHP model and from source [29] for  $\beta = 30$ . The x-axis display the ratio between the initial  $x$  coordinate of the orbit and the  $x$  coordinate for the  $L_2$  point. (a) Stability of orbit family  $g'$  in AHP model; (b) stability of orbit family  $g'$  from source [29].

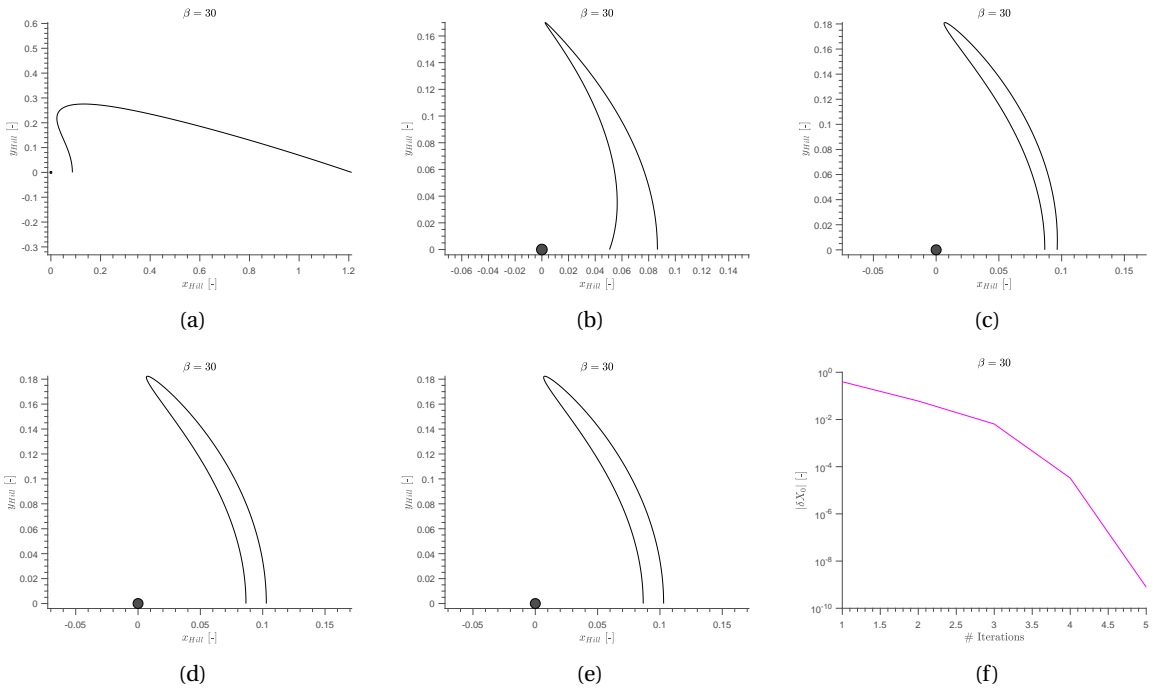


Figure A.8: Iterative process of the single-shooting differential corrector for an orbit of family  $a$  with  $\beta = 30$ . Figures (a)-(e) show the iteratively corrected orbit; figure (f) shows the magnitude of the correction at each iteration. Note that the orbit is corrected for half a period only.

the correct implementation of the algorithm. The results in Table A.13 differ slightly more; this may occur because we have two free-variables in this case,  $z_0$  and  $y_0$ , which may cause the algorithm to converge on a slightly different solution. Also, the above explanations, related with the difference in integrators, tolerances, among others, still apply.

Table A.8: Position error after one period in the AHP model for families of periodic orbits  $a$  and  $g'$ . Initial conditions are presented in non-dimensional coordinates, and  $y_0, z_0, \dot{x}_0, \dot{z}_0 = 0$ .

$\beta$	Family	$\Delta_r$ [m]	$x_0$ [-]	$\dot{y}_0$ [-]	$T$ [-]
0	$a$	$1.53916654 \times 10^{-6}$	0.24869900	2.58416552	3.89461730
30	$a$	$2.06054739 \times 10^{-6}$	0.05132600	5.92567848	0.69682678
200	$a$	$3.01033402 \times 10^{-8}$	0.0172700	10.41283556	0.08002881
0	$g'$	$1.76780447 \times 10^{-4}$	0.11622500	4.09267668	6.91424001
30	$g'$	$2.61511782 \times 10^{-8}$	0.08433387	4.14668673	0.43251929
200	$g'$	$1.42991770 \times 10^{-4}$	0.02894000	7.43861772	0.10109334

Table A.9: Position error after one period in the AHP model with the  $J_2$  and  $J_4$  gravity perturbations for the families of periodic orbits  $a$  and  $g'$ . Initial conditions are presented in non-dimensional coordinates, and  $y_0, z_0, \dot{x}_0, \dot{z}_0 = 0$ .

$\beta$	Family	$\Delta_r$ [m]	$x_0$ [-]	$\dot{y}_0$ [-]	$T$ [-]
0	$a$	$1.18579721 \times 10^{-5}$	0.33092200	2.03074970	3.53554695
30	$a$	$2.00834311 \times 10^{-9}$	0.05132600	5.92581163	0.34841633
200	$a$	$8.39258638 \times 10^{-8}$	0.0231000	8.76492734	0.0849180
0	$g'$	$6.83436276 \times 10^{-4}$	0.11622500	4.09268975	6.91430612
30	$g'$	$2.24528922 \times 10^{-8}$	0.08433387	4.14674659	0.43252583
200	$g'$	$2.28743164 \times 10^{-5}$	0.02894000	7.43954805	0.10112139

Table A.10: Position error after one period in the AHP model with eclipses for families of periodic orbits  $a$  and  $g'$ . Initial conditions are presented in non-dimensional coordinates, and  $y_0, z_0, \dot{x}_0, \dot{z}_0 = 0$ .

$\beta$	Family	$\Delta_r$ [m]	$x_0$ [-]	$\dot{y}_0$ [-]	$T$ [-]
30	$a$	$1.66533962 \times 10^{-3}$	0.03469471	7.41480793	0.32595655
200	$a$	$3.78375713 \times 10^{-4}$	0.016424084	10.72807973	0.07958770
30	$g'$	$4.07500195 \times 10^{-7}$	0.01247244	12.56243852	0.37428648
200	$g'$	$2.09500178 \times 10^{-4}$	0.02744236	7.76227102	0.10104096

Table A.11: Position error after one period in the full model (with eclipses and gravity perturbations), for families of periodic orbits  $a$  and  $g'$ . Initial conditions are presented in non-dimensional coordinates, and  $y_0, z_0, \dot{x}_0, \dot{z}_0 = 0$ .

$\beta$	Family	$\Delta_r$ [m]	$x_0$ [-]	$\dot{y}_0$ [-]	$T$ [-]
30	$a$	$1.84303435 \times 10^{-3}$	0.04329009	6.55417338	0.33808245
200	$a$	$3.85548551 \times 10^{-4}$	0.017669748	10.29884369	0.08067282
30	$g'$	$1.07667649 \times 10^{-4}$	0.04458246	6.37610978	0.39944588
200	$g'$	$3.25872597 \times 10^{-4}$	0.01329505	11.92798507	0.09368297

Table A.12: Comparison between results found by the differential corrector and those in [27], for  $\beta = 0$ , for families of periodic orbits  $a$ ,  $g'$  and  $f$ . Initial conditions are presented in non-dimensional coordinates, and  $y_0, z_0, \dot{x}_0, \dot{z}_0 = 0$ .

<b>Fam.</b>	$x_0$	$x_0^*$ ([27])	$C$	$C^*$ ([27])	$\frac{T}{2}$	$\frac{T^*}{2}$ ([27])	$\frac{1}{2}k$	$\frac{1}{2}k^*$ ([27])
$a$	0.62698000	0.62698	4.19999870	4.2	1.52566014	1.52566	948.8629	948.9
$a$	0.5802000	0.58020	4.00001980	4	1.54114889	1.54115	862.3554	862.3
$a$	0.4958000	0.4958	3.50000724	3.5	1.58658735	1.58659	671.0336	671.0
$a$	0.6269800	0.30114	2.00001660	2	1.82236569	1.82237	281.3745	281.4
$a$	0.1879700	0.18797	0.99998274	1	2.16320943	2.16320	142.1867	142.2
$f$	-0.1477900	-0.14779	6.00007789	6	0.16968333	0.16969	0.94014229	0.9401
$f$	-0.1716900	-0.17169	4.99987602	5	0.21011250	0.21011	0.92210477	0.9084
$f$	-0.2507100	-0.25071	2.99997164	3	0.35696220	0.35696	0.74425013	0.7443
$g'$	0.4808000	0.48080	3.49998119	3.5	1.78840908	1.78840	-152.5375	-152.5
$g'$	0.4105200	0.41052	2.99996403	3	1.91345170	1.91344	-185.5729	-185.6
$g'$	0.3455500	0.34555	2.50003146	2.5	2.06129717	2.06131	-201.3952	-201.4
$g'$	0.1677800	0.16778	0.99996663	1	2.90438219	2.90435	-232.6846	-232.7

Table A.13: Comparison between results found by the differential corrector and those in [48], for  $\beta = 33$ . Initial conditions are presented in non-dimensional coordinates, and  $y_0, \dot{x}_0, \dot{z}_0 = 0$ .

$x_0$	$x_0^*$ ([48])	$z_0$	$z_0^*$ ([48])	$\dot{y}_0$	$\dot{y}_0^*$ [48]	$T$	$T$ ([48])
0.1276804	0.1276804	0.0849533	0.0849524	1.4457657	1.4457752	0.393074	0.392906
-0.1061893	-0.1061893	0.1106582	0.1106481	0.8425931	0.8425277	0.382755	0.382064